INSTITUTO SUPERIOR DE ENGENHARIA DO PORTO
MESTRADO EM ENGENHARIA MECÂNICA




Evaluation of different damage initiation and growth criteria in the cohesive zone modelling analysis of single-lap bonded joints

RICARDO JORGE BRAGA DA ROCHA
Outubro de 2016

POLITÉCNICO
DO PORTO

Instituto Superior de Engenharia do Porto

EVALUATION OF DIFFERENT DAMAGE INITIATION AND GROWTH CRITERIA IN THE COHESIVE ZONE MODELLING ANALYSIS OF SINGLE-LAP BONDED JOINTS

Ricardo Jorge Braga da Rocha

2016

Instituto Superior de Engenharia do Porto

Mechanical Engineering

POLITÉCNICO DO PORTO

Instituto Superior de Engenharia do Porto

EVALUATION OF DIFFERENT DAMAGE INITIATION AND GROWTH CRITERIA IN THE COHESIVE ZONE MODELLING ANALYSIS OF SINGLE-LAP BONDED JOINTS

Ricardo Jorge Braga da Rocha

Dissertation presented at Instituto Superior de Engenharia do Porto for the fulfilment of requirements towards a Master's degree in Mechanical Engineering. The work was performed under the orientation and guidance of Professor Raul Duarte Salgueiral Gomes Campilho.

2016

Instituto Superior de Engenharia do Porto

Mechanical Engineering

POLITÉCNICO DO PORTO

JURY

President

To be defined

Coordinator

Raul Duarte Salgueiral Gomes Campilho

Assistant Professor, ISEP

Examiner

To be defined

ACKNOWLEDGEMENTS

I would like to gratefully thank my supervisor Dr. Prof. Raul Duarte Salgueiral Gomes Campilho for his invaluable support throughout the development of this thesis. My sincere gratitude for his mentoring, counsel, writing and grammar reviews, and for sharing with me his large expertise and experience.

I would also wish to specially thank my wife Arciona Banze, my daughter Mariana Rocha, my parents Jorge Rocha and Maria Alice, my sister Ana Rocha and her husband Emanuel Nogueira for their absolute support, even when study times restricted my social interactions with them during these years.

Finally, my gratitude goes to the Instituto Superior de Engenharia do Porto, as institution and to its staff, and to all the teachers for the knowledge provided during the past five years.

KEYWORDS

Structural adhesive, single-lap joint, cohesive zone models, finite element, numerical simulation

ABSTRACT

Adhesively-bonded joints are extensively used in several fields of engineering. Cohesive Zone Models (CZM) have been used for the strength prediction of adhesive joints, as an add-in to Finite Element (FE) analyses that allows simulation of damage growth, by consideration of energetic principles [1]. A useful feature of CZM is that different shapes can be developed for the cohesive laws, depending on the nature of the material or interface to be simulated, allowing an accurate strength prediction. On the other hand, different simulation conditions, and damage initiation and growth criteria, are available for use in CZM analyses to provide the mixed-mode behaviour required to analyse these structures, having as basis the pure tensile and shear CZM laws. Thus, it is highly relevant to understand in detail the influence of these different conditions on the outcome of the simulations. This work studies the influence of different conditions used in CZM simulations to model a thin adhesive layer in single-lap adhesive joints under a tensile loading, for an estimation of their influence on the strength prediction under different geometrical and material conditions. Validation with experimental data is considered. A comprehensive evaluation is performed, considering adhesives ranging from brittle (Araldite® AV138) to highly ductile (Sikaforce® 7752). An adhesive with moderate ductility, the Araldite® 2015, is also considered. Overlap lengths (L_O) between 12.5 and 50 mm were also equated. Different simulation conditions were performed and analysed, in which regards to: variation of the elastic stiffness of the cohesive law, decoupling of the loading modes, evaluation of different law shapes, variation of the cohesive parameters and consideration of several damage initiation and growth criteria. The analysis carried out in this dissertation allowed to conclude that CZM is a powerful technique for strength prediction of bonded joints, provided that the modelling conditions are properly defined. The influence of varying conditions to the standard ones was also assessed, showing that erroneous results can be obtained if the choice of the modelling conditions is not the most suitable for the problem.

PALAVRAS CHAVE

Adesivos estruturais, junta de sobreposição simples , modelos de dano coesivo, elementos finitos, simulação numérica

RESUMO

As juntas adesivas têm vindo a ser cada vez mais utilizadas em diversos ramos da engenharia. Por outro lado, os modelos de dano coesivo (MDC) têm vindo a ser utilizados para prever a resistência das juntas adesivas, como um desenvolvimento dos Elementos Finitos (EF) que permite a simulação do crescimento do dano através da consideração dos principios energéticos [1]. Uma caracteristica importante dos MDC é a possibilidade de desenvolver diferentes formas de leis coesivas, dependendo da natureza do material ou da interface a ser simulada, permitindo desse modo a correta previsão da resistência. Por outro lado ainda, na análise de MDC, diferentes condições de simulação, critérios de iniciação e crescimento do dano estão disponíveis para simular o comportamento em modo misto, necessárias para analizar as ligações adesivas, tendo como base leis coesivas em modo puro de tração e corte. Torna-se então extrememente importante compreender detalhadamente a influência destas diferentes condições nos resultados das simulações. Este trabalho estuda a influência de diferentes condições de MDC usadas para modelar uma camada fina de adesivo numa junta de sobreposição simples, sujeita a tração, de forma a avaliar de que forma a previsão da resistência é afectada por estas condições. Os resultados numéricos são validados com recurso a um trabalho prévio experimental. O estudo considerou juntas com comprimentos de sobreposição entre 12,5 e 50 mm e adesivos que variam desde o frágil (Araldite® AV138) ao de elevada ductilidade (Sikaforce® 7752). Recorreu-se ainda a um adesivo de ductilidade moderada, o Araldite®2015. As diversas condições de simulação realizadas e analisadas foram: variação da rigidez da lei coesiva, a dissociação dos modos de carregamento, diferentes formas de leis coesivas, variação dos parâmetros coesivos e a validação de diferentes critérios de inicio e crescimento do dano. A análise desenvolvida nesta dissertação permitiu concluir que os MDC são uma técnica robusta para a previsão da resistência de juntas adesivas, desde que e que as condições de modelação sejam corretamente definidas. A influência da variação das condições de modelação foi analisada, mostrando que os resultados podem ser adulterados quando a escolha das condições não é a mais acertada.

SYMBOLS, UNITS AND ABBREVIATIONS LIST

Abbreviations List

2D	Two Dimensions
3D	Three Dimensions
ASTM	American Society for Testing and Materials
BK	Benzeggagh-Kenane
CBBM	Compliance-Based Beam Method
CBT	Corrected Beam Theory
CCM	Compliance Calibration Method
CZM	Cohesive Zone Models
DCB	Double-Cantilever Beam
DoE	Design of Experiment
ENF	End-Notched Flexure
FE	Finite Element
FEM	Finite Element Method
KM	Kriging Metamodel
LEFM	Linear Elastic Fracture Mechanics
L_O	Overlap Length
MAXE	Maximum Nominal Strain Criterion
MAXPE	Maximum Principal Strain Criterion
MAXPS	Maximum Principal Stress Criterion
MAXS	Maximum Nominal Stress Criterion
P_m	Maximum Load
QUADE	Quadratic Nominal Strain Criterion
QUADS	Quadratic nominal Stress Criterion
SAAS	Stress Analysis for Adhesive Structures
SLB	Single-Leg Bending
SLJ	Single-Lap Joint
TAST	Thick Adherend Shear Test
UV	Ultra Violet
XFEM	eXtended Finite Element Method

Units List

°C	degree Celsius
g	gram
GPa	giga Pascal
kN	kilo Newton

m	meter
min	minute
mm	millimetres
MPa	mega Pascal
N	Newton
N/mm	Newton by millimetre

Symbols List

b	Joint width
C	Curve surrounding crack tip
d_n	Damage variable in tension
d_s	Damage variable in shear
E	Young's modulus
G	Shear modulus
G_C	Fracture toughness
G_I	Strain energy release rate in pure-mode I
G_{IC}	Critical strain energy release rate or fracture toughness in pure-mode I
G_{II}	Strain energy release rate in pure-mode II
G_{IIC}	Critical strain energy release rate or fracture toughness in pure-mode II
G_{III}	Strain energy release rate in pure-mode III
G_{IIIC}	Critical strain energy release rate or fracture toughness in pure-mode III
G_s	Strain energy release rate in pure-mode II plus pure mode III
G_T	Total strain energy release rate
J	J-integral
K	Stiffness matrix
K_{nn}, K_{ns}, K_{ss}	Stiffness parameters
L_T	Total length between gripping points
m, b	Parameters of the straight line equation
n	Element nodes
$\tilde{n}$	Element phantom nodes
P	Load
P_m/P_m^0	Maximum strength divided by previously predicted maximum strength
S	Arc length
t	Traction
t_A	Adhesive thickness
T_j	Traction vector
t_m^0	Cohesive strength in mixed-mode
t_n	Current tensile traction

t_n^0	Tensile cohesive strength
t_n^{und}	Current cohesive traction in tension
t_P	Adherends thickness
t_s	Current shear traction
t_s^0	Shear cohesive strength
t_s^{und}	Current cohesive traction in shear
u_j	Displacement vector
W	Energy density
x	Distance from the left edge of the adhesive layer
x_1	Coordinate system
x_2	Coordinate system
α	Parameter for the 3D criterion, power law parameter, non-dimensional parameter for the linear-exponential cohesive law
β, Υ	Parameters for the 3D criterion
γ_f	Shear failure strain
δ	Displacement
Δ	Percentile deviation
δ_m^0	Displacement at cohesive strength in mixed-mode
δ_m^f	Mixed-mode failure displacement
δ_n	relative displacement in tension
δ_n^0	Displacement at peak tensile strength
δ_n^f	Failure tensile displacement
δ_n^s	Stress softening onset displacement in tension
δ_s	relative displacement in shear
δ_s^0	Displacement at peak shear strength
δ_s^f	Failure shear displacement
δ_s^s	Stress softening onset displacement in shear
ε	Strain
ε_f	Tensile failure strain
ε_{max}	Current maximum principal strain
ε_{max}^0	Allowable maximum principal strain
ε_n	Current tensile strain
ε_n^0	Peak tensile strain
ε_s	Current shear strain
ε_s^0	Peak shear strain
η	Characteristic material parameter
ν	Poisson's ratio
σ_f	Tensile failure stress
σ_{max}	Current maximum principal stress

σ_{max}^{0}	Allowable maximum principal stress
σ_y	Tensile yield stress, peel stress
τ_{avg}	Average shear stress
τ_f	Shear failure strength
τ_{xy}	Shear stress
τ_y	Shear yield strength

FIGURES INDEX

TABLES INDEX

INDEX

INTRODUCTION

1 INTRODUCTION

1.1 Framework

Adhesively-bonded joints are an increasing alternative to mechanical joints in several engineering applications, providing many advantages over conventional mechanical fasteners [2]. By the use of adhesive bonding the integrity of the parent materials is preserved and different materials can be joined. Other advantages are high fatigue resistance, capability of fluid sealing, smaller weight, and most of all, more uniform stress distributions. In order to attain a more efficient use of adhesives, it is necessary to be able to analyse them. This means to evaluate stresses and strains under a given load, and to predict the probable points of failure. Analytical and numerical techniques (i.e. FE analysis) for strength prediction of bonded joints were improved over the years. The FE is by far the most common technique used in the context of adhesively bonded joints, by consideration of stress/strain or fracture mechanics criteria for strength prediction. However, FE has limitations such as predictions dependent on the mesh size at the critical regions, and the need of an initial crack by the fracture criteria. Surpassing those limitations was accomplished by CZM. Compared to conventional FE, a much more accurate prediction is achieved. CZM are an advanced numerical technique based on FE for the structural simulation of crack nucleation and growth, relying on continuum mechanics and fracture mechanics principles. A large amount of works is currently available that use CZM for strength prediction of bonded joints [3-5]. CZM depend on several parameters, the choice of law shape, initiation and propagation criteria, amongst other modelling conditions, all of each with possible impact on the strength predictions. Thus, a complete and detailed understanding of these affects is essential for the correct application of this method.

1.2 Objectives

The initial purpose of this study is the experimental strength evaluation of single-lap joints (SLJ) with different values of L_O. Three different adhesives were used to bond an aluminium alloy (AW6082-T651) adherends, the brittle adhesive Araldite® AV138, the moderate ductile adhesive Araldite® 2015 and the high ductile Sikaforce® 7752. This experimental part is based on raw data extracted from previous works executed by de Sousa [6] (joints with the adhesives Araldite® AV138 and Araldite® 2015) and by Carvalho [7] (joints with the adhesive Sikaforce® 7752). All the data analysis and subsequent discussion from the original load-displacement (P-δ) curves from the tests were performed within the scope of this thesis. Upon the conclusion of the experimental study, begins the numerical work. The numerical conditions will be presented, either for the stress or strength analyses. Firstly, the stress analysis of the adhesive layer will be performed, allowing a better understanding of the joints' mechanical behaviour, as well

as the maximum loads (P_m). Afterwards, the strength prediction by FE/CZM is accomplished taking into account the previously mentioned conditions. This leads to the main purpose of this thesis: the evaluation of different simulation conditions in the CZM analysis for an accurate strength prediction. Different features were considered: the variation of the elastic stiffness of the cohesive law, the decoupling of the loading modes, the evaluation of different law shapes, the percentile variation of the cohesive parameters and the assessment of different initiation and propagation criteria. Finally, an analysis of the obtained results is presented.

1.3 Thesis layout

This thesis is structured in the following manner:

Section 1 presents a short contextualization of adhesive bonding, thesis objectives and layout.

Section 2, related to the bibliographic work, addresses the state-of-the-art, a brief comparative evaluation regarding other joining methods, common applications, typical loads, failure modes and joint configurations are aforementioned. The most relevant techniques for strength prediction are discussed at the end of this section.

Section 3 is divided into two main parts: subsection 3.1 related with the experimental work and subsection 3.2 addressing the numerical part of this work. Subsection 3.1 shows a detailed description of the experimental work, including all materials involved, manufacturing process, experimental tests and, finally, the experimental results were presented and discussed. Subsection 3.2 addresses the numerical work, where the numerical conditions used in the FE/CZM analysis are described. A stress analysis was initially performed to provide a basis for further discussions regarding the joint strength. Following, the joints' strength was predicted and compared against the experimental data. The end of this section presents and discusses the influence of different simulation conditions on the strength estimation of the bonded joints, concerning the variation of the elastic stiffness of the cohesive law, the decoupling of the loading modes, the evaluation of different law shape, the percentile variation of the cohesive parameters and the assessment of different initiation and propagation criteria.

In Section 4, the conclusions of this thesis as well as suggestions for future works were presented.

The last Section, 5, presents the bibliographic references used throughout this work.

BIBLIOGRAPHIC WORK

2 BIBLIOGRAPHIC WORK

This section addresses the main principles of adhesive bonding, common applications in several industries, typical loads, failure modes and the most popular joint configurations. Structural adhesives are also mentioned and categorized in this section, considering the different families. At the end of this section, the most relevant analytical and numerical methods for strength prediction of bonded joints are presented, with emphasis on CZM.

2.1 Adhesive bonding

The main objective of an efficient joint is an effective load transmission between the two components during its lifetime. Joining between components is normally accomplished by mechanical, welding or bonded unions. One important feature of bonded joints is the relatively small quantity of adhesive that is required compared to the weight of the final structure. The bonding technique by structural adhesives is increasing and overcoming traditional techniques such as welding, riveting or fastening, and the aeronautic industry has been the major responsible for this development. The acceptance and continuous improvement of this bonding technique originate other industries to use it, in their quest for lighter and stronger structures. Currently, adhesive bonding has applications in several areas from high technology industries such as aerospace and automotive, to traditional industries such as construction, shoe making and furniture [8]. This is because bonded joints are a fast and effective process to join components with more uniform stress fields at the bonding region, providing fluid sealing, high fatigue resistance and the possibility to join different materials [9].

2.1.1 Bonded joints' characterization

In order to design an efficient joint, there are basic requirements to fulfil, such as the proper choice of adhesive, suitable joint configuration, correct preparation of the bonding surfaces, wetting of surfaces that are to be bonded and a proper adhesive bonding process in terms of solidification and cure. Depending on the application, adhesives can be the worst option or the best alternative to join two subtracts.

Some advantages of adhesive joints are listed as [8, 10]:

- Capacity to obtain lighter and stronger structures;
- Possibility to join different materials and materials with reduced stiffness;
- More uniform stress fields along the bonded area, enabling a more efficient load transfer;
- Good corrosion resistance;

- High fatigue strength;
- Better aesthetics (without bolts heads, rivets or welding);
- Fluid sealing;
- Reduced costs in a project, since the fabrication of bonded joints can be automated.

However, adhesive bonding also has disadvantages, such as [8, 10]:

- Joint design needs to be oriented towards the elimination of peel stresses, since adhesive joints should be primarily subjected to shear stresses;
- Low resistance to temperature and humidity;
- Requirement of a surface treatment;
- Fixing tools are needed since adhesive curing is not instantaneous.

Figure 1 shows how stresses are distributed along the bonded area in a bonded joint, in comparison to a riveted joint, emphasizing on the higher stiffness of the former on account of the larger contact area.

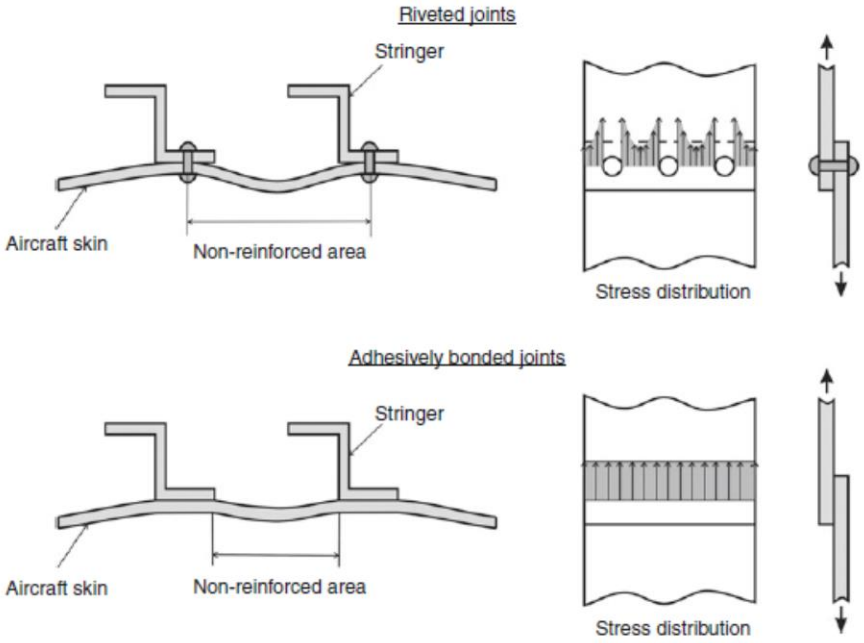

Figure 1 – Improved stiffness (left) and stress distribution (right) of adhesively-bonded joints compared to riveted joints [2]

2.1.2 Common applications of bonded joints

Adhesively bonded joints are nowadays present in several industries such as aeronautical, aerospace, automotive, railway, marine, electrical and civil construction [11].

The aircraft industry was only eleven years old when the First World War took place [11]. These five years of conflict revolutionized aircraft design and established the use of bonding (in those days more accurately named as gluing) as a means for joining structural aircraft components [12]. The first aircraft were built of wood. The use of natural adhesives in producing wood furniture and musical instruments has a history going back several hundreds of years. Therefore it cannot be just by chance that such a mean of joining structures was readily adopted. Later, by the end of the Second World War, wooden structures in military, passenger and freighter aircraft were slowly replaced by metals. More recently composites have begun to replace the metallic structures [13].

De Havillands and Fokker industries were the pioneers in using adhesive bonding in primary aircraft structures [2]. The Fokker F-27 Friendship (1955) and F-28 Fellowship aircraft (1967) are renowned for their successful widespread use of adhesive bonding. Other major airframers have restricted the use of adhesive bonding mainly to secondary structures. The major difference between primary and secondary structures is that primary ones would endanger the aircraft upon failure, while secondary structures are those that do not cause immediate danger upon failure. Figure 2 shows the extensive use in the aluminium airframe of the SAAB 340 aircraft, built in 1983. This aircraft has a structural efficiency and durability that is impossible to attain with conventional riveted structures.

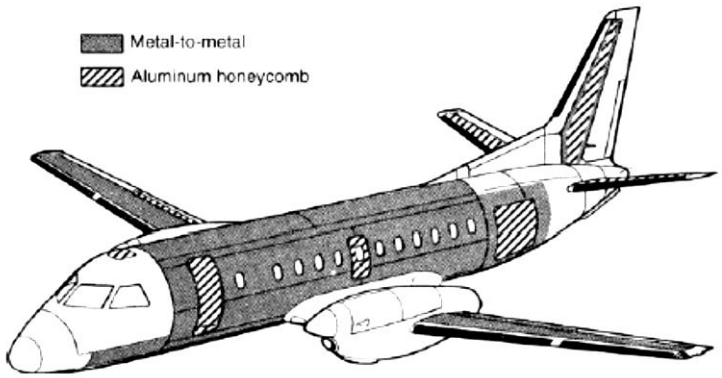

Figure 2 – Adhesive bonding in SAAB 340 fuselage, wings and tail [14]

Cessna made even more extensive the use of adhesive bonding in the fuselage of the Citation III Jet aircraft and used the same joining technology to produce wings on other aircraft with far fewer fuel leaks than on conventional riveted wing boxes [15]. The secondary structures, control surfaces and fixed panels of the Boeing 747 extensively used adhesive bonding in metals, mainly with honeycomb. Many of these components have been replaced by composite structures in later models. However, most of these components still require adhesive bonding [14]. Figure 3 shows the Boeing 777 composite tail, made by co-bonding pre-cured stiffeners to green skins.

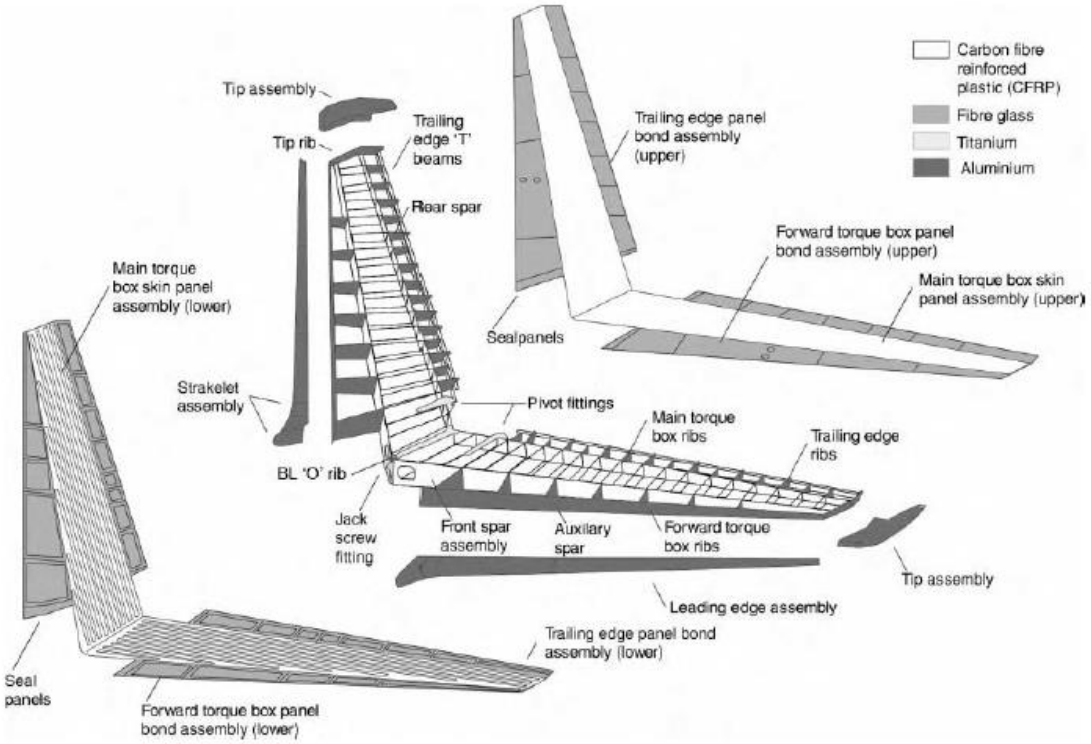

Figure 3 – Co-bonded composite primary structure on Boeing 777 tail [14]

Adhesive bonding has a great advantage over co-curing of composites for high production rates. In fact, co-cured structures require the use of larger tools for a higher time than adhesive bonding.

It is imperative to ensure that bonded joints will never be the weak link in the structure. However, it is not possible to inspect quality in bonded and composite structures afterwards, so the quality check must be assured during the fabrication process [14]. The inability to guarantee the quality of bonded structures after they have been built is a great obstacle to their widespread use. To assure quality control for bonded structures an appropriate process should be specify and followed, for example by shear and peel tests. Ultrasonic inspections can be relied upon only to assess in-service impact damage, not progressive degradation. However, at the time of manufacture, ultrasonic inspections can identify gaps and misfits [2]. Once a defect is detected, large inspection costs should be undertaken to assure that it has not grown. Visual inspections can be incredibly valuable, even if they not eliminate the need for all other tests.

Back in in the 1970's, an Airbus A300–600 had 5% of composite materials in its structure, while the recent Airbus A350 XWB today has 50% [2]. Bonding is mandatory for assembling composite parts. Under European Space Agency Funding, composite design rules have been, and are still being, issued by the members of the European Institution, provide guidelines for future composite space equipment. At the beginning of the space conquest, the structural parts of launchers and satellites were mainly made of metal. If weight reduction is important in the aeronautic industry, applied to spacecraft this

accomplish is even more relevant. Particular attention should be paid to the behaviour of adhesives in a space environment, namely in which regards to vacuum degassing, residual volatile organic compounds condensation and sensitivity to photonic radiations, with atomic oxygen being considered as a destructive criterion [2]. Bonding in launchers and satellites is also disseminated, from the cold thermal insulation of the cryogenic tanks to the structural parts of the launcher.

Automotive industry is one of most active industries in the use of adhesive bonding. By joining different materials with adhesives, better performances are achieved in lightweight, durability, by overcoming fatigue issues, safety and vehicle assembly, due to the elimination of welding access problems [10]. The use of adhesives applied to the automotive industry began decades ago with the bonding of windscreens to improve aesthetics. Afterwards, adhesives were used to fill gaps in spot-welded flanges to prevent corrosion. It was discovered that, besides corrosion resistance, adhesive bonding also enhanced the stiffness of the car body. Modern cars like the E-class and the S-class of DaimlerChrysler have more than 50 m of structural bondings. The situation is similar for other high-performance cars (Figure 4 and Figure 5).

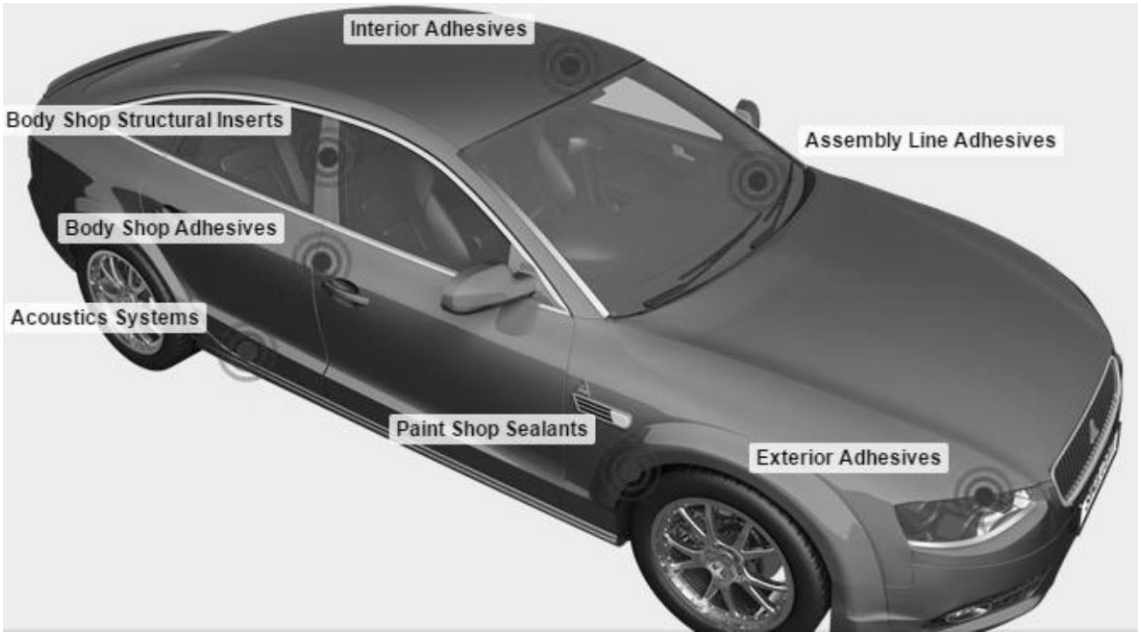

Figure 4 – Adhesive bonding in car [6]

Figure 5 – Adhesive bonding in the Lotus Elise [2]

In the train industry, adhesive bonding also became the most promising method to join multi-material structures. This technique enhances the weight advantage, improves the strength, stiffness and thermal insulation, reduces noise, and promotes the incombustibility and recyclability [2].

The marine industry requires a long-term durability in a seawater environment for structures. Therefore, the involved materials are mostly fiber reinforced composites, which in these industry are frequently assembled by adhesive bonding, in which surface preparation is a vital part [14]. The marine industry covers a wide range of structures, such as small boatyards, naval shipyards, racing yachts, and bonded structures for the offshore oil and gas industries. New markets are also appearing, for example the marine energy sector, which will require adhesives to bond structures like turbine blades.

2.1.3 Typical loads and failure modes in bonded joints

This sub-section gives a brief explanation of the different types of loads and failure modes in adhesive joints. Figure 6 shows the five types of loadings that can be found in adhesive joints. However, in adhesive joints a combination of these loads is typically found.

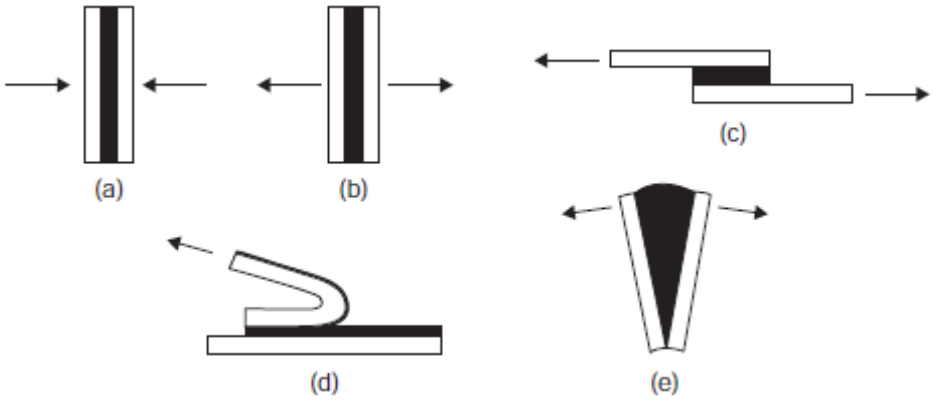

Figure 6 – Types of loads in adhesive joints: (a) compression, (b) tension, (c) shear, (d) peel and (e) cleavage [10]

Compression loads are not common in adhesives joints [10]. However, under a pure compression load the joint is less likely to fail. Actually, a joint loaded in pure compression hardly needs bonding of any sort if the compression force is high enough and there is no movement of the parts.

Tensile loads are the opposite of compression. They develop when forces act perpendicularly to the plane of the joint and are distributed uniformly over the entire area of the bond [11]. This loading distribution promotes a good joint strength with respect to the bonded area. However, in real applications, due to the difficulty to

guarantee the exact thickness of the adhesive layer and the alignment of the bonded parts, loads rarely are purely axial, therefore peel or cleavage stresses may occur.

Shear loads act in the plane of the adhesive and promote sliding between the adherends. Figure 7(a) shows shear stress distributions along the overlap of a SLJ. Stress peaks occur at the edges of the overlap. Whenever possible, most of the load should be transmitted as a shear load, because all of the bonded area contributes to the strength of the joint [11].

Peel loads try to split flexible adherends apart at one end of a bonded assembly, which originates high stress concentrations at the loaded overlap edge, as presented in Figure 7(b). This offers lower strength than joints loaded in shear because stresses are concentrated in a small area of the total bond. Unless the joint is wide or the load is small, failure of the bond will occur [10]. This type of loading is to be avoided if possible.

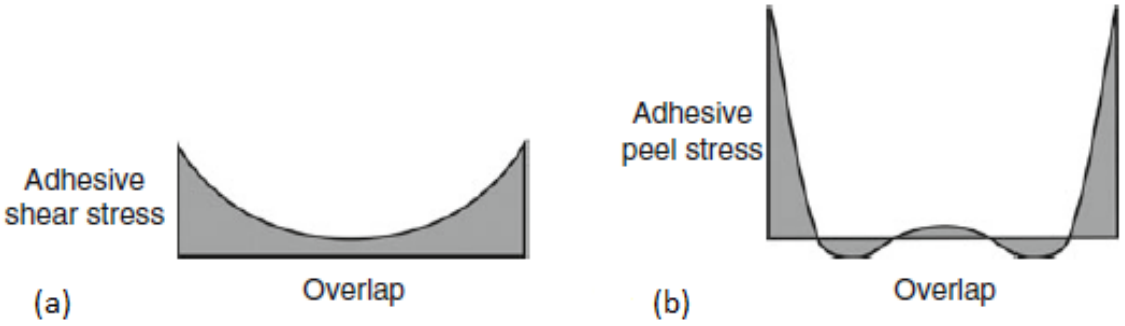

Figure 7 – Adhesive shear stress distribution along a SLJ (a) adhesive peel stress distribution along a SLJ (b) [2]

Cleavage loads occur when forces at one end of a bonded assembly act to split rigid adherends apart [11]. In joints under a cleavage load, similar to peel, the stresses are not evenly distributed along the adhesive layer, but they are instead concentrated at the loaded edge of the joint (Figure 8). However, the different stress distributions are due to the adherends' stiffness, since in cleavage the adherends are assumed as stiff, which results in a larger spread of stresses in the adhesive layer. The adherends' plasticization in peel loads promotes higher stress gradients towards the loaded edge of the adhesive [11, 13]. Both cleavage and peel stresses are undesirable for adhesive bonding.

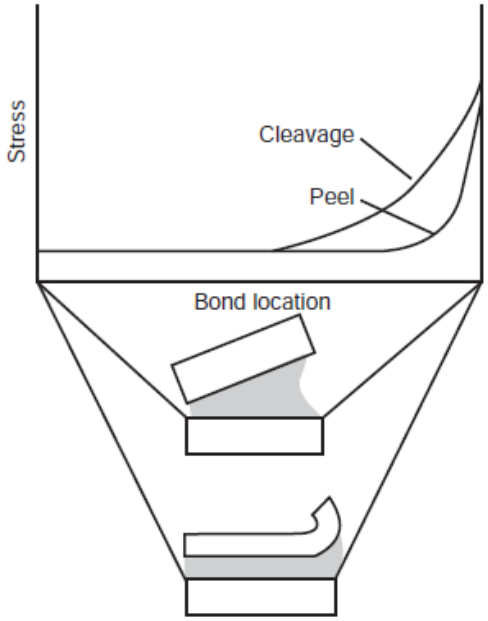

Figure 8 – Distribution of peel and cleavage stress [10]

The failure of a well-designed bonded joint should occur in the adherends. The standard ASTM D 5573-99 for classifying failure modes in fiber-reinforced-plastic foresees seven failure modes, from which it is important to report four of them applied to adhesive joints [2]. Figure 9 presents those possible failure modes.

Adhesive failure occurs in the interface between the adhesive and one of the adherends. Visually, one of the adherends has no adhesive, while the other adherend has the entire layer of adhesive attached to it. This failure mode results from a bad surface preparation or a bad adhesive choice.

Cohesive failure occurs when the bonding strength between the adherend and the adhesive is higher than the strength of the adhesive. With this failure mode, both failure surfaces have a thin layer of adhesive.

Adherend failure is when failure only occurs in the substrate. It hardly happens with high strength materials. This failure mode results from a correctly designed joint.

Mixed failure is a combination of adhesive and cohesive failures. This may happen because of a non-uniform cleaning in the adherend surfaces, or some areas with bad adhesion.

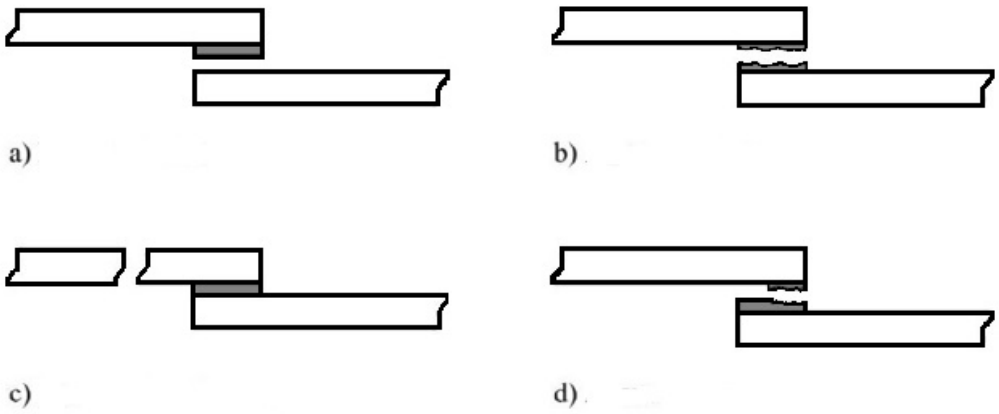

Figure 9 – Possible failure modes in bonded joints: adhesive failure (a), cohesive failure (b), adherend failure (c) and mixed failure (d) [6]

2.1.4 Joint configurations

In an ideal joint, the adhesive should be only subjected to shear stresses and the load-bearing area as large as possible but, due to design limitations, this cannot always be applied [10]. The wide variety of available joint configurations and adhesive types offer designers a number of choices. Figure 10 and Figure 11 present different butt and lap bonded joints configurations, each one of these with specific advantages, limitations and manufacturing difficulties.

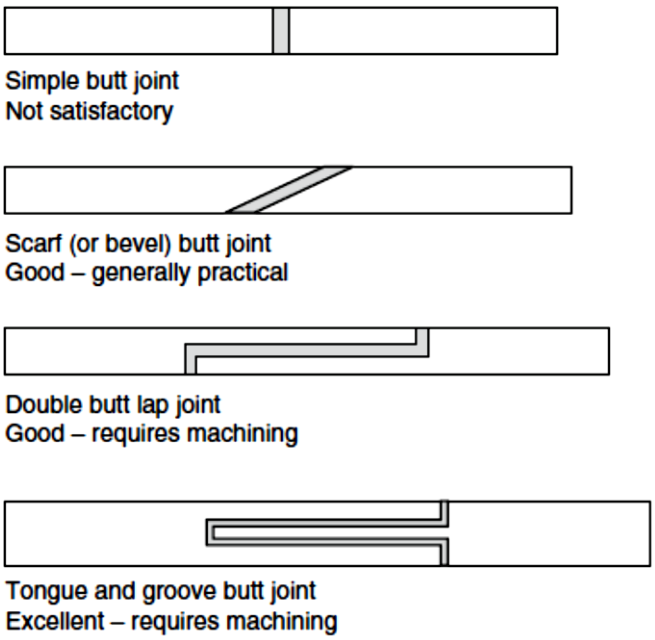

Figure 10 – Different butt joints designs [2]

Butt joints are the simplest to manufacture. However, they do not resist to bending loads, because under these conditions the adhesive is subjected to cleavage. Therefore, for this specific loading other variations were introduced. The tong and groove joints are the most efficient in the butt joint group, because they are self-aligned and act as a reservoir for the adhesive. Dvorak et al. [16] showed that adhesively-bonded tong and groove joints between steel and composite plates loaded in longitudinal tension are stronger than conventional strap joints, even in relatively thin plates.

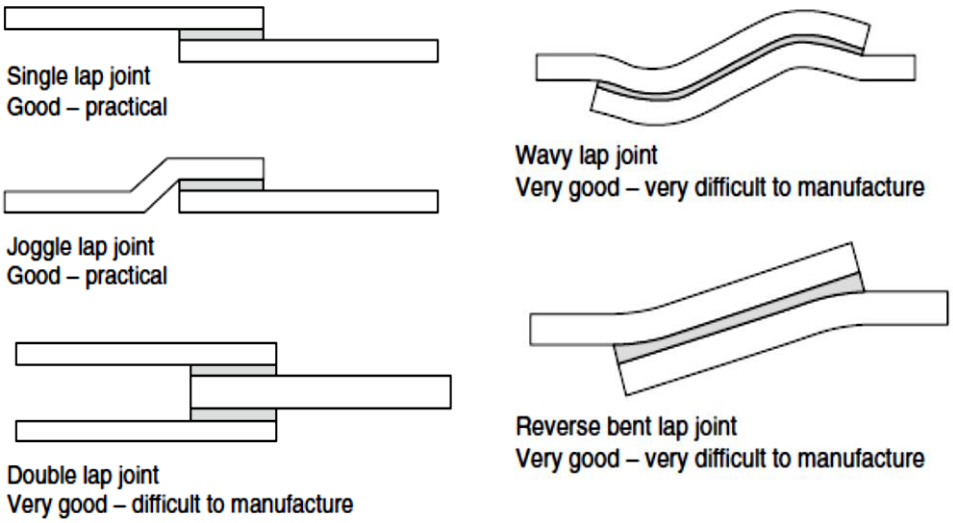

Figure 11 – Different lap joints designs [2]

Lap joints are the most commonly used adhesive joints (Figure 11). They are easy to manufacture, can be used with thin adherends and the adhesive is mostly loaded in shear. In the SLJ, the adherends are not collinear, which leads to significant peel stresses at the overlap end [11]. On the other hand, double-lap joints have a balanced construction that decreases the bending moment. However, there are internal bending moments that cause peel stresses at the ends of the inner adherend. Recent solutions included wavy and reverse-lap joints. Ávila and Bueno [17] analysed a wavy-lap joint configuration and showed that P_m carried by those joints was in average 41% higher than that carried by equivalent conventional SLJ.

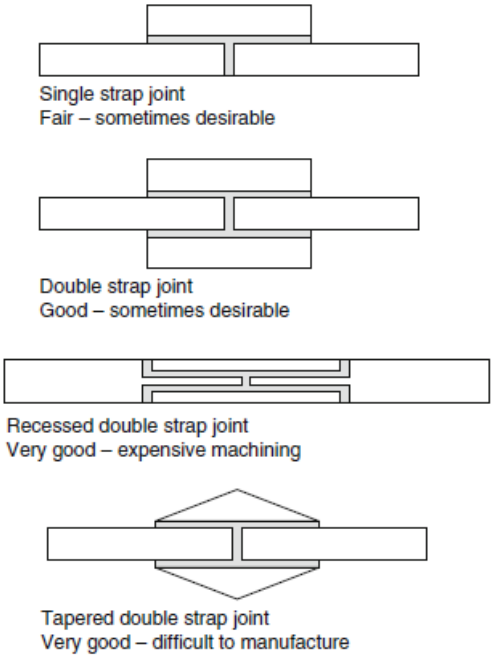

Figure 12 – Different strap joints designs [2]

Figure 12 presents various configurations of strap joints. This type of joints are generally used where overlap joints are impractical due the adherends' thickness [11]. The single-strap joint is subjected to significant peeling stresses due to the non-collinearity of the transmitted loads, equally to what happens to SLJ. The double-strap joint reduces the bending moment, therefore is stronger. The recessed and tapered double joints are used in fuselage repairs of aeronautical structures, being the best joint design to resist bending moments. Unfortunately, both require expensive machining operations [2, 11].

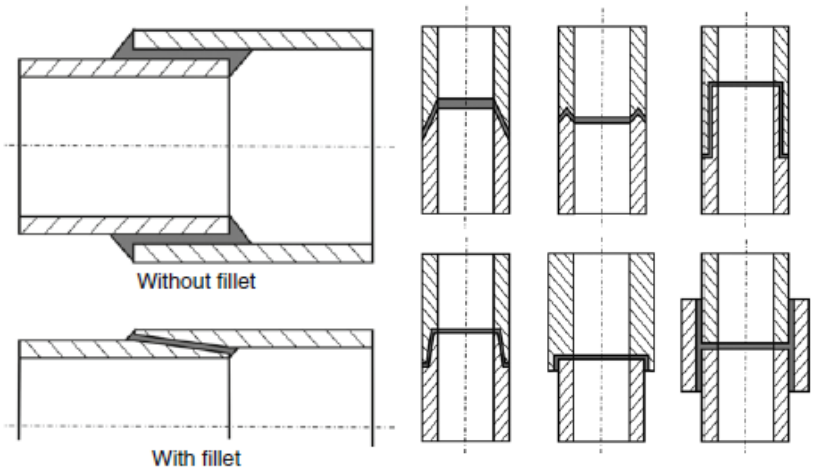

Figure 13 – Different tubular joints designs [2]

In tubular bonding, the loading can be axial or in torsional. Figure 13 shows different tubular joints designs. The left side figures explain that the square end can be replaced

by a taper, in case of axial loading, and the right side present joints commonly used in tubes. The presented solutions reveal advantage over butt joints because a larger bonded area is obtained and peel stresses are reduced. However, the disadvantages are the difficulty of inspection and the expensive machining operations [2, 10, 11]. Kim et al. [18] studied various tubular joint designs and found with an FE analysis and experimentally that the double-overlap configuration is the strongest joint.

2.1.5 Structural adhesives

There are two main types of adhesives: structural and non-structural. A structural adhesive is supposed to resist substantial loads, to be responsible for the strength and stiffness of the structure, and has been defined as having a shear strength higher than 7 MPa [15]. Non-structural adhesives are not required to support substantial loads, and can be applied for lightly loaded structures, for positioning purposes or fluid sealing. Based in different literature [2, 11, 19], adhesives can be classified by the nature of the base polymer, function, chemical composition, mode of application or reaction, physical form, by its family and cost. The most common classification of adhesives is by nature of the base polymer, which may be natural or synthetic. The functional classification defines adhesives as being either structural, hot-melt, pressure sensitive, water-base, ultra violet (UV) /electron beam-curing, high temperature, sealants, conductive and nanocomposites [2]. The classification by chemical composition divides the adhesives as being either thermosetting, thermoplastic, elastomeric, or hybrids of these. Thermosetting adhesives are materials that cure by an irreversible chemical reaction (often referred as crosslinked) at room or elevated temperatures, and they cannot be heated and softened repeatedly. Substantial pressure may be required with some thermosetting adhesives, yet others are capable of providing strong bonds with only few pressure being applied during the cure. This type of adhesive is typically available in liquid, past and solid forms. They have a high mechanical strength, and thus they can be considered structural adhesives. Thermoplastic adhesives do not cure or set under heat. They can be melted with application of heat and then applied to the adherends, since thermoplastic molecules do not cure into a crosslinked structure. Thermoplastics have a long term deformation under load (due to a non-crosslinked structure), which prevents these adhesives from being used in structural applications. The temperature operating range is more limited than thermosetting adhesives. Thermoplastics are typically available in liquid and solid forms. Elastomeric adhesives are capable of high degrees of extension and compression. Indeed, this material returns to its original dimensions when unloaded due to having a three dimensional (3D) crosslinked network molecular structure. As result, they may absorb large amounts of energy and offer high strengths in bonded structures. Elastomeric adhesives may be either thermosetting or thermoplastic. Hybrid adhesives are made by combining thermosetting, thermoplastic or elastomeric resins, thus enabling combining the most useful properties of each component. Another method of classification is by the reaction or solidification:

chemical reaction, loss of solvent or water, or cooling from a melt. For instance, in thermoset adhesives the solvent is required to first evaporate and then cross-linking to occur before bonding. Classification thru physical form may distinguish adhesives in four major types: multiple part solvent (liquid or paste), one part solvent (liquid or paste), one part solution (liquid) or solid (powder, tape, film). Cost, although not being a classification method, is nowadays a decisive factor in adhesives' selection. When estimating the cost of using adhesives, not only the adhesive price should be accounted for, but also the design and fabrication to perform a reliable joint should be considered. Another option to categorize adhesives is by its chemical family, as shown in Table 1.

Table 1 – Structural and non-structural adhesives' families [11]

Adhesives			
Structural		Non-structural	
Epoxies	Epoxy resin	Elastomeric resins	Natural rubber
	Toughened epoxies		Asphalt
	Epoxy phenolic		Reclaimed rubber
	Epoxy nylon		Butyl rubber
	Epoxy polysulfide		Styrene rubber
	Epoxy vinyl		Neoprene
	Epoxy hybrids		Nitrile
Resorcinol formaldehyde			Polyisobutylene
Melamine			Polyvinyl methyl ether
Phenolics	Nitrile-phenolic		Silicone
	Vinyl-phenolic	Thermoplastic resins	Polyvinyl
	Neoprene-phenolic		Thermoplastic elastomers
Polyaromatic high temperature resins	Polyimide		Cellulosic resins
	Bismaleimide		Polyamide
	Polybenzimidazole		Polyester
Polyesters			Phenoxy
Polyurethanes			Acrylic
Anaerobic resins		Natural occurring resins	Glues of animal origin
Cyanoacrylates			Glues of agricultural resin
Modified acrylics			Sodium silicate
			Phosphate cement
			Sulfur cement

2.2 Strength prediction of bonded joints

This section presents an overview of the most relevant analytical and numerical methods for the strength prediction of bonded joints. The analytical analysis of bonded joints began about eighty years ago with Volkersen [20]. This model is an analytical approximation based on a simple model of a SLJ. After being presented, this model has been continuously improved to approach the real behaviour of bonded joints [21].

2.2.1 Analytical methods

Volkersen's method [20] is the most simple and limited method to obtain shear stresses in a SLJ. This solution is represented in Figure 14. Shear stresses in the adhesive are maximum at the overlap edges and minimum at the inner portion of the bond.

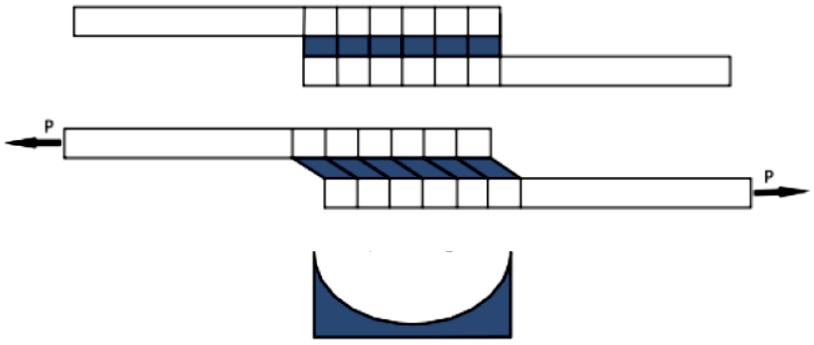

Figure 14 – Specimen without load (up), specimen with load (middle), shear stress in adhesive layer (down) [8]

The Goland and Reissner's [22] analysis took into account the fact that the load (*P*) represented in Figure 14 is non collinear, therefore creating a bending moment that promotes the joint's transverse deflection. The displacements are no longer proportional to the load, which results in a geometrical non-linearity. The results of this model were very similar to those of Volkersen regarding shear stresses, but this analytical formulation also allows to obtain peel stresses, as shown in Figure 15.

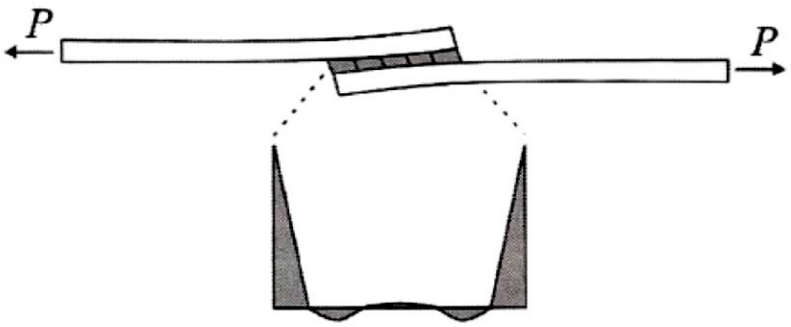

Figure 15 - Peel stresses in the adhesive by the Goland and Reissner's analysis [8]

The analysis of Hart-Smith [23] goes further and considers that, beyond elastic deformation, adhesives and adherends also have plastic deformations. This method shows that the adhesive's plasticity increases the strength of a joint compared with an elastic analysis because, when the material plasticizes, a redistribution and a peak reduction of stresses occur, and failure takes longer to occur. Hart-Smith chose an elasto-plastic model and showed that the actual form of the adhesive´s load-displacement (*P-δ*) curve was less important than the area under it (which represents the dissipated energy). Therefore, an elastic-perfectly plastic response was assumed (Figure 16).

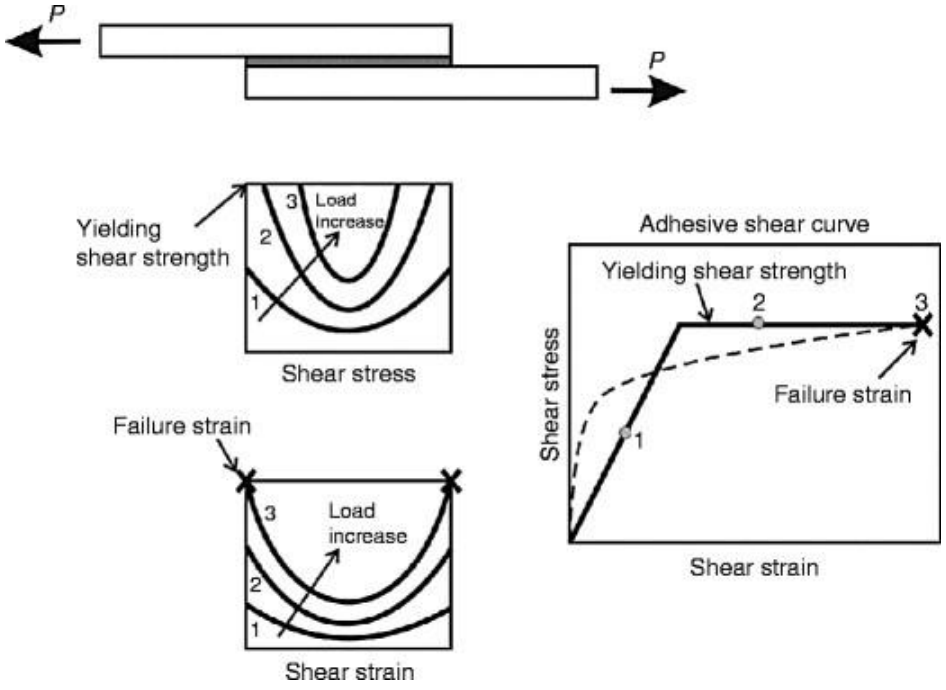

Figure 16 – Hart-Smith analysis [2]

Renton and Vinson [24] made another significant contribution to the analysis of SLJ. They used balanced SLJ boundary conditions based on Goland and Reissner's formulation for the overlap bending moment, but they included thermal strains in the formulation and the adhesive layer was modelled as a separate block. This enables the adhesive shear stress to drop rapidly to zero at the overlap edges.

Ojalvo and Eidinoff [25] incorporated a complete description for the adhesive shear strain that allows for a linear variation across the adhesive thickness. Substrate shearing has not been included. The authors showed that shear stresses could exhibit a significant variation across the overlap at the joint ends.

Allman [26] and Chen and Cheng [27], using models based on the two dimensions (2D) elastic theory, assumed a linear variation of peel stresses and constant shear stresses across the adhesive thickness. Adams and Mallick [28], and then Zhao and Lu [29], developed models in which both the adhesive and adherends are described as elastic

media. Their models can be applied in joints with thick adhesives, although analytical solutions of composite joints are too complicated with this model [2].

Yang and Pang [30] further developed a model for SLJ including asymmetric laminates, and all three stress components in the adhesive were obtained thru a Fourier series approach.

Several authors developed other methods to establish strength prediction of SLJ as well as other joint configurations. In order to provide design analysis for a wide range of structures, capable of modelling non-linear adhesive behaviour, general structural analysis packages were developed. These analyses were restricted to just one overlap region. Crocombe [31] developed a package known as SAAS (stress analysis for adhesive structures) and, in order to promote the versatility of the analysis, FE principles were implemented. GLUEMAKER® was another approach to facilitate FE analyses. It is a pre-processor for commercial FE codes such as ABAQUS® [14].

2.2.2 Numerical methods

Despite the continuous improvement of analytical methods, the appearance of new and complex adhesives leads to a high complexity of the analysis, which many time requires a non-analytical solution. Under these conditions, numerical methods are more adequate. This section reports the main strength prediction techniques that can be applied to bonded joints.

2.2.2.1 Continuum mechanics

The continuum mechanics approach uses the maximum values of stress, strain or strain energy predicted by an FE analysis or analytical methods and compares them with the corresponding material allowable values to assess failure [1]. Ignoring all the other principal stresses, initially, the maximum principal stress (MAXPS) was used for the strength prediction of brittle materials, because it is the most responsible for the failure of this kind of materials. Adams et al. [15] used this criterion with success. Nonetheless, care must be taken when using this criterion, because of the singularity of stresses at re-entrance corners of the joint. It is known that, a small amount of rounding at the adherend corners eliminates the singularity point, and this may affect the stress distributions in that area and also the joint strength. Zhao et al. [32, 33] studied the effect of adherend rounding (Figure 17) and showed that the stress singularity became nil with a small degree of rounding, as presented in Figure 18.

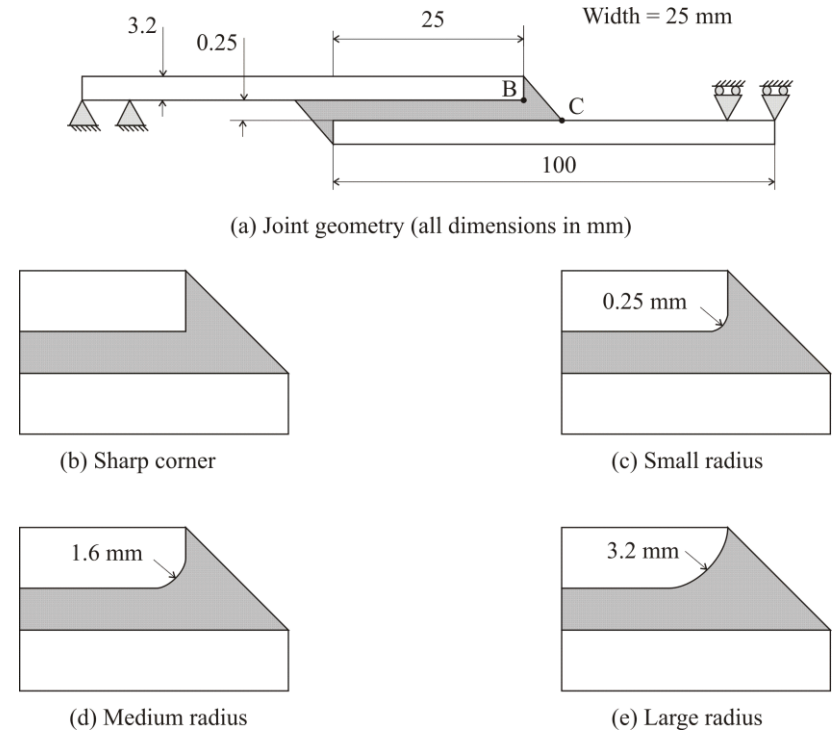

Figure 17 – SLJ with different degrees of rounding [32]

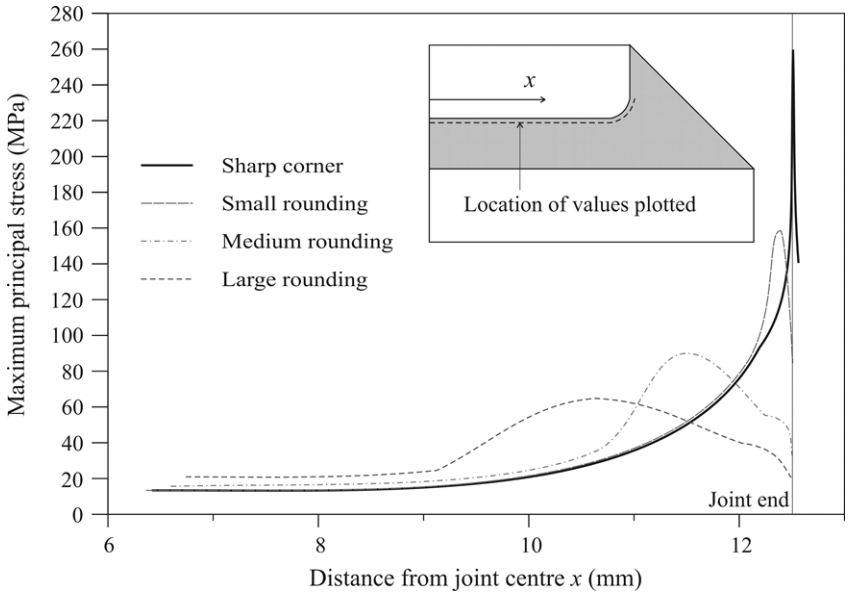

Figure 18 – Maximum principal stresses in the adhesive close to the unloaded adherend [32]

Shear stresses have also been used for strength prediction. da Silva et al. [21, 34] showed for SLJ that this criterion is only valid for brittle adhesives and short overlaps. For ductile adhesives, which can endure large loads after adhesive yielding, the criterion of maximum principal strain (MAXPE) can be used. However, as well as the maximum principal stresses, this criterion is sensitive to mesh the size. Hart-Smith [23] proposed that the maximum shear strain might be used as a failure criterion when plastic

deformation was apparent. da Silva et al. [21, 34] showed, for SLJ, that the maximum shear strain criterion is very accurate for ductile adhesives. The above mentioned criteria are applicable to continuous structures only.

2.2.2.2 Fracture mechanics

Continuum mechanics assumes that the structure and its materials are continuous. However, defects in structures or two materials with re-entrant corners constitute a structural discontinuity. Continuum mechanics gives no solution for these cases. Therefore, fracture mechanics has been developed. With this approach, it is well accepted that stresses calculated by using continuum mechanics are singular at the crack tip. Figure 19 helps to explain why these singularities exists.

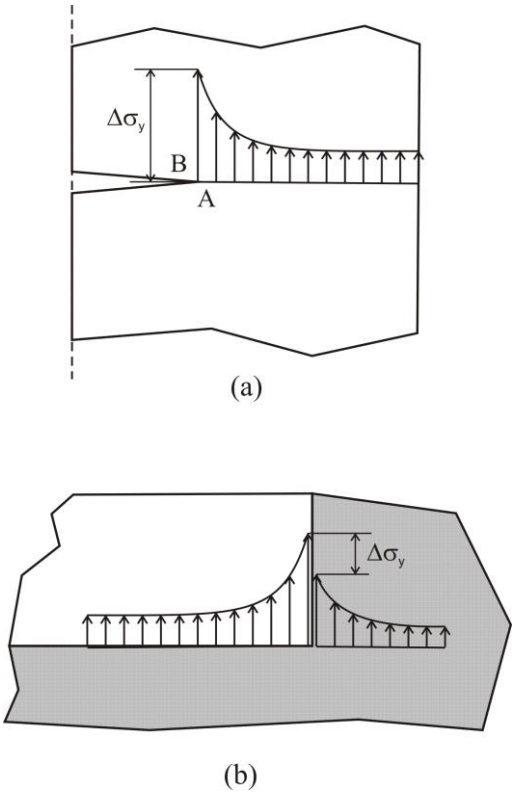

Figure 19 – Stress discontinuity around (a) a crack tip and (b) at a re-entrant corner [1]

The normal y-stresses, σ_y, must be finite, instead of infinite as theory predicts. However, σ_y stresses into the crack and away from the tip of the crack are nil because of the free surfaces. Therefore a discontinuity exists at point A. The continuum mechanics criterion requires all the stresses to be continuous, fact that is not observed at the crack tip. As a result, stresses at the crack tip must be finite, instead of infinite (as theory predicts). Williams [35] found that a singularity always exists when the crack angle is < 180°. Actually, the stress discontinuity still exists, but free surfaces do not [1]. Fernlund and Spelt [36] and Shahin and Taheri [37], among others, used the strain energy release rate,

G, and respective critical value or fracture toughness, G_C, instead of stress intensity factors. However, fracture of adhesive joints typically takes place under mixed-mode. Failure criteria for mixed mode fracture can be developed similarly to the classical failure criteria, although the mixed-mode loadings obliges to take into account the toughness in tension, G_{Ic}, and toughness in shear, G_{IIc}. Failure criteria for mixed-mode fracture can be developed in a way analogous to the classical failure criteria, although the fracture surface (or envelope) concept must be introduced. Various mathematical surface functions were proposed such as the 3D criterion by Dillard et al. [38]

$$\left(\frac{G_I}{G_{IC}}\right)^{\alpha}+\left(\frac{G_{II}}{G_{IIC}}\right)^{\beta}+\left(\frac{G_{III}}{G_{IIIC}}\right)^{\gamma}=1, \quad (1)$$

where G_I, G_{II} and G_{III} are the values of G under pure tension, shear and tearing modes, respectively, and G_{IC}, G_{IIC} and G_{IIIC} are the respective critical values. The linear energetic criterion (α=β=γ=1) and the quadratic energetic criterion (α=β=γ=2) are the most used. Constructing such envelopes involves fitting with experiments, or assuming a pre-established shapes, although the fitting method does not help much to understand the physical failure mechanism of mixed mode fractures. When materials deform plastically, the linear elastic fracture mechanics (LEFM) concepts have to be extended into elasto-plastic fracture mechanics. Rice and Rosengren [39] proposed the J-integral to solve those problems. The J-integral has been successfully used by researchers to predict the joint strength of cracked adhesive joints

$$J=\int_c w dx_2 - T_j \frac{\partial u_j}{\partial x_1} dS, \quad (2)$$

where C is the curve surrounding the crack tip, S indicates the arc length, W the energy density, T_j is the traction vector, u_j the displacement vector and x_1 –x_2 is the coordinate system. However, this approach may not be used as a strength criterion for joints without a pre-crack [1].

2.2.2.3 Cohesive zone models

The computer implementation of LEFM techniques had a great success some decades ago, but these are limited to the elastic behaviour of materials. Moreover, modern toughened adhesives usually develop plastic zones larger than the adherends' thickness, which requires a proper technique to overcome this problem. Barenblatt [40, 41] and Dugdale [42] proposed the concept of cohesive zone to describe damage under static load at the cohesive process zone ahead of the apparent crack tip. Since then, CZM were improved and tested to simulate crack initiation and propagation even in composite delamination [43]. CZM are based on spring [44] or more typically cohesive elements

[45], connecting 2D or 3D elements of structures. CZM can be easily incorporated in FE softwares to model the fracture behaviour in various materials. CZM are based on the assumption that a fracture can be artificially introduced in structures, in which damage growth is allowed by the introduction of a possible discontinuity in the displacement field. This technique consists of the establishment of traction-separation laws to model interfaces or finite regions.

CZM reproduce the damage along a given path, disregarding the phenomena on the origin of failure establishing a traction-relative displacement (t-δ), by specification of several parameters ruling the crack growth process such as G_{IC}, G_{IIC} or G_{IIIC} [33]. The traction-separation laws are typically represented by linear relations at each one of the loading stages [46]. Figure 20 presents the 2D triangular CZM model actually implemented in Abaqus® for static damage growth in pure and mixed-mode.

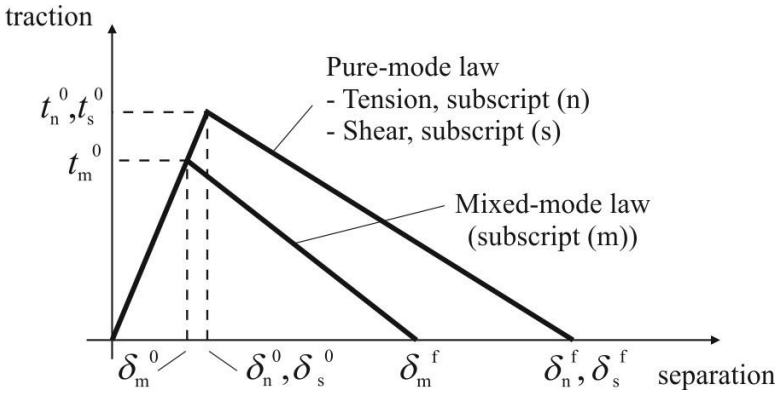

Figure 20 – Triangular traction-separation law (adapted from Abaqus® [47])

The subscripts s and n relate to pure normal (tension) and shear behaviours, respectively. t_n and t_s are the corresponding current stresses, and δ_n and δ_s the current values of δ. G_I and G_{II} along the fractures path and respective values of G_{IC} and G_{IIC} are required. The cohesive strengths must be defined (t_n^0 for tension and t_s^0 for shear), cancelling the elastic behaviour and leading to the initiation of stress softening. δ_n^0 and δ_s^0 are the peak strength displacements, and δ_n^f and δ_s^f the failure displacements. For the mixed-mode model, t_m^0 is the mixed-mode cohesive strength, δ_m^0 the corresponding displacement, and δ_m^f the mixed-mode failure displacement. Under pure-mode loading, the damage initiation occurs at the cohesive strength (t_n^0 or t_s^0) and, when the values of t became nil, the crack propagates up to the adjacent pair of nodes in the failure path allowing the gradual debonding between crack surfaces. Under mixed-mode loading, stress and/or energetic criteria are often used to combine the pure-mode laws. Thru those principles, the complete failure response of structures may be simulated [48]. CZM has more utility than conventional fracture mechanics, as it does not need an initial flaw. CZM extends the concepts of continuous mechanics by including a zone of discontinuity by means of a CZM path. CZM has been used to simulate the behaviour of structures up to failure. The knowledge of the spot were damage will start is not

necessary, although cohesive elements must exist at the planes where damage could occur, which in some cases is not easy to know beforehand. However, an important feature of adhesively bonded joints, that helps to overcome the issue, is that damage propagation is restricted to well defined plans (at or near the adhesive/adherend interfaces, or cohesively in the adhesive bond) [49].

2.2.2.3.1 Cohesive law shapes

Over the years several models were developed include triangular [50], linear-parabolic [51], polynomial [52], exponential [53] and trapezoidal laws [54]. In order to faithfully simulate the behaviour of thin material strips or interfaces, the shape of CZM laws can be adjusted. Figure 21 presents those CZM models used for strength prediction of different materials.

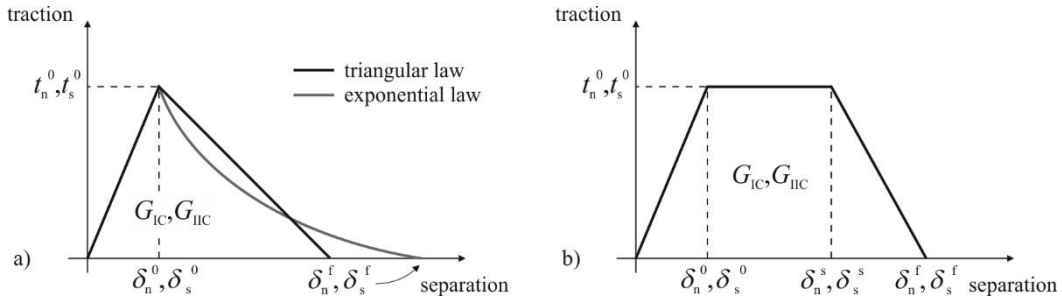

Figure 21 – Different shapes of pure mode CZM laws: triangular or exponential (a) and trapezoidal (b)

For the represented trapezoidal CZM, δ_n^s and δ_s^s are the stress softening onset displacements. Campilho et al. [49, 55], in order to simulate ductile adhesives, considered trapezoidal softening laws. Other study from Pinto et al. [56] concluded that, for stiffer adherends, a precise shape of the cohesive law is fundamental for the accuracy of the results and *P-δ* response of the structure and also that the *P-δ* curve precisely follows the shape of CZM law.

At a glance, the trapezoidal law is often preferred for ductile adhesives [45, 57] and a triangular CZM is normally used for brittle materials that do not plasticize before failure [58]. The material behaviour should always be the main factor for the choice of the most appropriate CZM law shape.

2.2.2.3.2 Damage initiation and growth criteria

Damage initiation refers to the beginning of degradation of the cohesive response at a contact point. The process of degradation begins when the contact stress and/or contact separation satisfy certain damage initiation criteria. Each damage initiation criterion has an output variable associated with it, to indicate whether the criterion is met. A value of one or higher denotes that the initiation criterion has been met. Several damage

initiation criteria are available, mainly divided in two groups: stress and strain based. Within the stress-based damage initiation criteria, one that depends upon maximum contact stress ratio is denominated MAXS (maximum nominal stress), expressed as [47]:

$$\max\left\{\frac{\langle t_n\rangle}{t_n^0}, \frac{t_s}{t_s^0}\right\}=1. \tag{3}$$

$\langle\ \rangle$ are the Macaulay brackets, emphasizing that a purely compressive stress state does not initiate damage [59].The quadratic nominal stress criterion (QUADS), based on contact stress ratios, states that damage initiates upon fulfilment of the equation (4) [47]:

$$\left\{\frac{\langle t_n\rangle}{t_n^0}\right\}^2+\left\{\frac{t_s}{t_s^0}\right\}^2=1, \tag{4}$$

The last strength-based criteria relies upon maximum principal stresses (MAXPS), predicts damage initiation by [47]:

$$\left\{\frac{\langle \sigma_{max}\rangle}{\sigma_{max}^0}\right\}=1. \tag{5}$$

σ_{max} and σ_{max}^0 represent the current and the allowable maximum principal stress. All criteria (MAXS, QUADS, and MAXPS) evaluate stress ratios between a given stress value and the peak nominal stress.

For the strain-based criteria, the maximum nominal strain criterion (MAXE) assumes damage initiation upon veracity of equation (6) [47],

$$\max\left\{\frac{\langle \varepsilon_n\rangle}{\varepsilon_n^0}, \frac{\varepsilon_s}{\varepsilon_s^0}\right\}=1, \tag{6}$$

where ε_n and ε_s are the current tensile and shear strain, respectively. ε_n^0 and ε_s^0 are corresponding peak strains. The quadratic nominal strain criterion (QUADE) is assessed by [47]:

$$\left\{\frac{\langle \varepsilon_n\rangle}{\varepsilon_n^0}\right\}^2+\left\{\frac{\varepsilon_s}{\varepsilon_s^0}\right\}^2=1. \tag{7}$$

The last initiation criteria is based on the maximum principal strain (MAXPE), expressed by [47]:

$$\left\{\frac{\langle \varepsilon_{max} \rangle}{\varepsilon_{max}^{0}}\right\} = 1. \quad (8)$$

ε_{max} and ε_{max}^{0} represent the current and the allowable maximum principal strain. The MAXE, QUADE and MAXPE criteria evaluate the strain ratios between a given strain value and the peak nominal strain.

By the fulfilment of one above mentioned criteria, the material stiffness initiates a degradation process. Complete separation and failure displacement are predicted by a damage evolution law that describes the rate at which the cohesive stiffness is degraded. It can be defined based on the energy that is dissipated as a result of the damage process. The fracture energy is equal to the area under the traction-separation curve (Figure 20). The dependence of the fracture energy on the mode mix can be defined based on a power law fracture criterion. The power law criterion states that failure under mixed-mode conditions is governed by a power law interaction of the energies required to cause failure in the individual (normal and shear) modes. It is given by the expression [47],

$$\left\{\frac{G_I}{G_{IC}}\right\}^{\alpha} + \left\{\frac{G_{II}}{G_{IIC}}\right\}^{\alpha} = 1, \quad (9)$$

where α is the power law parameter, G_I and G_{II} relate to the work done by the traction and corresponding relative displacements in the normal and shear directions, respectively, whilst the relating critical fracture energies required for pure mode failure are given by G_{IC} and G_{IIC} for normal and shear loadings, respectively.

Another damage evolution law, the Benzeggagh-Kenane (BK) [60] fracture criterion is particular useful when the critical fracture energies during deformation purely along the first and the second shear directions are the same; i.e., G_{IIC}=G_{IIIC}. It is given by:

$$G_{IC} + \left(G_{IIC} + G_{IC}\right)\left\{\frac{G_S}{G_T}\right\}^{\eta} = G_C, \quad (10)$$

where G_S=G_{II} + G_{III}, G_T=G_I + G_S and η is a characteristic material parameter.

2.2.2.3.3 Influence of the cohesive law shape on the joint strength

Few works analysed the effect of the cohesive law shape used to model the adhesive layer on the strength of SLJ. This section reports the findings of one of these works [61], whose results are consistent with the general published data on this matter. In the reported work, the effect of the cohesive law shape (triangular, linear-exponential or

trapezoidal) of the adhesive layer on the accuracy of the strength prediction is established. Unidirectional carbon-epoxy pre-preg (SEAL® Texipreg HS 160 RM) with 0.15 mm thickness was considered for the composite adherends of the SLJ, with the $[0]_{16}$ lay-up. Two epoxy adhesives were considered: Araldite® AV138 and Araldite® 2015. The SLJ geometry and characteristic dimensions are represented in Figure 22. The following dimensions were considered (in mm): L_O=10-80, width b=15, total length between gripping points L_T=240, adherends thickness t_P=2.4 and adhesive thickness t_A=0.2. Eight different values of L_O were evaluated (10, 20, 30, 40, 50, 60, 70 and 80 mm). For each value of L_O, six specimens were tested, with at least four valid results.

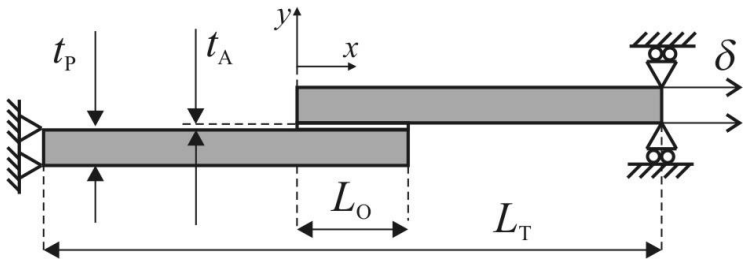

Figure 22 – Geometry and characteristic dimensions of the SLJ specimens [61]

The Finite Element Method (FEM) software Abaqus® was considered for this study, to evaluate the modelling accuracy of its CZM embedded formulation when stipulating different CZM shapes to model the adhesive layer in SLJ. The adhesive layer was modelled with a single row of cohesive elements [58] and a damage model between each set of paired nodes with varying CZM shape. Figure 23 details the CZM laws with different shapes for the adhesives AV138 and 2015 in tension (a) and shear (b).

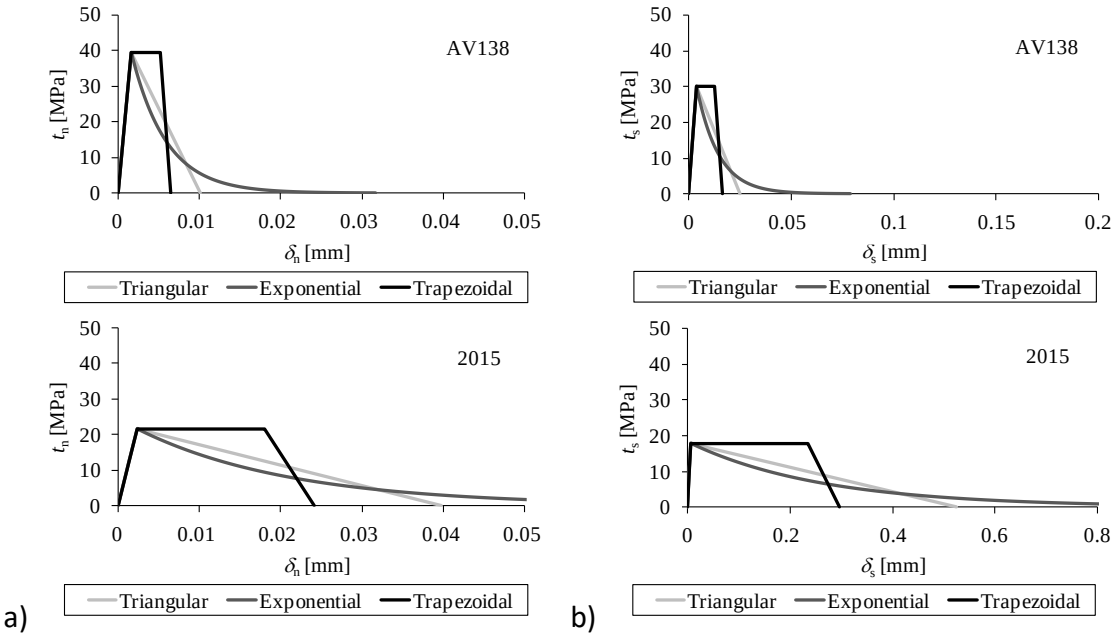

Figure 23 – CZM laws in tension (a) and shear (b) for both the adhesives tested [61]

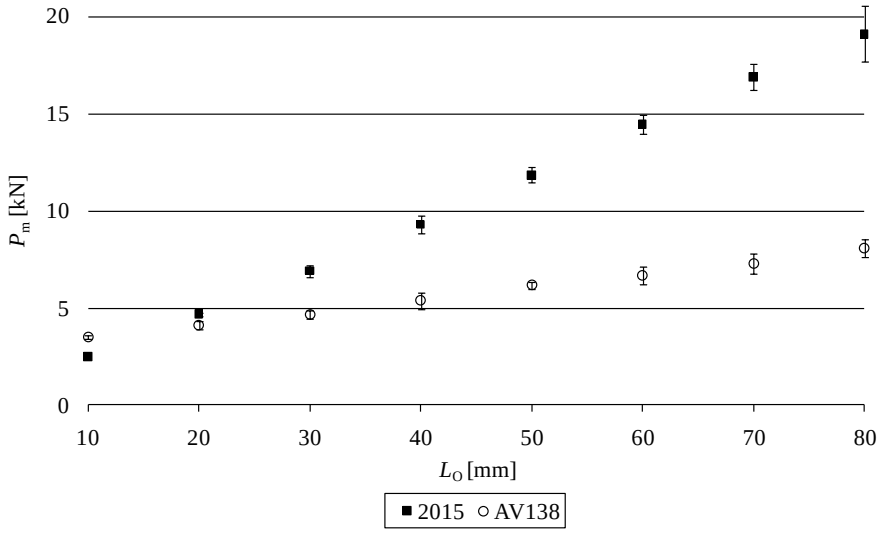

Figure 24 – Experimental plot of the P_m-L_O values for the adhesives AV138 and 2015 [61]

Figure 24 reports P_m as a function of L_O for both adhesives tested, showing a nearly linear increase of P_m with L_O. The non-existence of a limiting P_m value in the P_m-L_O curves is justified by the high strength of the carbon-epoxy adherends (i.e., the tensile strength of the laminates was not attained for the tested L_O values up to failure in the adhesive layer). The CZM law shape influence on the strength predictions was carried out considering triangular, linear-exponential and trapezoidal CZM, for a perception of the influence of this choice on the accuracy of the FEM simulations under different material/geometrical conditions.

SLJ with the ductile adhesive

Figure 25 reports the percentile deviation (Δ) between the experimental and FEM P_m values for the adhesive 2015 (averaged by the respective experimental P_m values). The slight inconsistent trend of the P_m-L_O plots is related to the calculation process to average experimental data, giving natural oscillations.

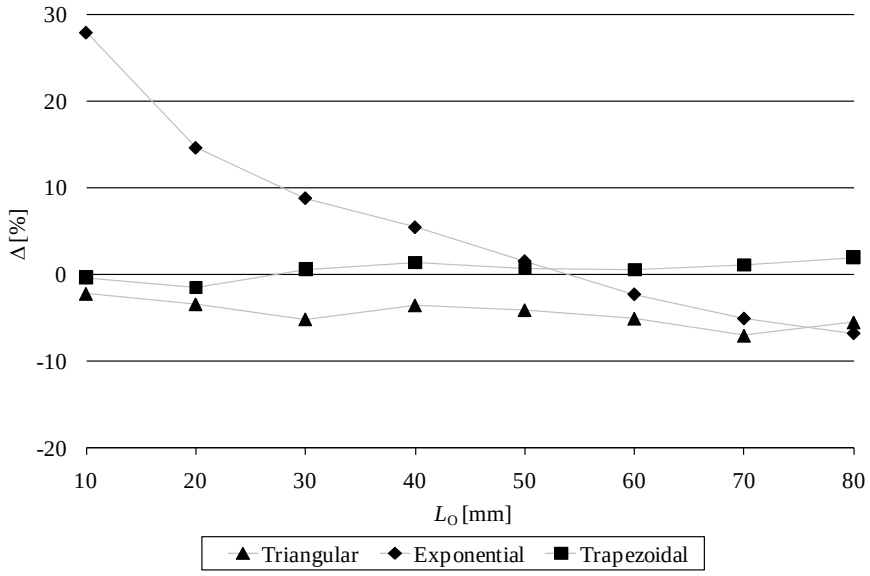

Figure 25 – Percentile deviation between the experimental and FEM P_m values for the adhesive 2015 [61]

Results show that the trapezoidal law approximates the best the experimental data. The percentile errors between the experimental and FEM data are negligible, with a maximum of 1.9% for L_O=80. These results are consistent with previous observations for these types of adhesives [49, 62]. The use of a triangular law showed to consistently underestimate P_m, with a clear tendency for bigger discrepancies with larger values of L_O (Δ=-2.2% for L_O=10 mm, growing steadily for bigger L_O values; Δ=-5.5% for L_O=80 mm). The described tendency is justified in light of the typical stress distributions (namely shear stresses) for SLJ. As a fact, for small values of L_O, the nearly constant level of shear stresses between overlap ends [9] makes the CZM law shape practically irrelevant because, at the time P_m is attained, the adhesive is evenly loaded in all its length. In the FEM analyses, this corresponds to a scenario in which the stress levels are close to $t_{n,s}^0$ along the entire bond, which renders the softening shape of the CZM law not so important. With bigger values of L_O the stress gradients increase [9] and the deviation to the experimental data enlarges as well. Despite the variations to the experimental results, the triangular law still manages to predict P_m with an acceptable accuracy, which is an important feature to mention, as it is the easiest CZM law to use in terms of implementation, time of calculation, CZM parameter definition and availability in commercial FEM codes. The linear-exponential CZM gave opposite results for the range of L_O values evaluated. For small values of L_O, P_m was numerically overestimated (maximum Δ of 27.9% for L_O=10 mm). The Δ values consistently reduced and approached the experimental results for L_O=50 mm. From this point, under predictions of P_m were obtained with exponential softening (reaching Δ=-6.8% for L_O=80 mm). Analysis of the FEM results showed that the overestimation of P_m for the smaller L_O values is due to the following motives:

1- With the reduction of L_O, peel peak stresses develop at a larger normalized region of L_O [9]. With the increase of L_O, peel peak stresses concentrate at smaller normalized regions of L_O. This difference makes the preponderance of peel stresses not negligible for small L_O values. The over estimation of P_m for small L_O values is thus linked to the bigger value of δ_n^f for the linear-exponential law (Figure 23 a), which leads to failure at the overlap edges at higher values of P_m. The normalized peel stresses extension rapidly diminishes with the increase of L_O, reducing the error of the CZM predictions with the linear-exponential law.
2- With the reduction of L_O, owing to the bigger value of δ_s^f for the linear-exponential law induced by the steeper reduction of t_s after t_s^0 is attained, and also to a state of approximately constant shear stresses [9], the CZM elements of the inner overlap region at the time of failure show smaller degradation (i.e., higher transmitted loads), and thus the predicted P_m values artificially increase.

SLJ with the brittle adhesive

Figure 26 provides an identical comparison for the adhesive AV138, in which the oscillations are due to the aforementioned experimental variations. A large discrepancy can be readily observed in which regards the order of magnitude of Δ, since for the AV138 the maximum deviation is near 3%, compared to the approximate 30% for the 2015. On the other hand, the results of all the three CZM configurations follow the same tendency for the entire range of L_O values. This is related to the brittleness of the AV138, especially when compared to the large ductility of the 2015, which can be testified in Figure 23 by the disparity in the $\delta_{n,s}^f$ values. Actually, for the shear behaviour (Figure 23 b), δ_s^f for the 2015 is more than one order of magnitude higher than for the AV138. As a result of this difference, the CZM shape of the AV138 is much less influent because the region under softening is negligible compared to that of the 2015.

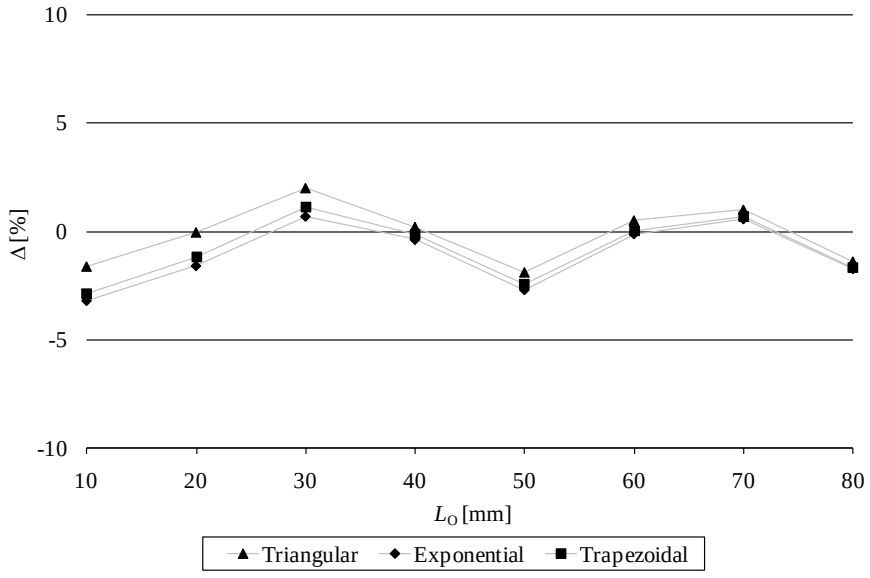

Figure 26 – Percentile deviation between the experimental and FEM P_m values for the adhesive AV138 [61]

Under brittle conditions, all the CZM shapes revealed to be accurate in predicting the measured response of the joints, although the best results (especially for small values of L_O) were found with the triangular law (maximum value of Δ of -1.9% for L_O=10 mm). Compared to these and the experiments, the trapezoidal results showed a slight under prediction (maximum Δ=-2.9% for L_O=10 mm). The linear-exponential CZM further under predicts P_m (maximum Δ=-3.2% for L_O=10 mm), although following the very same trend of the previously reported data.

As a conclusion regarding the different CZM shapes, these showed a significant influence on the results for the joints bonded with the 2015. These were more precisely modelled by the trapezoidal CZM that captured the adhesive plastic flow at the end of the elastic region, whilst the triangular CZM under predicted P_m up to Δ=-5.5% for L_O=80 mm. The linear-exponential CZM showed over predictions of P_m for short overlaps (up to 27.9%) and under predictions for long overlaps (up to -6.8%). For the AV138, the triangular CZM showed to be the most suited, although the results were very close between all CZM shapes tested (maximum deviations of -1.9%, -2.9% and -3.2% for the triangular, trapezoidal and linear-exponential CZM, respectively). As a result of this study, it was found that the influence of the CZM shape can be neglected when using brittle adhesives without compromising too much the accuracy, whilst for ductile adhesives this does not occur. Additionally, the smaller the value of L_O and the adhesive ductility, the greater is the influence of the CZM shape. In the end, the use of a CZM shape not suited to the material/interface to be simulated has to be balanced in these issues and expected variations in accuracy.

2.2.2.3.4 Influence of the cohesive parameters on the joint strength

Aiming to describe the effect of the cohesive parameters on the SLJ strength, a detailed work available in the literature [9] is reported in this subsection. In the mentioned study, the influence of the cohesive law parameters of a triangular CZM used to model a thin adhesive layer in bonded joints is addressed, to estimate their effect on the predictions. The adherends were fabricated from unidirectional carbon-epoxy pre-preg (SEAL® Texipreg HS 160 RM; Legnano, Italy) with 0.15 mm thickness plies and $[0]_{16}$ lay-up. The adhesive Araldite® 2015 (Basel, Switzerland), employed in this work, was previously characterized [63]. Figure 22 represents the joint geometry. The characteristic dimensions were defined as (in mm): L_O=10-80, b=15, L_T=240, t_P=2.4 and t_A=0.2. Eight different values of L_O were evaluated (10, 20, 30, 40, 50, 60, 70 and 80 mm). For each value of L_O, six specimens were tested, with at least four valid results.

The numerical analysis in the FEM package Abaqus® aimed to check the accuracy of its triangular CZM embedded formulation to predict the strength of adhesively-bonded SLJ and to evaluate the impact of cohesive parameter misjudgements on the strength predictions, either caused by intrinsic limitations of the data reduction techniques, or by different restraining scenarios between the characterization tests and the structures to

be simulated (e.g. t_A or t_P inconsistencies). The triangular CZM formulation was chosen for this analysis because of its simplicity, large use for investigation purposes and availability in Abaqus® including a mixed-mode formulation, which is absolutely necessary to model the SLJ used in this case study. However, other CZM shapes are available, such as the trapezoidal, which for this particular case would suit more faithfully the ductile adhesive behaviour [64]. The numerical analysis considered geometrical non-linear effects [64, 65].

The results show that all the joints experienced a cohesive failure of the adhesive layer. Figure 27 reports P_m as a function of L_O, showing an increase of P_m at a slightly decreasing rate with L_O [66, 67], although the P_m-L_O plot is nearly linear. As previously discussed, this occurs from the high stiffness of the adherends and ductility of the adhesive [68, 69]. The absence of a strength plateau in the P_m-L_O curve is justified by the high strength of the carbon-epoxy (i.e., the tensile strength of the laminates was not attained for the tested range of L_O values), and by the ductility of the adhesive that allowed a progressively larger redistribution of stresses in the adhesive layer up to the largest value of L_O, initiating at the loci of peak stresses, i.e., the overlap edges [70, 71]. In fact, since fracture was always abrupt, only with a negligible crack growth before P_m for the bigger values of L_O, it can be concluded that the adhesive plasticity always held up crack initiation at the overlap edges up to P_m, keeping these regions at the peak strength while stresses increased at the inner regions [69].

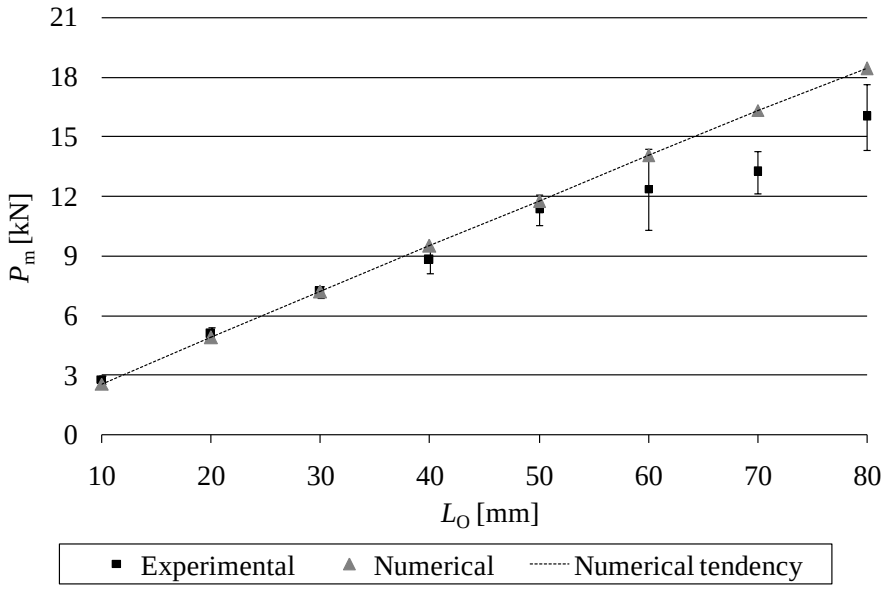

Figure 27 – Experimental and numerical comparison between the P_m values as a function of L_O [9]

The influence of percent variations of G_{Ic}, G_{IIc}, t_n^0, t_s^0, and their combined effect, on the value of P_m/P_m^0 of the joints is numerically assessed (P_m^0 represents P_m for the initial parameters). Percentile variations of the initial properties between -80 to +100% were considered, whilst the non-mentioned cohesive parameters in all analyses were kept

unchanged. The influence of each parameter on the damage laws is depicted in Figure 28 ((a) for G_{Ic} and the tensile law; (b) for G_{IIc} and the shear law) and Figure 29 ((a) for t_n^0 and the tensile law; (b) for t_s^0 and the shear law).

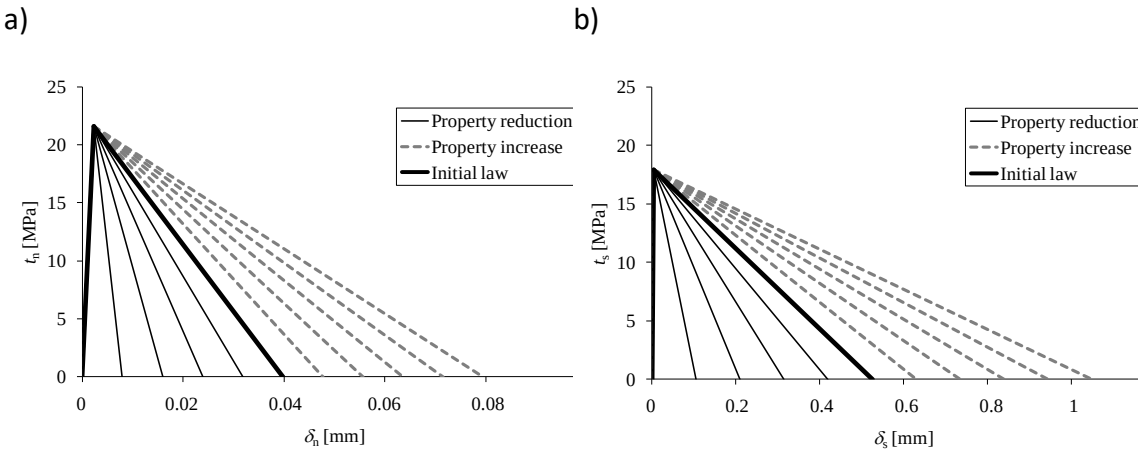

Figure 28 – Cohesive laws for values of G_{Ic} (a) and G_{IIc} (b) ranging from -80 to +100% of the initial ones, in increments of 20% [9]

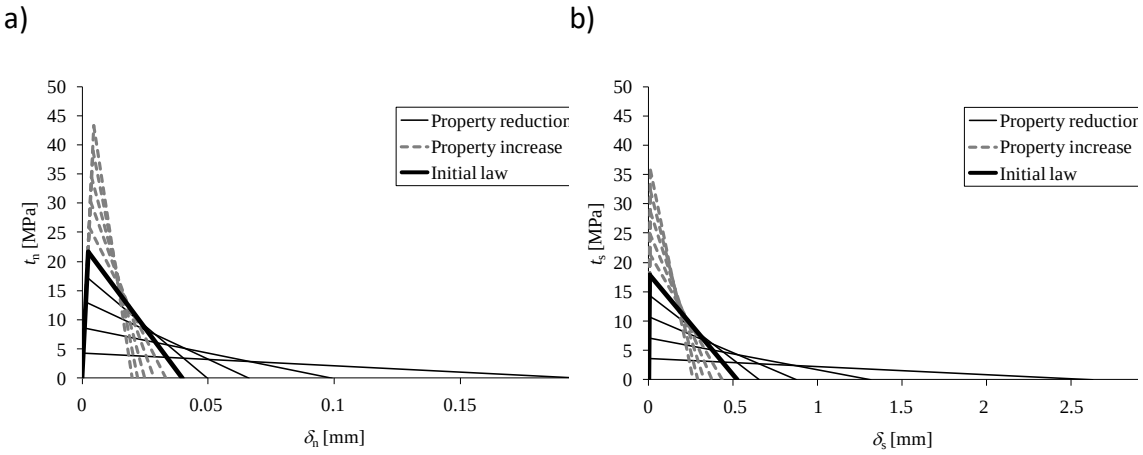

Figure 29 – Cohesive laws for values of t_n^0 (a) and t_s^0 (b) ranging from -80 to +100% of the initial ones, in increments of 20% [9]

Varying G_{Ic} or G_{IIc} changes the slope of the decaying portion of the respective cohesive law, while t_n^0 or t_s^0 remain identical. The modification of t_n^0 or t_s^0, by keeping the respective value of G_{Ic} or G_{IIc} unchanged, greatly changes the softening behaviour and value of δ_n^f or δ_s^f, respectively. As it will be discussed in detail in the following Section, the fluctuations of P_m/P_m^0 with G_{Ic} and G_{IIc} are justified by the variations of δ_n^f or δ_s^f of the damage laws by the modifications of these parameters (Figure 28) and the actual values of δ_n or δ_s along the entire bondline when P_m is attained, which determine the loads transmitted by the adhesive layer according to the established cohesive laws. On the other hand, the influence of t_n^0 and t_s^0 on P_m/P_m^0 will mainly depend on the value of t_m^0 (Figure 20), which is attained when the initiation criterion is fulfilled, and whose

value significantly changes by the modification of t_n^0 and t_s^0 in the same equation. Actually, by the variation of t_m^0, P_m/P_m^0 will be affected to an extent that depends on the values of δ_n and δ_s along the entire adhesive layer at the time of failure.

Fracture toughness

Figure 30, Figure 31 and Figure 32 describe the influence of percentile variations of G_{Ic}, G_{IIc}, and G_{Ic} plus G_{IIc}, respectively, on P_m/P_m^0. Figure 30, relating to G_{Ic}, shows a significant under prediction of P_m/P_m^0 for reductions of G_{Ic} (maximum of≈35.5% for an 80% reduction of the initial G_{Ic} and L_O=40 mm), occurring by the smaller values of δ_n^f (Figure 28 a) in the tensile cohesive law, which results on the premature failure at the overlap edges. A slight reduction of the reported under prediction is found near L_O=80 mm, since for bigger values of L_O the peak values of δ_n focus at a smaller normalized region at the overlap edges. The gradual increase of P_m/P_m^0 from L_O=30 mm to L_O=10 mm is accredited to the smaller values of δ_n at the overlap edges with the reduction of L_O, which leads to smaller actual values of δ_n in the tensile cohesive law when P_m is attained (Figure 28 a), rendering any under prediction of G_{Ic} less preponderant. Over predicting G_{Ic} gives minor improvements of P_m/P_m^0 (maximum of≈4.9% for L_O=50 mm) [62], equally smaller for shorter overlaps, due to the corresponding reduction of δ_n values. The negligible influence of the G_{Ic} over predictions, when compared to the under predictions, is also closely related to the sole attainment of large δ_n values (bigger than δ_n^f for the initial parameters; Figure 28 a) at the overlap edges, which renders any increase of G_{Ic} above its initial value not significant [62].

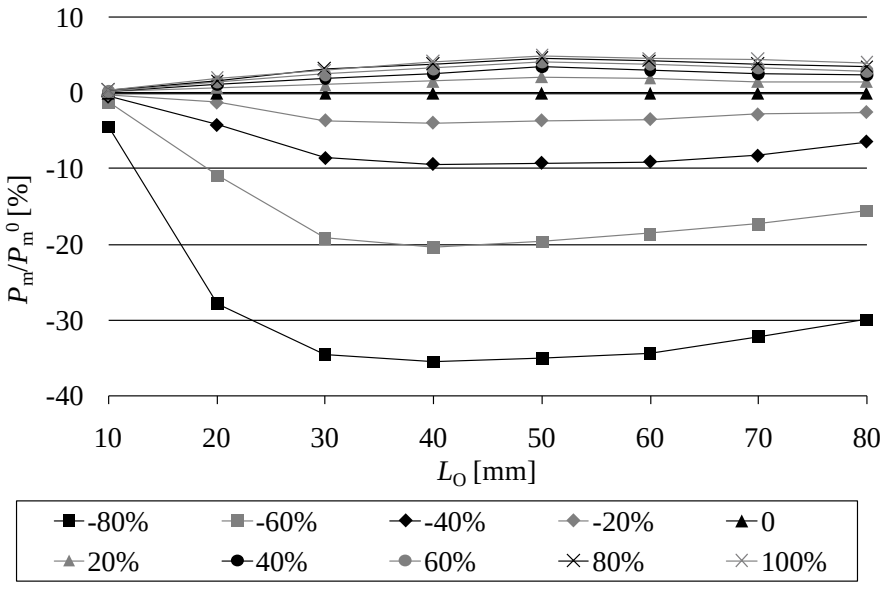

Figure 30 – Percentile variation of P_m/P_m^0 with G_{Ic} values ranging from -80 to +100% of the initial ones [9]

Figure 31 corresponds to G_{IIc} and depicts a significant difference to the data of Figure 30 (G_{Ic}), as P_m/P_m^0 varies nearly proportionally with L_O for under predictions of G_{IIc}. This is related to the more uniform values of δ_s along the bondline, compared to δ_n. As a result,

for small values of L_O the value of P_m/P_m^0 corresponds to a state of stress in which all the cohesive elements of the adhesive are very close to t_s^0 (Figure 20 and Figure 28 b). Thus, any modification to the shear cohesive law at $\delta_s>\delta_s^0$ does not reflect by a large amount on P_m/P_m^0. The increase of L_O steadily increases the gradients of δ_s along the bondline, associating P_m/P_m^0 to an increasing portion of the overlap with $\delta_s>\delta_s^0$ (at the overlap edges). As a result, the softening shape of the shear damage law becomes progressively more preponderant with L_O. The maximum reduction of P_m/P_m^0, of≈34.8%, was found for L_O=80 mm. On the other hand, identically to the G_{Ic} data, over predicting G_{IIc} only causes a maximum P_m/P_m^0 improvement of≈5.7% (L_O=80 mm) [62], because of the occurrence of large values of δ_s (bigger than δ_s^f for the initial parameters; Figure 28 b) at a restricted region at the overlap edges.

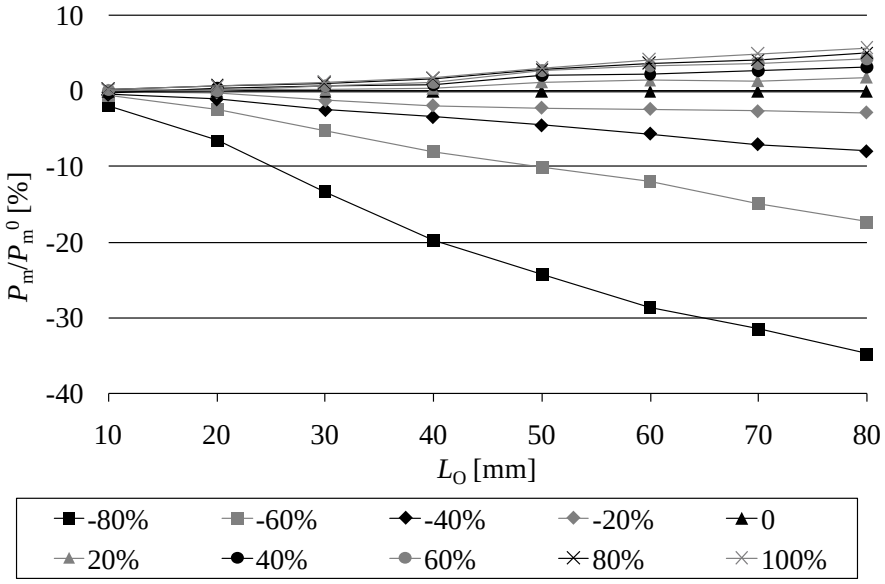

Figure 31 – Percentile variation of P_m/P_m^0 with G_{IIc} values ranging from -80 to +100% of the initial ones [9]

The combined modification of G_{Ic} and G_{IIc} (Figure 32) gives a reduced influence on P_m/P_m^0 between -20 and +100% of the initial values (maximum of≈9.3% for L_O=80 mm), and large reductions from -40 to -80% that attain its maximum, of≈44.5%, for L_O=80 mm. The value of P_m/P_m^0 increases from L_O=40 to L_O=10 mm, owing to the combined effect of G_{Ic} (Figure 30) and G_{IIc} (Figure 31). The bigger deviations of P_m/P_m^0, compared to Figure 30 and Figure 31, also relate to the joint influence of G_{Ic} and G_{IIc} on the failure process.

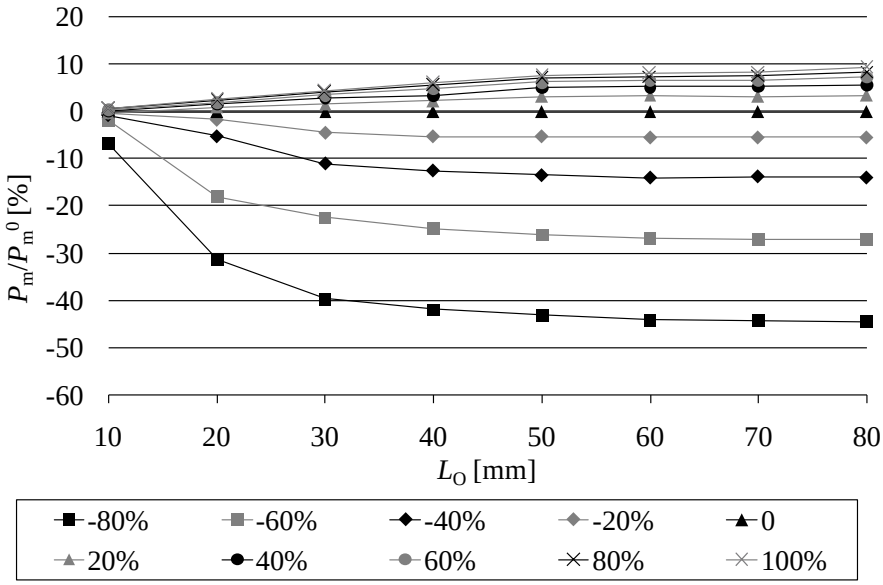

Figure 32 – Percentile variation of P_m/P_m^0 with G_{Ic} and G_{IIc} values ranging from -80 to +100% of the initial ones [9]

Cohesive strength

The influence of t_n^0 and t_s^0 on P_m/P_m^0 is shown in Figure 33, Figure 34 and Figure 35 for t_n^0, t_s^0 and t_n^0 plus t_s^0, respectively. The variation of these parameters also affects δ_n^f and δ_s^f (Figure 29) to keep G_{Ic} or G_{IIc} constant.

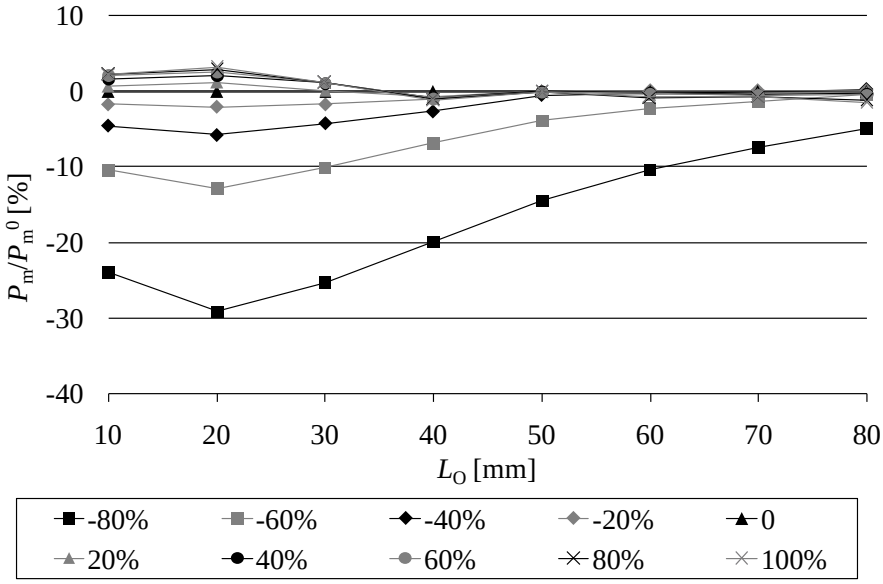

Figure 33 – Percentile variation of P_m/P_m^0 with t_n^0 values ranging from -80 to +100% of the initial ones [9]

Figure 33 displays a larger influence of t_n^0 on P_m/P_m^0 for the smaller values of L_O, for under and over predictions of t_n^0, due to the concentration of peel δ_n values at a larger normalized region at the overlap edges. With the increase of L_O, the concentration of

peel δ_n values occurs over a smaller normalized region, giving a less significant influence of t_n^0 on the global behaviour of the joints. Figure 33 also reports a much lesser influence on P_m/P_m^0 by over predicting t_n^0 than under predicting [62]. In both of these scenarios, these variations are closely related to the attainment of t_m^0 (Figure 20). Actually, the improvement of P_m/P_m^0 by over predicting t_n^0 (maximum of≈3.2% for L_O=20 mm) is related to the smaller influence of t_n stresses on the initiation criterion. Oppositely, the under prediction of t_n^0 is largely more preponderant on P_m/P_m^0 (maximum of≈29.1% for L_O=20 mm), owing to a premature occurrence of t_m^0 (Figure 20) by the larger influence of t_n on the failure process.

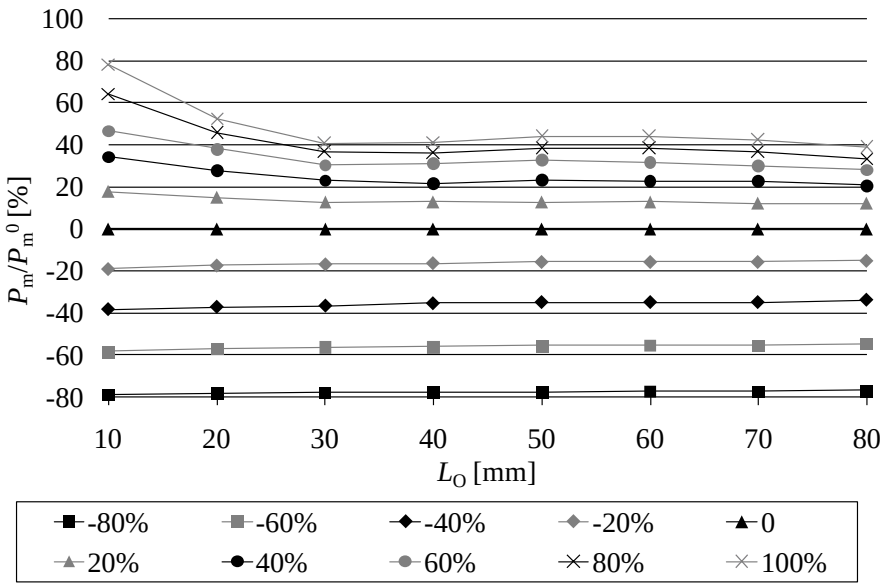

Figure 34 – Percentile variation of P_m/P_m^0 with t_s^0 values ranging from -80 to +100% of the initial ones [9]

Figure 34 depicts a nearly proportional percentile reduction of P_m/P_m^0 with t_s^0 notwithstanding the value of L_O (maximum of≈79.1% for L_O=10 mm). Actually, the transmission of loads through the adhesive is accomplished mainly by shear [72]. By reducing t_s^0, t_m^0 diminishes nearly proportionally at almost the entire overlap (see initiation criteria of Section 2.2.2.3.2), and P_m/P_m^0 follows the same tendency. This is valid either for small values of L_O, for which P_m/P_m^0 relates to small gradients of δ_s, and big values of L_O, corresponding to large δ_s variations. On the other hand, the improvement of P_m/P_m^0 with over predictions of t_s^0 is only close to proportional for L_O=10 mm (maximum of≈78.7% for L_O=10 mm and t_s^0 increase of +100%), due to the evenness of δ_s values along the overlap that result from a value of P_m/P_m^0 almost exclusively depending on t_s^0. For bigger values of L_O, owing to the enlarging δ_s gradients along the overlap, increasing t_s^0 results on higher load transfer for $\delta_s<\delta_s^0$ (δ_s^0 is the shear relative displacement at softening onset; Figure 20) and smaller or eventually nil load transfer for $\delta_s>\delta_s^0$ (Figure 29 b). As a result of these conflicting variations along the overlap when P_m/P_m^0 is attained, the improvement of P_m/P_m^0 is limited.

The combined influence of t_n^0 and t_s^0 (Figure 35) is identical to the sole effect of t_s^0 (Figure 34), but with a slightly bigger impact on P_m/P_m^0, especially for the smaller values of L_O (maximum improvement of≈90.0% and reduction of 79.4%, for the respective variations of t_n^0 and t_s^0 equal to +100% and -80%), because of the bigger importance of shear stresses on the joint strength than peel ones [72], and to a larger influence of t_s^0 on the results (Figure 34).

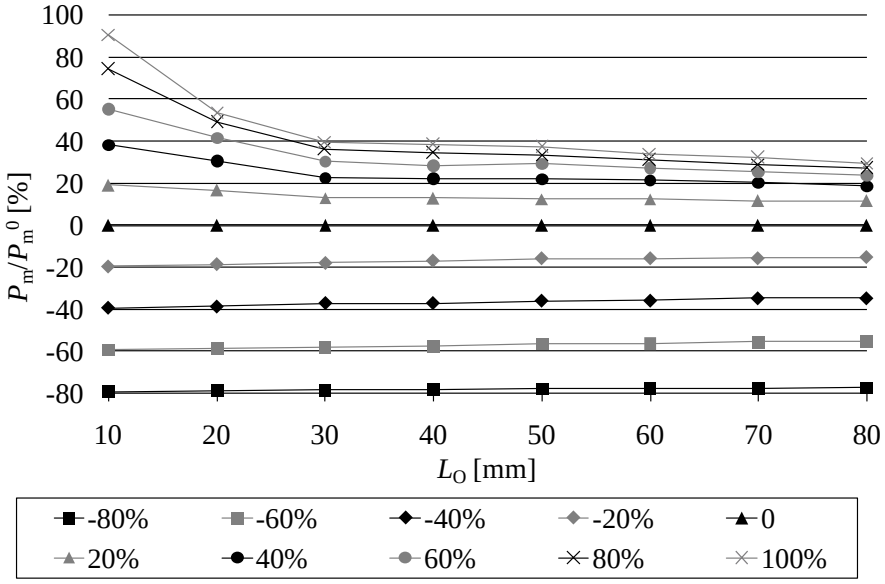

Figure 35 – Percentile variation of P_m/P_m^0 with t_n^0 and t_s^0 values ranging from -80 to +100% of the initial ones [9]

Combination of cohesive strength and fracture toughness

Figure 36 reports on the combined influence of similar percentile variations of G_{Ic}, G_{IIc}, t_n^0 and t_s^0 on P_m/P_m^0. The results show that the relationship is typically linear for under predictions of the cohesive parameters, following the overall tendency of Figure 35 (t_n^0 and t_s^0 have a higher influence on P_m/P_m^0 than G_{Ic} and G_{IIc}; Figure 32). As it regards to the increase of the cohesive parameters, the relationship is nearly proportional for L_O=10 mm, but it quickly diminishes for bigger values of L_O (maximum deviation for the L_O=80 mm joint: 100% improvement of the cohesive properties gives only a≈69.6% increase of P_m/P_m^0). This trend also resembles the results of Figure 35, relating to t_n^0 and t_s^0, but the increase was larger, since G_{Ic} and G_{IIc} were increased as well (as previously discussed, the fracture parameters play an important role for large values of L_O).

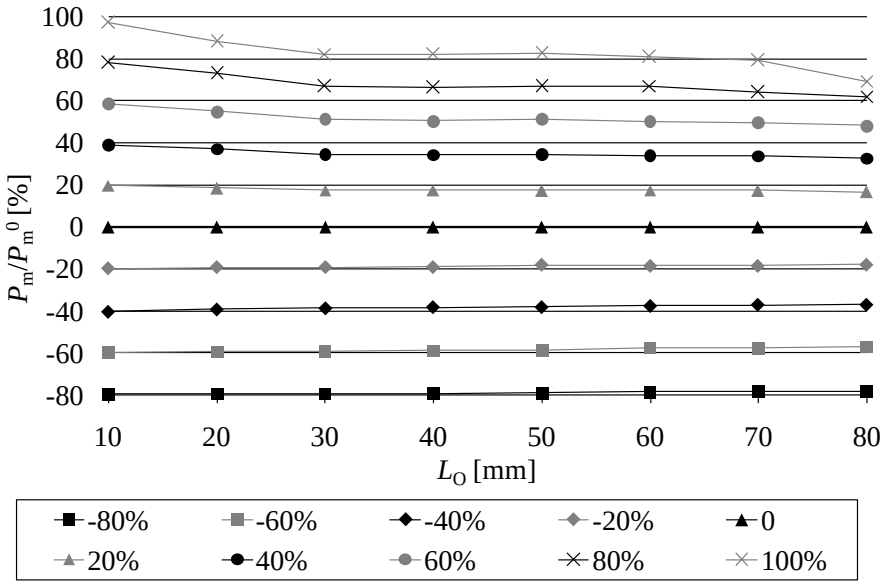

Figure 36 – Percentile variation of P_m/P_m^0 with G_{Ic}, G_{IIc}, t_n^0 and t_s^0 values ranging from -80 to +100% of the initial ones [9]

To conclude, the quantitative results presented in work study are solely applicable to the particular set of geometric and material properties selected, but they can qualitatively be extrapolated for different bonded geometries and materials. For the conditions tested, under predicting G_{Ic} and/or G_{IIc} is highly detrimental to the accuracy (maximum under prediction of≈44.5% for L_O=80 mm, by reducing G_{Ic} and G_{IIc} by -80% of the initial values), except for extremely small values of L_O. On the other hand, the over prediction of G_{Ic} and/or G_{IIc} only slightly affects the results (maximum over prediction of≈9.3% for L_O=80 mm; G_{Ic} and G_{IIc} improvement of +100%). Over predictions of t_n^0 are almost inconsequent (maximum of ≈3.2% for the L_O=20 mm joint and +100% improvement), but moderate variations are expected if this parameter is under predicted, especially for small values of L_O (maximum of≈29.1% for L_O=20 mm and -80% reduction). Opposing to t_n^0, t_s^0 largely influences the results with a nearly proportional relation between the under prediction of P_m/P_m^0 and the percentile variation of t_s^0 (maximum of≈79.1% for L_O=10 mm and -80% reduction). For over predictions of t_s^0, the improvement of P_m/P_m^0 is not so notorious, especially for large values of L_O (maximum of≈78.7% for L_O=10 mm and t_s^0 increase of +100%). The combined effect of t_s^0 and t_n^0 is close to that of t_n^0 (maximum improvement of≈90.0% and reduction of 79.4%, for the respective variations of t_n^0 and t_s^0 equal to +100% and -80%). The simultaneous variation of G_{Ic}, G_{IIc}, t_n^0 and t_s^0 gives values of P_m/P_m^0 in close proportion with the parameter percentile variations, except for over predictions and large values of L_O. In these circumstances, the improvement is not so significant, with a maximum deviation for L_O=80 mm (over prediction of≈69.6% and +100% properties improvement).

2.2.2.3.5 Methods to estimate the cohesive parameters

Different techniques are nowadays available for the definition of the cohesive parameters (G_{Ic}, G_{IIc}, t_n^0, t_s^0), such as the property identification method, the direct method and the inverse method [1].

The property identification technique consists of the separated calculation of each one of the cohesive law parameters by suitable tests. The method is particularly critical if bulk tests are used due to reported deviations between the bulk and thin adhesive bond cohesive properties [73]. However, in the property identification method, at least one cohesive parameter is approximated by consideration of bulk adhesive properties [56]. Campilho et al. [49] evaluated the tensile strength of bonded single-strap repairs on laminated composites as a function of the L_O and the patch thickness. For the estimation of the cohesive properties, several approximations were considered. Actually, the authors obtained t_n^0 and δ_n^s from the stress-strain (σ-ε) curve of the bulk adhesive, based upon authenticated evidences. One by Andersson and Stigh [73], which states that t_n^0 is of the same order of magnitude of the tensile strength measured in bulk testes. Other by the demonstration of Yang et al. [74], in which t_s^0 derivation from t_n^0 by the Von Mises yield criterion for bulk isotropic materials do not significantly influence the numerical results. Identically, δ_n^0 and δ_n^s do not significantly influence the numerical results. G_{Ic} and G_{IIc} values were estimated from double-cantilever beam (DCB) and end-notched flexure (ENF) tests, respectively. After evaluation, despite the above CZM parameters approximations, the authors found a reasonable agreement for the stiffness and failure load/displacement.

The direct method gives the precise shape and the complete CZM law by measuring the J-integral and crack tip normal or shear displacements thru differentiation of G_I or G_{II} with respect to the relative opening of the crack (δ_n or δ_s) [75]. Few works currently exist on CZM law determination by the direct method on adhesive bonds (e.g. Sørensen [76], Zhu et al. [25] and Campilho et al. [77]). Andersson and Stigh [73] used a direct method to determine the continuum CZM parameters in tension of a ductile adhesive in a DCB test configuration. The authors concluded that t_n-δ_n relationship can be divided in three parts. In the beginning, due to the linear elastic behaviour of the adhesive, t_n increases proportionally to δ_n until limit the stress is achieved. The second part is a plateau region that corresponds to the plasticity development in the adhesive, followed by a parabolic softening region (third part), giving an approximate trapezoidal shape. Carlberger and Stigh [78] determined the continuum CZM laws of a thin bond of a ductile adhesive in tension and shear using the DCB and ENF test configurations, respectively, considering $0.1 \leq t_A \leq 1.6$ mm. The values of G_I and G_{II} were derived by a J-integral formulation, given the large adhesive plasticity. Figure 37 shows the averaged CZM laws in tension for each value of t_A. The results clearly show the transition from an approximate triangular CZM law for small values of t_A to a trapezoidal law for bigger values.

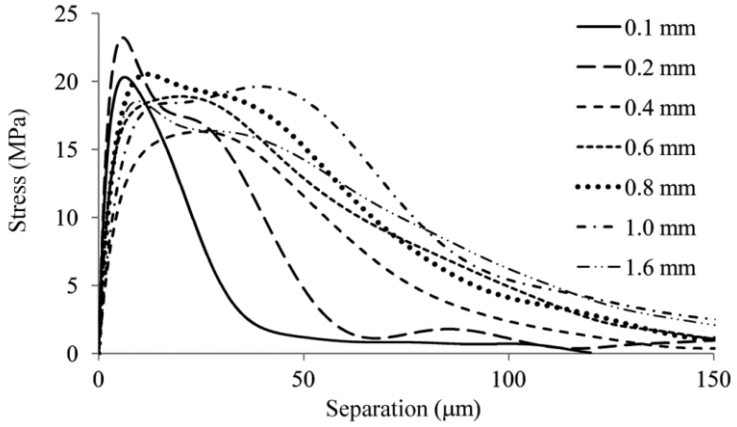

Figure 37 – CZM laws in tension for the adhesive Dow Betamate® XW1044-3 and $0.1 \leq t_A \leq 1.6$ mm [78]

Figure 38 presents the shear CZM laws. The results show an approximate triangular shape for t_A=0.1 mm and a modification to trapezoidal shape for bigger values of t_A. It was thus concluded that the CZM shapes significantly vary with t_A.

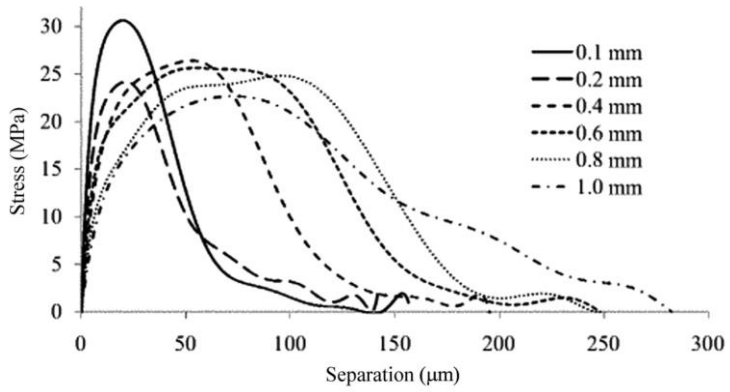

Figure 38 – CZM laws in shear for the adhesive Dow Betamate® XW1044-3 and $0.1 \leq t_A \leq 1.0$ mm [78]

Ji et al. [79], by a continuum CZM analysis, addressed the influence of t_A on t_n^0 and G_{IC} for a brittle epoxy adhesive considering the DCB specimen and the direct method for parameter identification. The G_{IC} measurement was made thru the analytical *J*-integral method. The authors concluded that this method for evaluation of G_{IC} and the direct method for the CZM law calculation give accurate and calibrated CZM law parameters for specific geometry and material conditions.

The inverse method consists of the estimation of the CZM parameters by iterative fitting the FE prediction with experimentally measured data (typically the *P-δ* curve), considering a precise description of the experimental geometry and approximated cohesive laws [80]. The inverse characterization of adhesive bonds should be applied individually for each tested specimen to account for slight geometry variations between specimens [55]. The value of G_{IC} or G_{IIC} is input in the FE model and, to completely define the CZM law, approximate bulk values can be used for t_n^0 or t_n^s (Figure 20) for the

initiation of the trial and error iterative process [81]. Examples of experimental data for the iterative fitting procedure are the *R*-curve [82], the crack opening profile [83] and the *P-δ* curve [84]. In the work of Campilho [81], for the definition of a shear CZM law by the ENF test, G_{IIC} was estimated by three methods: the compliance calibration method (CCM), the corrected beam theory (CBT) and the compliance-based beam method (CBBM). Data reduction by the three methods for five tested specimens showed similar CCM and CBBM results and smaller values for CBT. The CBBM values of G_{IIC} were used as input in the FE models and the remaining cohesive parameters (t_s^0 and δ_s^s) were estimated by fitting the experimental and numerical *P-δ* curves of each specimen. The authors found that the manual fitting process allowed to verify the influence of the CZM parameters on the FE *P-δ* curves' shape. The peak load is mainly influenced by G_{IIC}. Higher values of t_s^0 increase the peak load and the specimen stiffness up this value and δ_s^s has influence on the roundness of the *P-δ* curve near the peak value. This findings indicate that a unique solution for the shear CZM law of the adhesive could be provided by the inverse technique. In order to simplify the inverse fitting technique and estimate the local CZM parameters, Jung Lee et al. [85] used Single-Leg Bending (SLB) mixed-mode tests with tension or shear as dominant modes. The authors used a introduction of the design of experiment (DoE) and the kriging metamodel (KM) as an optimization technique. The mode-mixity was experimentally determined by using the classical beam theory. The G_{IC} and G_{IIC} values for each pure mode were calculated by a linear extrapolation of the obtained results. A mixed mode CZM was considered to replicate the tests. The estimation of the missing cohesive parameters (K_{nn}, K_{ss}, t_n^0 and t_s^0) was made by DoE and KM. Then the load difference between the numerical and experimental *P-δ* curves at several values of it are defined as an error function. The KM was constructed based on the sampling points of the cohesive parameters and the error function. In order to minimize the error, the cohesive parameters were obtained by applying a nonlinear optimization algorithm to the KM. The authors concluded that the proposed procedure accurately described the fracture behaviour of mixed-mode joints without additional tests (DCB for tension and ENF for shear characterization) as it is usually performed.

2.2.2.4 Damage mechanics

In these methods, a damage parameter is established to modify the constitutive response of materials thru a decreasing of stiffness or strength to represent the severity of damage material during loading. Literature examples that used properties degradation are found in thin adhesive bonds [86], composite delaminations or matrix failure [87]. This parameter can be used in a damage evolution law to model pre-cracking damage and crack growth. The damage variables can be categorized in two main groups, one that predicts the amount damage by redefinition of the material constitutive properties, and other considering variables linked to a specific kind of damage, such as porosities [88]. By damage mechanics techniques the growth of damage is defined as a

function of the load for static modelling [89] or cycling count for fatigue analyses [90]. Compared to fatigue CZM, damage mechanics techniques do not provide a clear distinction between fatigue initiation and propagation phases [86]. Nonetheless, these may be recommended if the damage is more widespread or the failure path is not known [91]. A few works currently exist in the field of static applications of damage mechanics [92, 93]. The work of Sampaio et al. [94], addressed damage behaviour of an adhesive joint by an analytical damage mechanics model accounting for the value of t_A. The authors observed that comparing the predicted values of failure stress against experimental data for different values of t_A, a good agreement was found. Hua et al. [95] proposed a mesh-independent damage mechanics model to predict the residual strength of adhesively bonded joints with the ductile adhesive Hysol® EA9321 under different scenarios of environmental degradation. The study was performed by introducing a displacement-based damage parameter into the constitutive equation of damage materials, which allowed to establish a linear response of the material behaviour. The mesh independency derived from a damage parameter that is defined in terms of the equivalent plastic displacement rather than strain. The study concluded that the joint strength predictions and the respective damage initiation and propagation during loading matched well with the experimental data. This technique was considered as useful to predict the environmental degradation, the failure path and the actual degree of damage in ductile bonded joints, were failure is predominantly within the adhesive bond.

2.2.2.5 Extended finite element method

The recently developed eXtended Finite Element Method (XFEM) is an extension of the FE method and its fundamental features were firstly presented in the late 1990s by Belytschko and Black [96]. This method, contrary to CZM, does not requires the crack to follow a predefined path. XFEM simulates crack onset and growth along an arbitrary path without the requirement of the mesh to match the geometry of the discontinuities neither remeshing near the crack [97]. It is based on concept of partition of unit, which consists on the introduction of local enrichment functions for the nodal displacements to model crack growth and separation between crack faces [98]. As the crack tip grows, it continuously changes its position and orientation due to loading conditions, and the XFEM algorithm creates the necessary enrichment functions for the nodal points of the FE around the crack path/tip. XFEM uses damage laws based on the bulk strength of the materials for the initiation of damage and strain for the assessment of failure (defined by G_{IC}), rather than values of t_n^0/t_s^0 or δ_n^0/δ_s^0 used in CZM. Therefore, damage and failure are simulated by suitable damage initiation criteria (MAXPS and MAXPE) and damage laws (traction-separation laws that simulate material degradation up to failure) between the real and phantom nodes of a cracked element. In the presence of damage propagation, phantom nodes are established that subdivide elements cut by a crack and simulate separation between the newly created sub elements. Initially, phantom nodes

have the same coordinates than the real nodes and are completely constrained to the real nodes up to damage initiation.

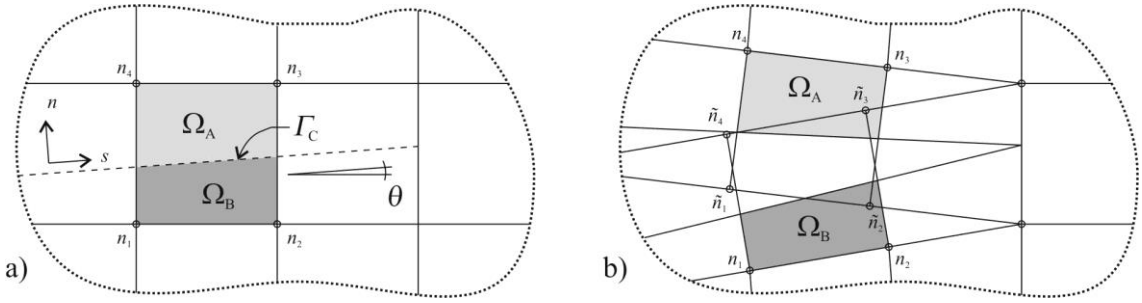

Figure 39 – Damage propagation using the phantom nodes concept: before (a) and after partitioning (b) of a cracked element into sub-elements [99]

In Figure 39, the highlighted element has nodes n_1-n_4. After being crossed by a crack, the element is divided in two sub-elements. The discontinuity in the displacements is made possible by adding phantom nodes ($\tilde{n}_1$-$\tilde{n}_4$) superimposed to the original nodes. When an element cracks, each one of the two sub-elements will be formed by real nodes (the ones corresponding to the cracked part) and phantom nodes (the ones that no longer belong to the respective part of the original element). These two elements that have fully independent displacement fields replace the original one. From this point, each pair of real/phantom node of the cracked element is allowed to separate according to a suitable cohesive law up to failure. If initiation criteria are based on principal stresses or strains, crack initiation/propagation will always take place orthogonally to the maximum principal stresses or strains.

Several applications to this innovative technique were proposed to simulate different engineering problems. In 2000, three-dimensional damage simulations [100] and modelling cracks with multiple branches, multiple holes and cracks emanating from holes [101] were made available. In 2002, Moës and Belytschko [102] solved the problem of cohesive propagation of cracks in concrete structures considering three-point bending and four point shear scaled specimens. The use of plastic enrichments in XFEM modelling to capture the singular fields in elasto-plastic fracture mechanics was proposed by Elguedj et al. [103]. Campilho et al. [58] predicted the strength of single and double lap joints made of aluminium adherends and bonded with a brittle adhesive (Araldite® AV138) by standard FEM and XFEM. It was shown that, due to the direction of crack growth being ruled by the maximum principal stresses/strains at the crack tip, the damage grows towards and within the adherends, which is not consistent with the real behaviour of the joints. However, the XFEM was used with satisfactory results to predict failure by approximating it to damage onset at the overlap edges. However, results were mesh dependent.

THESIS DEVELOPMENT

3 THESIS DEVELOPMENT

3.1 Experimental work

This section addresses the experimental part of the thesis, where all material properties, joint geometry, manufacturing process, results and comments are presented. The experimental work described in this thesis was previously executed by de Sousa [6] (joints with the adhesives Araldite® AV138 and Araldite® 2015) and by Carvalho [7] (joints with the adhesive Sikaforce® 7752). The work carried out in this section consisted of the raw data analysis from the tests and respective treatment and analysis for subsequent comparison with the numerical results.

3.1.1 Materials

The next subsections concern the materials used to perform the experimental work, and their most relevant mechanical properties useful for the experimental and numerical analyses.

3.1.1.1 Adherends

The material used as adherend in all joints was the high strength and ductile aluminium alloy AW6082-T651. This alloy is obtained through artificial ageing at 180°C [104], and it was selected not only because of its good mechanical properties, but also due to the vast structural applications under different extruded or rolled shapes. This aluminium alloy was characterized in the work of Campilho et al. [58], where the most relevant mechanical properties presented in Table 2 were defined.

Table 2 - Relevant mechanical properties of the aluminium alloy AW6082-T651 [58]

Properties	Aluminium 6082-T651
Tensile failure stress, σ_f [MPa]	324.00±0.16
Young´s modulus, E [GPa]	70.07±0.83
Tensile yield stress, σ_y [MPa]	261.67±7.65
Tensile Failure strain, ε_f [%]	21.70±4.24
Poisson´s ratio, ν	0.3*

* Manufacturer´s value

The aluminium σ-ε curves presented in Figure 40 were experimentally obtained according to the ASTM-E8M-04 standard [58]. The numerical approximation used in the numerical simulations is also represented.

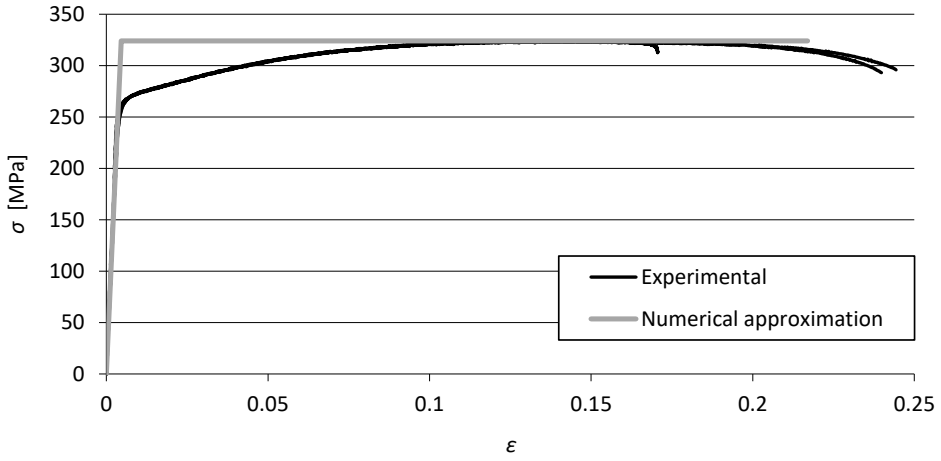

Figure 40 – Aluminium σ-ε curves and numerical approximation [58]

3.1.1.2 Adhesives

The three adhesives tested were all two part (resin + hardener), two epoxy (Araldite® AV138 and Araldite® 2015) and one polyurethane (Sikaforce® 7752). They all present a low viscosity, which promotes an easier application on the adherends.

3.1.1.2.1 Araldite® AV138

The structural epoxy adhesive Araldite® AV138 is manufactured by HUNTSMAN ADVANCED MATERIALS. It has a brittle behaviour but high strength (Figure 41, Table 3), and it is suitable to join miscellaneous materials like metals, composites, polymers [77].

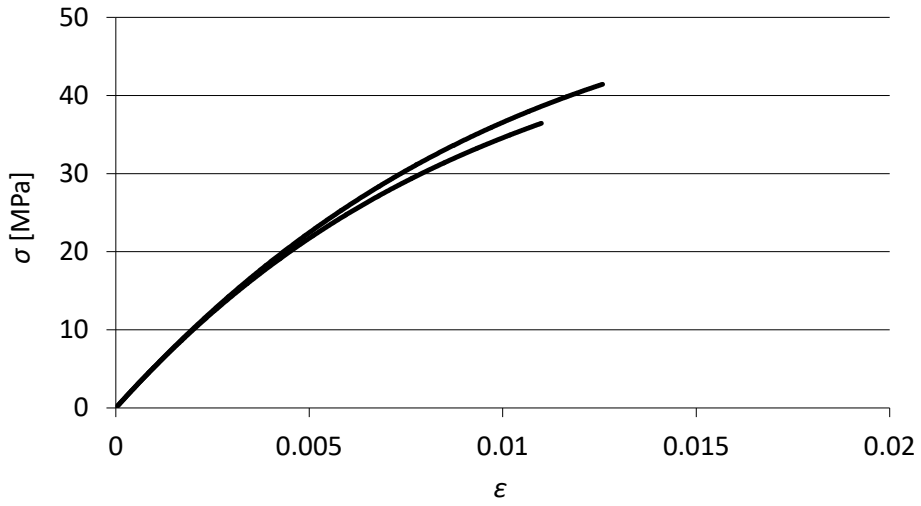

Figure 41 –σ-ε curves estimated by the bulk specimens of the Adhesive Araldite® AV138 [58]

This adhesive is provided in two recipients (Figure 42), one with a thermoset resin AV138 and other with the hardener HV998, and the mixture is performed manually after weighting in the correct proportion. The mixture proportion is 100 g of resin for 40 grams of hardener, with an accuracy of ±5%. This adhesive is a thixotropic gap filling paste with low out gassing and volatile loss, and it cures at temperatures down to 5°C.

Figure 42 - Adhesive Araldite® AV138 [6]

Table 3 – Properties of the Araldite® AV138 [5]

Properties	Araldite® AV138
Young´s modulus, E [GPa]	4.89±0.81
Poisson´s ratio, ν	0.35*
Tensile yield stress, σ_y [MPa]	36.49±2.47
Tensile failure stress, σ_f [MPa]	39.45±3.18
Tensile failure strain, ε_f [%]	1.21±0.10
Shear modulus, G [GPa]	1.56±0.01
Shear yield strength, τ_y [MPa]	25.10±0.33
Shear failure strength, τ_f [MPa]	30.20±0.40
Shear failure strain, γ_f [%]	7.80±0.70
Toughness in tension, G_{Ic} [N/mm]	0.20**
Toughness in shear G_{IIc} [N/mm]	0.38**

* - Manufacturer´s value

** - Estimated in reference [58].

3.1.1.2.2 Araldite® 2015

The adhesive Araldite® 2015 is also manufactured by HUNTSMAN ADVANCED MATERIALS, and it is equally a two part structural epoxy adhesive. It shows a smaller ultimate strength than the previous adhesive and has intermediate ductility, allowing large plastic flow prior to failure. A redistribution of stresses occurs at stress

concentrated regions which usually take place in the edges of the overlap ends of bonded joints. Figure 43 shows the cartridges incorporating mixers for application of the adhesive.

Figure 43 – Adhesive Araldite® 2015 [6]

The bond strength and durability of joints with this adhesive are dependent on an adequate surface treatment. At least, surfaces to be bonded should be clean with solvent wiping (acetone). However, surface preparation may also include a combination of mechanical abrading, chemical cleaning and acid etching [11].

The analysis of Figure 44 and Table 4, which present the σ-ε curves and mechanical properties, respectively, shows that the shear failure strain is six times higher than that of the previous adhesive. However, the tensile and shear failure strength of the Araldite® AV138 is twice the value of the Araldite® 2015. Thus, this ductile adhesive allow stress distribution at the stress concentration area, typically at the edges of the overlap due to joint asymmetry and to the adherends' differential deformation [61].

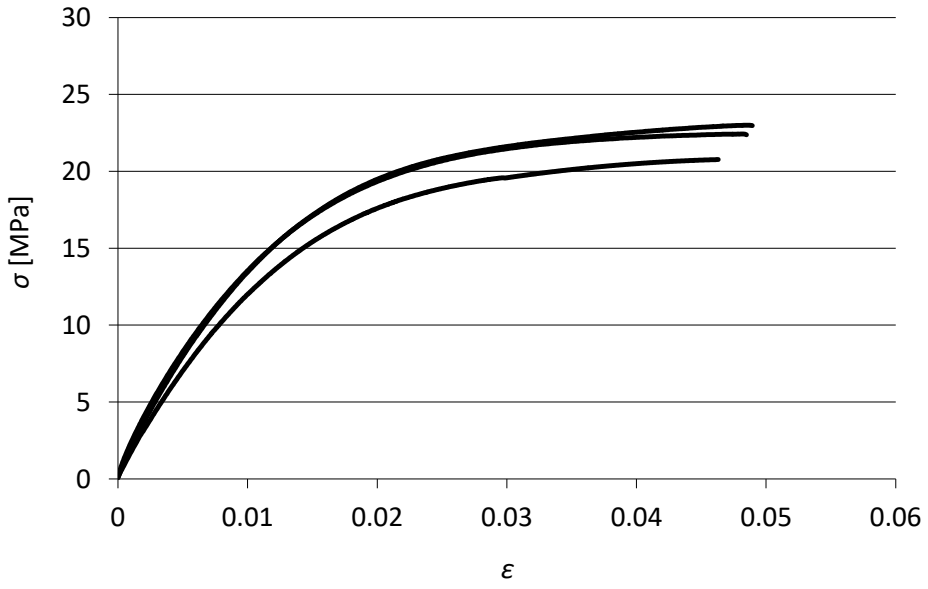

Figure 44 – σ-ε curves estimated by the bulk specimens of the Araldite® 2015 [9]

Table 4 - Properties of the Araldite® 2015 [9]

Properties	Araldite® 2015
Young´s modulus, E [GPa]	1.85±0.21
Poisson´s ratio, ν	0.33*
Tensile yield strength, σ_y [MPa]	12.63±0.61
Tensile failure strength, σ_f [MPa]	21.63±1.61
Tensile failure strain, ε_f [%]	4.77±0.15
Shear modulus, G [GPa]	0.56±0.21
Shear yield strength, τ_y [MPa]	14.60±1.3
Shear failure strength, τ_f [MPa]	17.9±1.8
Shear failure strain, γ_f [%]	43.9±3.4
Toughness in tension, G_{Ic} [N/mm]	0.43±0.02
Toughness in shear G_{IIc} [N/mm]	4.70±0.34

* - Manufacturer´s value

3.1.1.2.3 Sikaforce® 7752

The structural polyurethane adhesive Sikaforce® 7752 is manufactured by Sika® and it is provided in two parts (Figure 45). The mixing proportion is 100 g of resin for 20 g of hardener.

Figure 45 - Adhesive Sikaforce® 7752 [7]

It is the most ductile of the three adhesives, as depicted in the σ-ε curves of Figure 46. Analysing the mechanical properties presented in Table 5, the adhesive Sikaforce® 7752 has the lowest tensile and shear tensile strength. However, it has high ductility, which allows large plastic flow prior to failure, resulting in a higher joint strength [105].

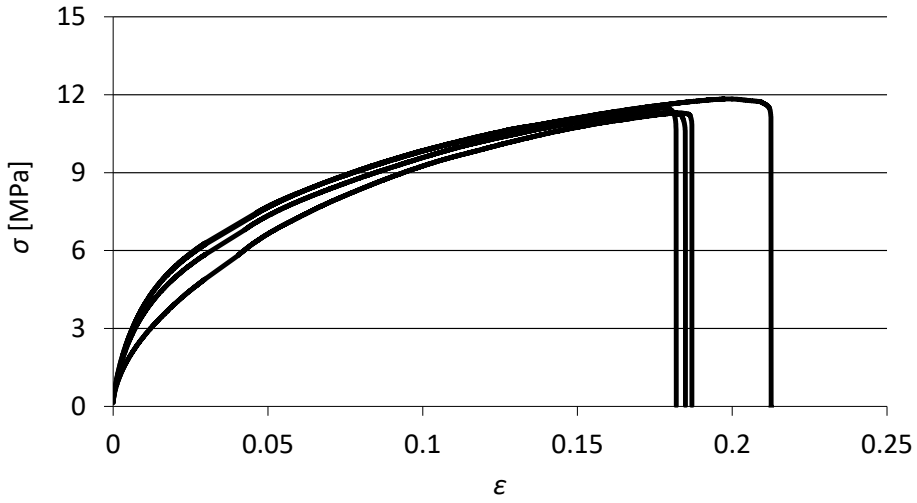

Figure 46 - σ-ε curves estimated by the bulk specimens of the Sikaforce® 7752 [105]

Table 5 - Properties of the Sikaforce® 7752 [105]

Properties	Sikaforce® 7752
Young´s modulus, E [GPa]	0.49±0.09
Poisson´s ratio, ν	0.30*
Tensile yield strength, σ_y [MPa]	3.24±0.48
Tensile failure strength, σ_f [MPa]	11.48±0.25
Tensile failure strain, ε_f [%]	19.18±1.40
Shear modulus, G [GPa]	0.19±0.01
Shear yield strength, τ_y [MPa]	5.16±1.14
Shear failure strength, τ_f [MPa]	10.17±0.64
Shear failure strain, γ_f [%]	54.82±6.38
Toughness in tension, G_{Ic} [N/mm]	2.36±0.17
Toughness in shear G_{IIc} [N/mm]	5.41±0.47

* - Manufacturer´s value

3.1.2 Joint geometry

The SLJ geometry and characteristic dimensions are presented in Figure 47 and Table 6. All the specimens have the same geometric configuration varying only the L_O.

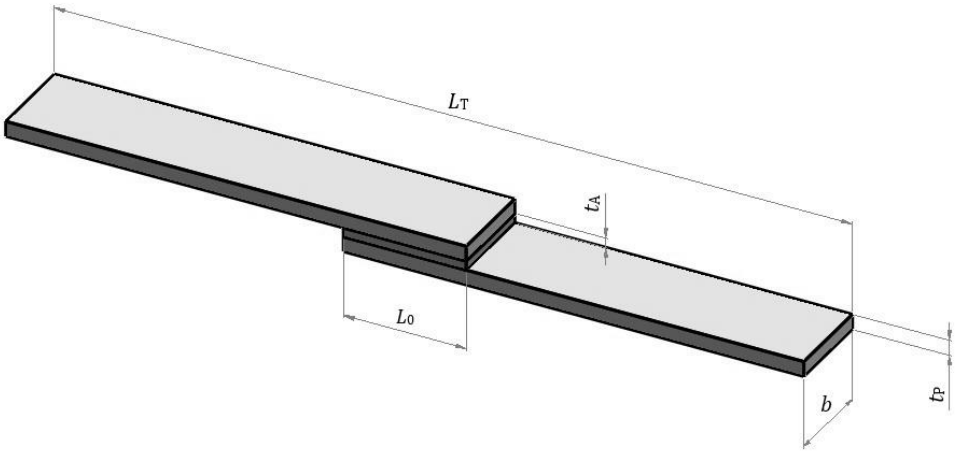

Figure 47 – Specimen geometry configuration

Table 6 - Specimen dimensions (mm)

L_O	12.5	25	37.5	50
Length between grips (L_T)	170	170	170	170
Adherend thickness (t_P)	3	3	3	3
Adhesive thickness (t_A)	0.2	0.2	0.2	0.2
Specimen width (b)	25	25	25	25

3.1.3 Adhesive joint fabrication

The adherends were already provided in their final dimensions. Sixty adherends were necessary to obtain 5 specimens per joint configuration. The first step (Figure 48) consists of roughening, by manual abrasion, the surfaces to bond and cleaning it with acetone to provide oxide removal and improve the bonding process.

a) b)

Figure 48 - Surface preparation (a) and acetone cleaning (b) [6]

The surface preparation removed from the adherends' surface foreign materials such as dirt, oil, moisture and weak oxide layers. Otherwise, the adhesive will bond to these weak boundary layers rather than the adherend.

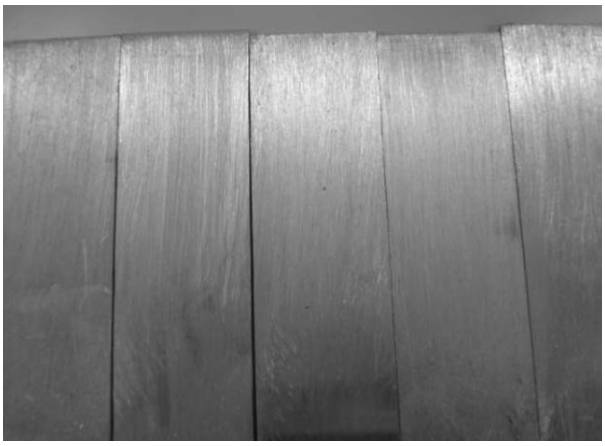

Figure 49 – Adherends' appearance after surface cleaning [6]

The next step consisted of the preparation to apply the adhesive and assemble the joints. With this purpose, the adherends were fixed in an apparatus for the correct alignment (Figure 50), using a calibrated fishing line with 0.2 mm placed under the upper adherend to ensure a constant adhesive thickness (t_A), as presented in Figure 51.

Figure 50 – Adherends' fixing and alignment [6]

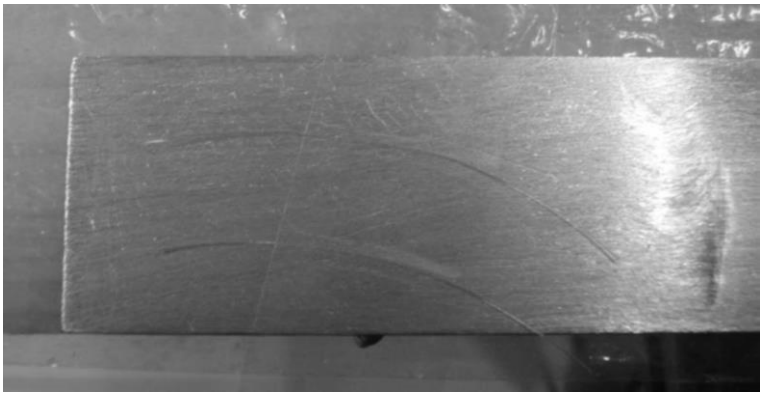

Figure 51 - Adherend with calibrated fishing line [6]

Following, the adhesive was applied on the bonding surfaces. The curing process was accomplished using pressure grips to guarantee the adherends' alignment (Figure 52). Tabs were glued at the specimens' edges to ensure a correct alignment in the testing machine.

Figure 52 - Grip fixing [6]

The joints were left to cure at room temperature for one week to assure complete curing. To provide square edges at the overlap region, the excess adhesive was removed using a grindstone in a vertical drill (Figure 53). This is important because the adhesive excess influences the joint strength, which theoretically and in numerical models does not exist.

Figure 53 - Adhesive excess removal [7]

3.1.4 Experimental testing

In order to perform the experimental tests, a Shimadzu® AG-X 100 (Figure 54) testing machine with a 100 kN load cell was used, considering a distance between grips of 170 mm and room temperature. The displacement rate was 1 mm/min.

a) b)

Figure 54 - Shimadzu testing machine (a) and adherend fixation (b) [6]

3.1.5 Results

In this section the *P-δ* curves obtained from the experimental tests, the failure modes and the P_m are presented. A brief analysis of the joint strength is discussed regarding the three adhesives.

3.1.5.1 P-δ curves

The experimental results of few joints were markedly different from the average behaviour and, therefore, those results were excluded from the analysis. Figure 55 presents the *P-δ* curves of the joints bonded with the adhesive Araldite® AV138. All curves have a linear behaviour up to failure, although some initial fluctuations of the elastic stiffness and displacement at P_m variation occurred due to the machine and grips flexibility. However, a good reproducibility was observed regarding the stiffness and P_m.

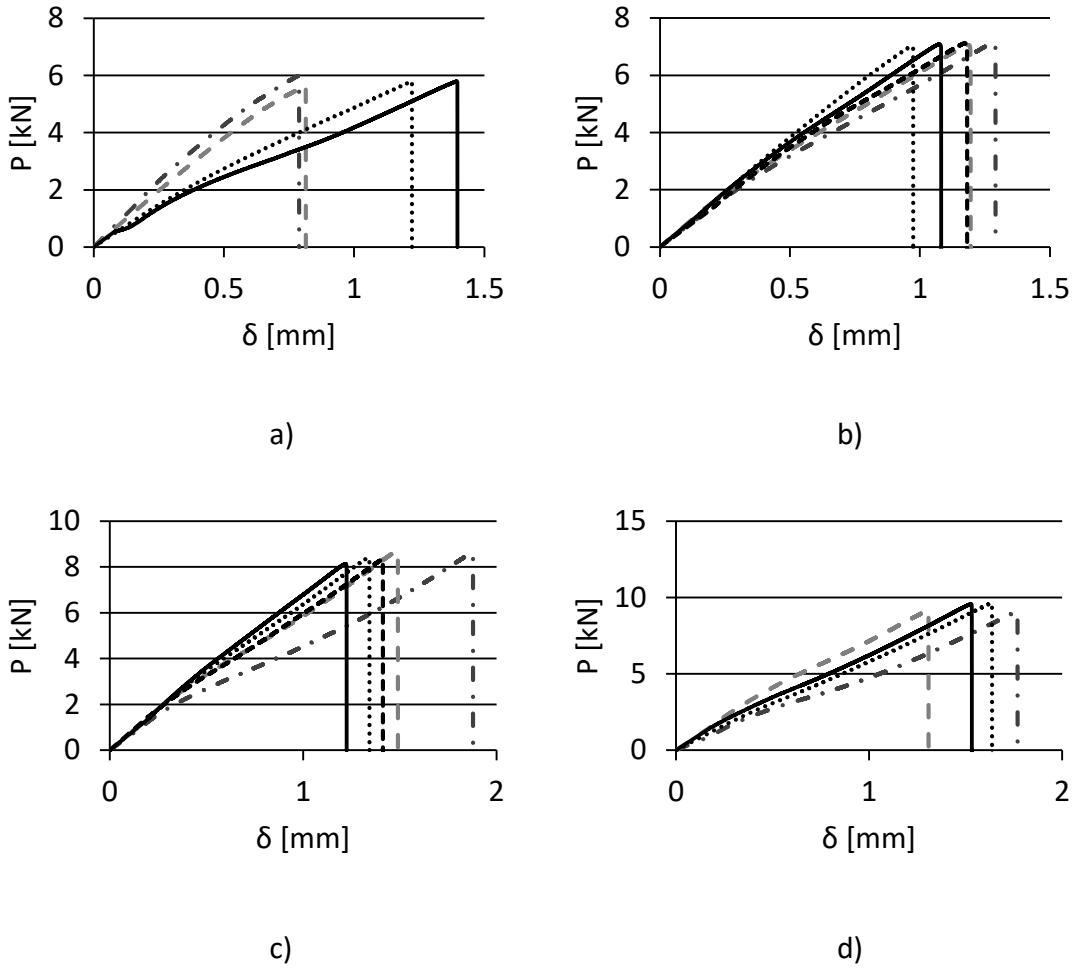

Figure 55 - *P-δ* curves for the joints bonded with the Araldite® AV138 and L_O=12.5 (a), 25 (b), 37.5 (c) and 50 mm (d)

The following tables (Table 7, Table 8 and Table 9) show the average P_m for each adhesive and L_O, respective standard deviation, and the percentile P_m increase between a joint with a given L_O and the previous one.

Table 7 - P_m and deviation for the joints bonded with the Araldite® AV138

L_O (mm)	12.5	25	37.5	50
P_m average (N)	5793.17	7079.09	8417.08	9342.21
Standard deviation	149.69	51.04	214.22	278.45
P_m increase (%)	-	22.20	18.90	10.99

Table 7 shows that P_m increases with L_O, but not steadily, since the P_m improvement is not too significant between L_O=25 and 50 mm. P_m overall increases by only 61.26% from L_O=12.5 to 50 mm. due to the brittleness of the adhesive. This characteristic does not permit the adhesive's plastification and, therefore, failure occurs when the tensile peak is reached [58].

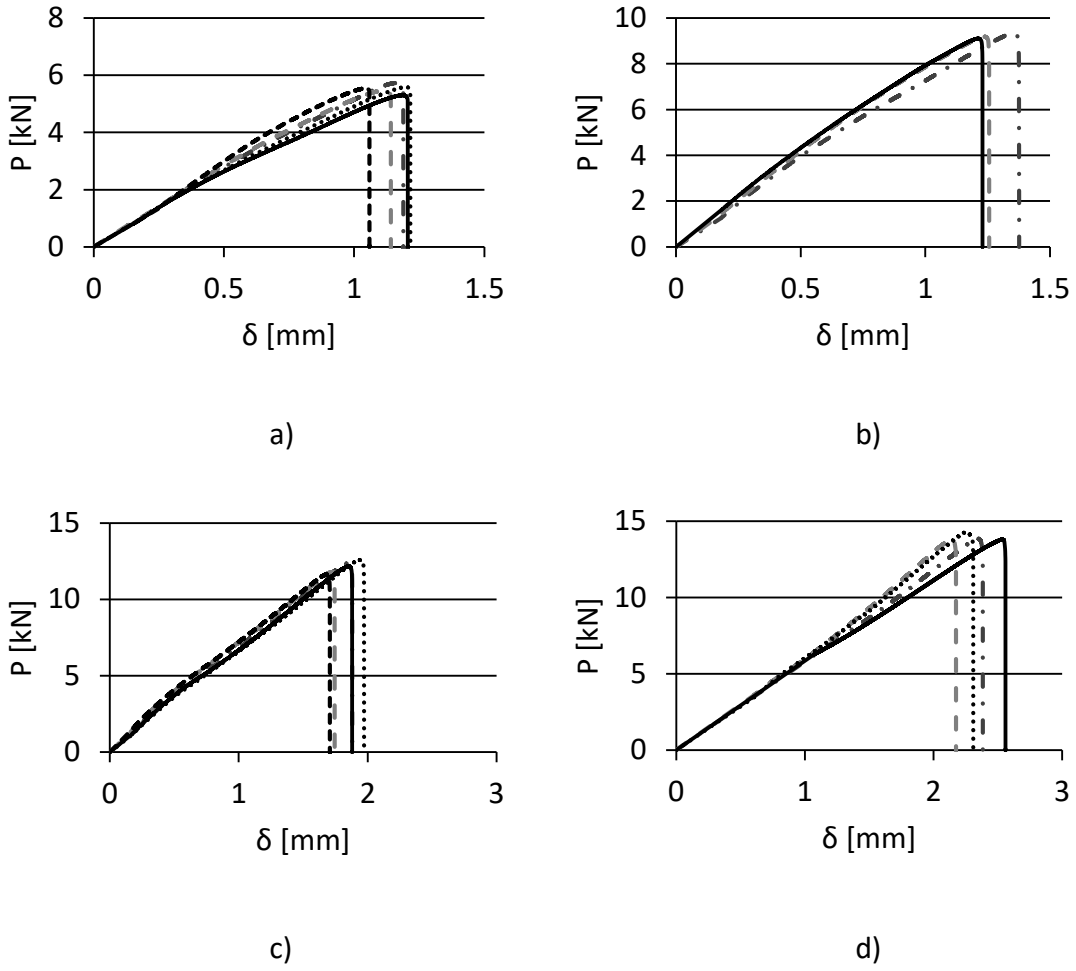

Figure 56 - *P-δ* curves for the joints bonded with the Araldite® 2015 and L_O=12.5 (a), 25 (b), 37.5 (c) and 50 mm (d)

The *P-δ* curves of the adhesive Araldite® 2015 depicted in Figure 56 present a linear behaviour up to failure, as the previous adhesive, but with smaller fluctuations on the displacement at P_m. There is also a good reproducibility regarding P_m.

Table 8 - P_m and deviation for the joints bonded with the adhesive Araldite® 2015

L_O (mm)	12.5	25	37.5	50
P_m average (N)	5520.52	9207.69	12116.79	13927.85
Standard deviation	154.83	120.71	398.53	229.92
P_m increase (%)	-	66.79	31.59	14.94

Regarding Table 8 for the adhesive Araldite® 2015, P_m substantially increases with L_O. The overall increase is 152.29% from L_O=12.5 to 50 mm. The reason of such difference between this and the previous adhesive is the plasticity that the Araldite® 2015 possesses, enabling stress redistribution before P_m is reached [58].

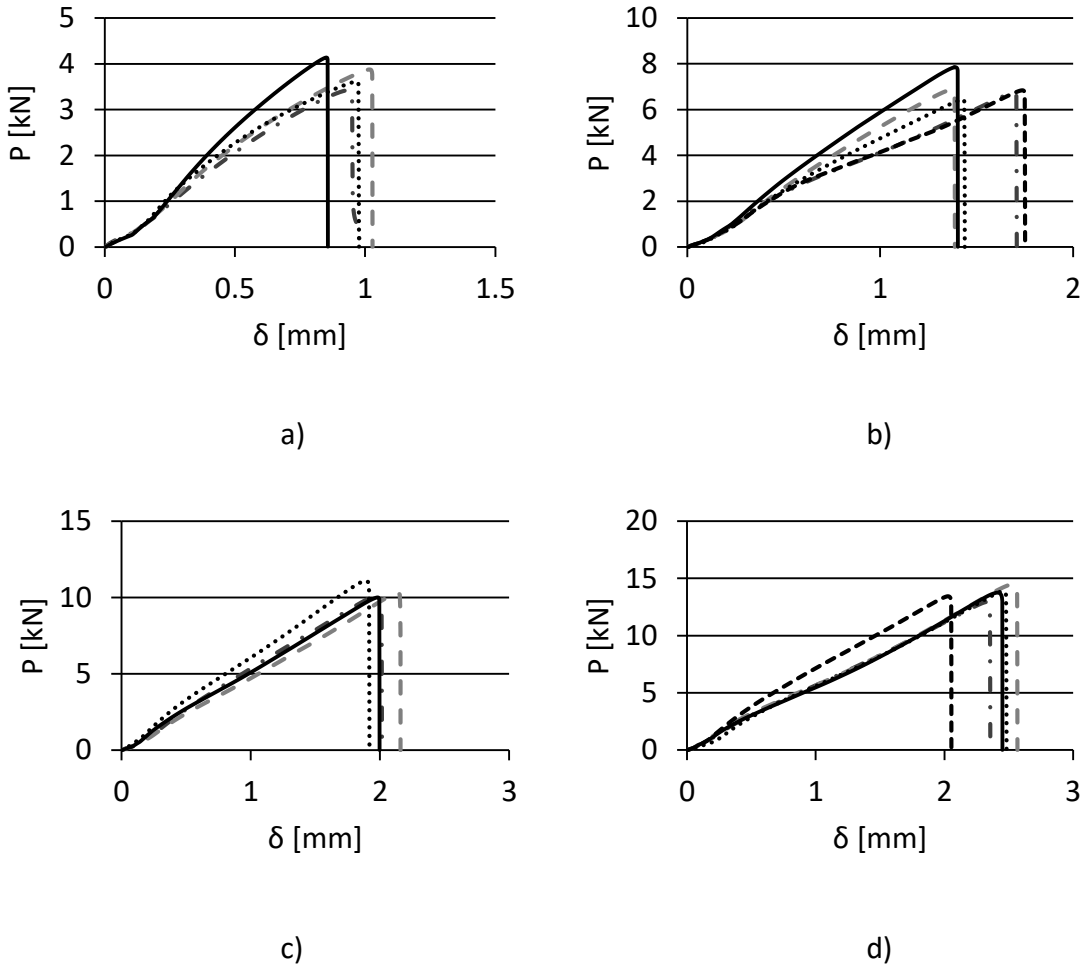

Figure 57 - *P-δ* curves for the joints bonded with the Sikaforce® 7752 and L_O=12.5 (a), 25 (b), 37.5 (c) and 50 mm (d)

Figure 57 shows the *P-δ* curves of the adhesive Sikaforce® 7752, which present a nonlinear behaviour before reaching P_m, due to the high adhesive´s plasticity. Deviations on the plastic stiffness in the beginning of experimentation can be observed. However, the plots present good reproducibility regarding the stiffness and P_m.

Table 9 - P_m and deviation for the joints bonded with the adhesive Sikaforce® 7752

L_O (mm)	12.5	25	37.5	50
P_m average (N)	3763.48	6940.57	10371.10	13698.89
Standard deviation	311.25	535.52	490.64	567.62
P_m increase (%)	-	84.41	49.43	32.08

The P_m evolution with L_O is the highest of the three adhesives (Table 9). This is due to the fact that the Sikaforce® 7752 is the most ductile of all three adhesives, which results in failure under global yielding conditions [15]. The overall P_m increase is 263.99% from L_O=12.5 to 50 mm.

3.1.5.2 Failure modes

The use of different adhesives and values of L_O may induce different failure modes. The failure modes of all joint configurations are presented in this subsection.

The failure modes of the specimens bonded with the adhesive Araldite® AV138 are presented in Figure 58 (a typical failure for each value of L_O is considered). All failures with this adhesive were cohesive in the adhesive layer. The apparent lack of adhesive at the bonded area is due to failure taking place nearby the interface between the adhesive layer and the adherend.

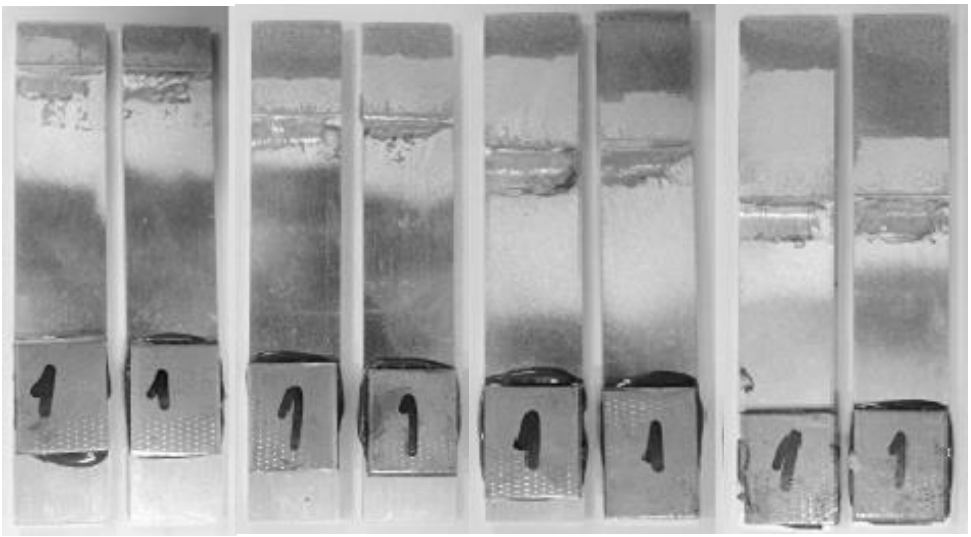

a) b) c) d)

Figure 58 - Failure modes of the specimens bonded with the adhesive Araldite ® AV138, and L_O=12.5 (a), 25 (b), 37.5 (c) and 50 mm (d)

The failure modes of the specimens bonded with the adhesive Araldite® 2015 are presented in Figure 59. A cohesive failure is observed for all specimens at the adhesive mid-thickness. This failure mode denotes an efficient bonding between the adherends and adhesive.

Figure 60 shows the failure modes of the specimens bonded with the adhesive Sikaforce® 7752. The failures are apparently adhesive; however, with careful inspection, adhesive can be found in both adherends, thus corresponding to a cohesive failure.

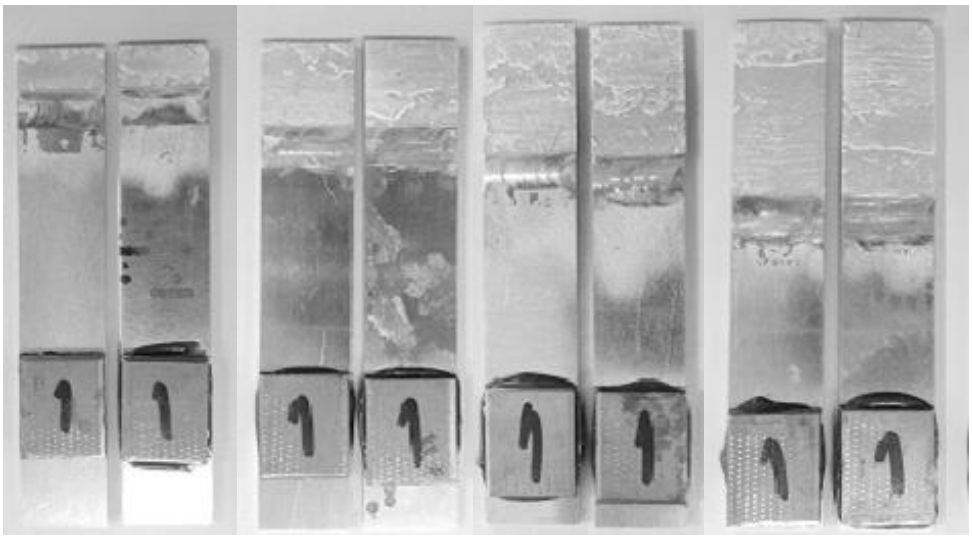

a) b) c) d)

Figure 59 - Failure modes of the specimens bonded with the adhesive Araldite ® 2015, and LO=12.5 (a), 25 (b), 37.5 (c) and 50 mm (d)

a) b) c) d)

Figure 60 - Failure modes of the specimens bonded with the adhesive Sikaforce® 7752, and L_O=12.5 (a), 25 (b), 37.5 (c) and 50 mm (d)

3.1.5.3 Joint strength

The average values of P_m and respective deviation for the joints bonded with the three adhesives are depicted in Figure 61. The evolution of P_m with L_O is almost lineal for all joints.

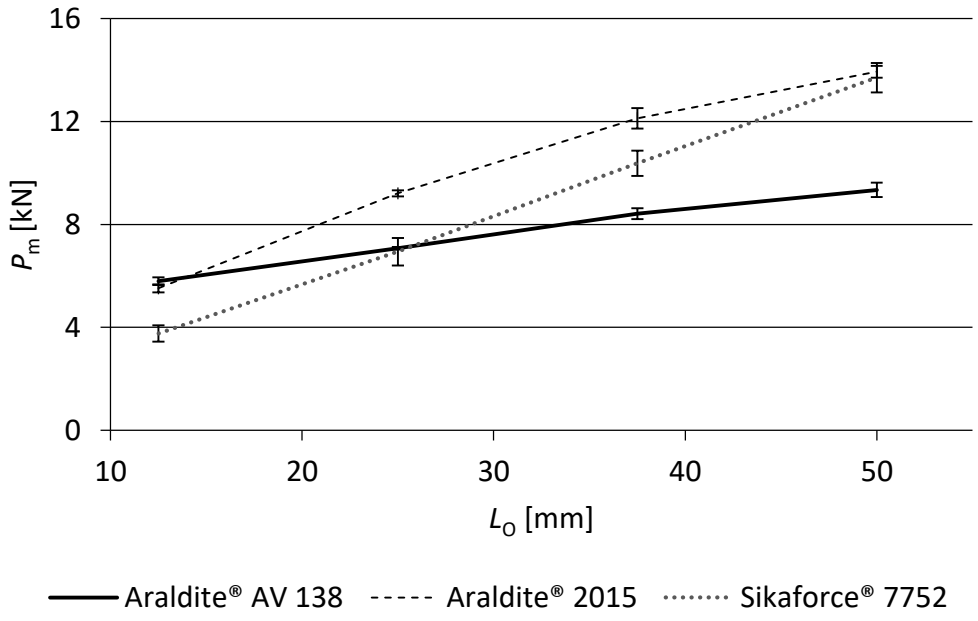

Figure 61 – Average values of P_m and standard deviation for each value of L_O and adhesive type

The increase of P_m with L_O for the adhesive Araldite® AV138 is not very significant, contrarily to the others adhesives. For L_O=12.5 mm, the value of P_m of the Araldite® AV138 and Araldite® 2015 is identical, while the adhesive Sikaforce® 7752 is lower by 35.04%. For L_O=25 mm, the Araldite® 2015 performs best, while the other two adhesives give a P_m value lower by ≈23.87%. For L_O=37.5 mm, the Araldite® 2015 still has the maximum P_m, while the Sikaforce® 7752 is lower by 14.41% and the Araldite® AV138 by 30.53%. For L_O=50 mm, the adhesives Sikaforce® 7752 and Araldite® 2015 perform identical in which regards P_m and the Araldite® AV138 is lower by ≈32.36%. The maximum values of the standard deviation were 2.98% for Araldite® AV138, 3.29% for Araldite® 2015 and 8.27% for Sikaforce® 7752.

A detailed analysis of the obtained results is presented in Section 3.2.4.

3.2 Numerical work

This section addresses the numerical work of this thesis. The imposed numerical conditions and the CZM formulation are initially presented. A stress analysis in the adhesive layer is further performed and discussed, as well as the joints strength

prediction and it´s comparison with the experiments. Finally, a study on the influence of different conditions in the numerical analysis is performed.

3.2.1 Numerical conditions

For a better understanding of the joints' behaviour, a stress analysis in the adhesive layer was carried out prior to the strength prediction. The software ABAQUS® was used to accomplish those analysis. The software is based on the FEM and has an embedded CZM modelling package. For the stress analysis, the adherends and adhesive were modelled as elastic-plastic isotropic materials (Figure 62), and by 4-node plane-strain elements (CPE4 from ABAQUS®).

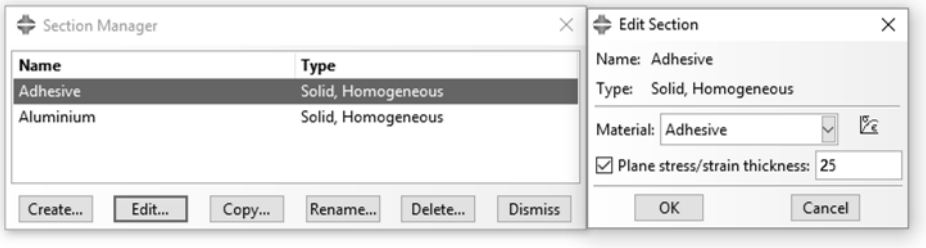

Figure 62 - ABAQUS® section manager used in the stress analysis

For the strength prediction, the adherends were modelled as for the stress analysis and the adhesives were modelled by 4-node cohesive elements (Figure 63). Both simulations consisted of a 2D and geometrically non-linear analysis.

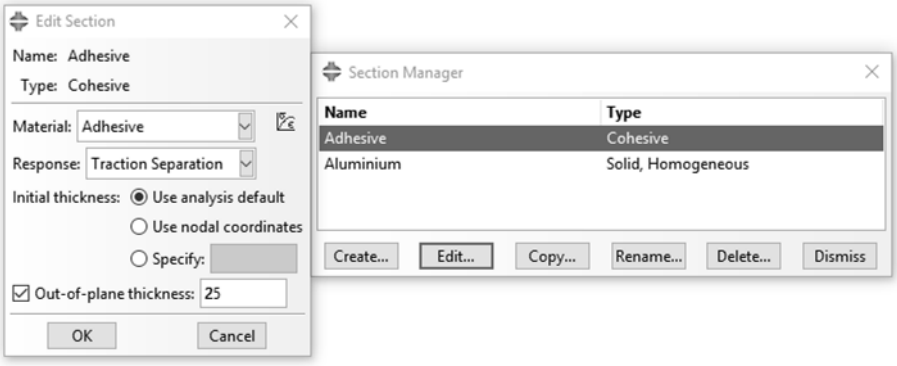

Figure 63 - ABAQUS® section manager used in the strength prediction

Meshes for the stress analysis require a higher degree of refinement than the mesh used in the strength prediction (Figure 64) in order to accurately measure the stress variation along the joint, especially at the overlap edges because, in those regions, there are theoretical singularity spots with large stress variations [61].

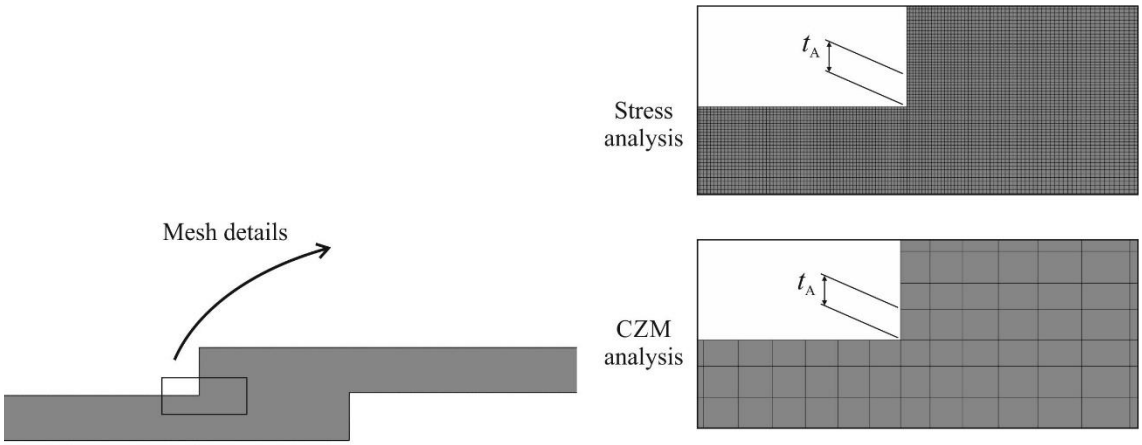

Figure 64 – Example of FE mesh for L_O=12.5 mm, including mesh details for the stress and strength analyses

To provide identical modelling conditions, the element sizes were made equal at overlap edges for all L_O values (approximately 0.02×0.02 mm^2 elements for the stress analysis and 0.2×0.2 mm^2 elements for the strength analysis). In order to reduce the computer effort, mesh grading was considered by using the bias effect. The bias effect can be regarded as the growing refinement along a model edge. In the adhesive layer length, a double bias effect was considered from the central region to the overlap edges, as presented in Figure 65. In both stress and strength analyses, a higher refinement was applied horizontally in the direction of the overlap edges and in the adherends towards the adhesive layer, to capture the stress variations at these locations.

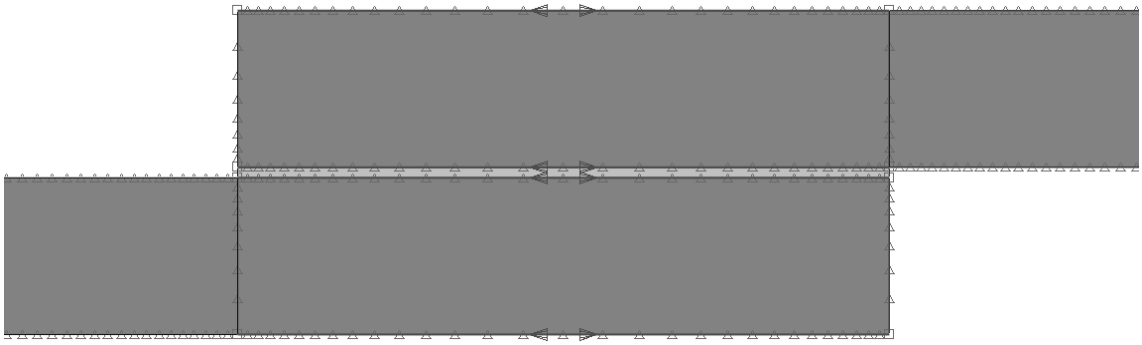

Figure 65 - Double bias effect in the adhesive layer length

In adherends' height, bias effects were considered as well towards adhesive layer (Figure 66).

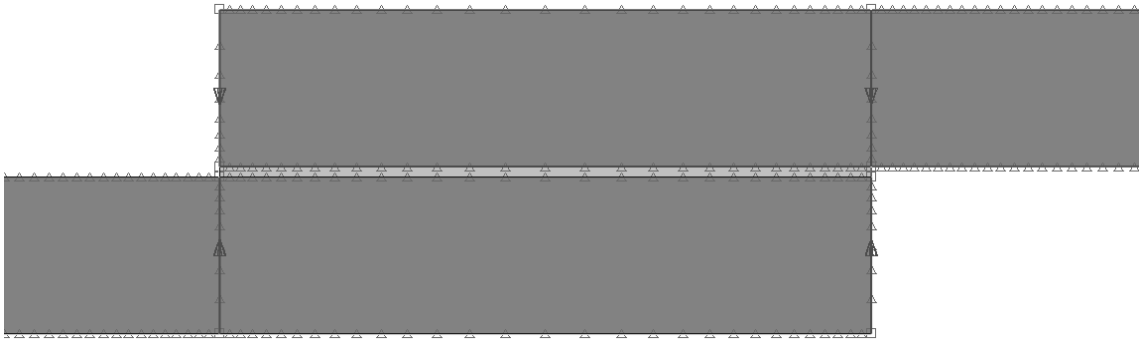

Figure 66 - Bias effect in the adherends in the vertical direction

In the unbonded adherends' length, bias effects were used towards overlap region (Figure 67).

Figure 67 - Bias effect in the adherends at the unbonded region

The different mesh elements for all values of L_O are presented in Table 10 and Table 11, for the stress and strength analyses, respectively.

Table 10 – Mesh refinement for the stress analysis

	L_O (mm)	12.5	25	37.5	50
Figure 65	Number of elements	300	500	800	1100
	Bias ratio	4	4	4	4
Figure 66	Number of elements	80	80	80	80
	Bias ratio	4	4	4	4
Figure 67	Number of elements	1000	1000	1000	1000
	Bias ratio	10	10	10	4

Table 11 – Mesh refinement for the strength analysis

	L_O (mm)	12.5	25	37.5	50
Figure 65	Number of elements	30	60	90	120
	Bias ratio	4	4	4	4
Figure 66	Number of elements	8	8	8	8
	Bias ratio	4	4	4	4
Figure 67	Number of elements	100	90	80	70
	Bias ratio	10	10	10	10

The applied boundary conditions consisted of clamping the joints at one of the edges, to reproduce the testing machine gripping, while the opposite edge was pulled in tension together with lateral restraining, as presented in Figure 68.

Figure 68 – Boundary conditions

3.2.2 Cohesive zone models

3.2.2.1 Mixed-mode triangular CZM

CZM model the elastic loading, initiation of damage and further propagation due to local failure within a material. CZM are based on a relationship between stresses and relative displacements connecting initially superimposed nodes of the cohesive elements (Figure 20), to simulate the elastic behaviour up to a peak load and subsequent softening, to model the gradual degradation of material properties up to complete failure. Generically speaking, the shape of the softening laws can be adjusted to conform to the behaviour of the material or interface they are simulating [49, 55]. The areas under the traction-separation laws in each mode of loading (tension and shear) are equalled to the respective fracture energy. Under pure mode, damage propagation occurs at a specific integration point when the stresses are released in the respective traction-separation law. Under mixed-mode, energetic criteria are often used to combine tension and shear [49], thus simulating the typical mixed mode behaviour inherent to bonded assemblies. In this work, a continuum-based approach, i.e. using the cohesive elements to model solids rather interfaces, was considered to model the finite thickness of the adhesive layer. The cohesive layer is assumed to be under one direct component of strain (through-thickness) and one transverse shear strain, which are computed directly from the element kinematics. The membrane strains are assumed as zero, which is appropriate for thin and compliant layers between stiff adherends. The strength predictions of CZM modelling are expected to be mesh independent [58].

The traction-separation law assumes an initial linear elastic behaviour followed by linear evolution of damage. Elasticity is defined by an elastic constitutive matrix relating stresses and strains across the interface [47]

$$\mathbf{t} = \begin{Bmatrix} t_n \\ t_s \end{Bmatrix} = \begin{bmatrix} K_{nn} & K_{ns} \\ K_{ns} & K_{ss} \end{bmatrix} . \begin{Bmatrix} \varepsilon_n \\ \varepsilon_s \end{Bmatrix} = \mathbf{K\varepsilon}. \tag{11}$$

The matrix **K** contains the stiffness parameters of the adhesive layer, given by the relevant elastic moduli. A suitable approximation for thin adhesive layers is provided

with K_{nn}= E, K_{ss}= G, K_{ns}=0; E and G are the longitudinal and transverse elastic moduli [49]. Damage initiation can be specified by different criteria. In this work, the QUADS criterion was considered for the initiation of damage(equation (4)), already shown to give accurate results [64]. After the peak value in Figure 20 is attained, the material stiffness is degraded under different possible laws, depending on the material to be simulated. For brittle materials such as the Araldite® AV 138, a linear softening law is sufficiently appropriate, Figure 20 [106]. Complete separation is predicted by a linear power law form of the required energies for failure in the pure modes as presented in equation(9) , with α=1.

3.2.2.2 Pure-mode triangular, trapezoidal and linear-exponential CZM

This section describes the mode-uncoupled CZM models with different law shapes tested in this work. The triangular, linear-exponential and trapezoidal shapes were evaluated (Figure 21 schematically represents these three CZM shapes with the associated nomenclature).

As shown in Figure 21, the linear-exponential law is linear up to t_n^0 or t_s^0, and afterwards undergoes an exponential softening up to failure. This shape is an approximation of the full-exponential law [53] providing in this case a more abrupt stress drop than the triangular law, after the peak loads are achieved. G_I and G_{II} are the areas under the CZM laws in tension or shear, respectively. The definition of the normal or shear maximum relative displacements (δ_n^f and δ_s^f, respectively) is carried out by making G_I=G_{IC} for tension or G_{II}=G_{IIC} for shear. The initial linear elastic behaviour in the CZM laws (notwithstanding their shape) is defined by an elastic constitutive matrix relating the current stresses and strains in tension and shear across the interface (subscripts n and s, respectively) [47], as described on equation (11) of the previous subsection.

For all of the three CZM shapes, initiation of damage was evaluated by the QUADS criterion, reported in equation(4). Thus, initiation of damage is coupled between tension and shear [107]. After the criterion of equation(4) is met, the material stiffness initiates a degradation process. However, from this point on, an uncoupled tensile/shear behaviour was used, in which the tensile and shear behaviours of the CZM elements are independent up to failure. This choice was made because of the Abaqus® unavailability of mixed-mode coupling criteria for the trapezoidal CZM formulation.

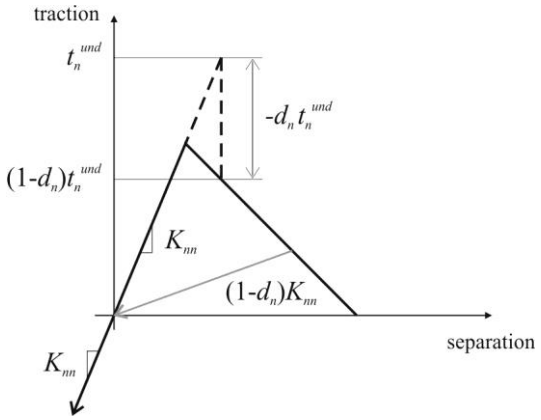

Figure 69 - Definition of the damage variable in tension, d_n, in Abaqus® (extrapolation is possible for d_s)

The softening regions of the CZM laws are defined in Abaqus® by specification of the damage variable (d_n for tension or d_s for shear), as a function of δ_n–δ_n^0 (tension) or δ_s–δ_s^0 (shear), i.e., as a function of the effective displacement beyond damage initiation (δ_n^0 and δ_s^0 represent the damage onset relative displacements in tension and shear, respectively). This is described by the following formulae. Figure 69 pictures the definition of d_n for the triangular law, although it can be extrapolated to d_s [47]

$$\begin{aligned} t_n &= (1-d_n)\, t_n^{und} \\ t_s &= (1-d_s)\, t_s^{und} \end{aligned}, \tag{12}$$

where t_n^{und} and t_s^{und} are the current cohesive tractions in tension and shear, respectively, without stiffness degradation. In this expression, $d_{n,s}$=0 for an undamaged material (in the elastic region) and $d_{n,s}$=1 for a fully damaged material. By this principle, the generic expression (in tension or shear) of $d_{n,s}$ for the triangular law takes the form [47]

$$d_{n,s} = \frac{\delta_{n,s}^{\,f}\left(\delta_{n,s} - \delta_{n,s}^{\,0}\right)}{\delta_{n,s}\left(\delta_{n,s}^{\,f} - \delta_{n,s}^{\,0}\right)}. \tag{13}$$

For the exponential law, the expression of $d_{n,s}$ gives [47]

$$d_{n,s} = 1 - \frac{\delta_{n,s}^{\,0}}{\delta_{n,s}}\left(1 - \frac{1-e^{\left(-\alpha\left(\frac{\delta_{n,s}-\delta_{n,s}^{\,0}}{\delta_{n,s}^{\,f}-\delta_{n,s}^{\,0}}\right)\right)}}{1-e^{(-\alpha)}}\right), \tag{14}$$

where α is a non-dimensional parameter, related to a specific material, that establishes the rate of damage evolution with $\delta_{n,s}$ (for α=0 a triangular law is attained). In this work, α=7 was chosen to provide a significant difference to the triangular shape, by a

significantly faster degradation after $t_{n,s}^0$ is reached. For the trapezoidal law, the stress softening displacements in tension and shear, δ_n^s and δ_s^s, respectively, are introduced. The value of $d_{n,s}$ is divided into the constant stress region ($\delta_{n,s}^0<\delta\leq\delta_{n,s}^s$; Figure 21) and softening region ($\delta_{n,s}^s<\delta\leq\delta_{n,s}^f$; Figure 21) as follows [47]

$$\begin{cases} d_{n,s}=1-\dfrac{\delta_{n,s}^{\ 0}}{\delta_{n,s}} & if \quad \delta_{n,s}^{\ 0}<\delta<\delta_{n,s}^{\ s} \\ d_{n,s}=1-\dfrac{m\delta_{n,s}+b}{K_{nn,ss}\delta_{n,s}} & if \quad \delta_{n,s}^{\ s}<\delta<\delta_{n,s}^{\ f} \end{cases}. \tag{15}$$

The values of m and b relate to the straight line equation of the decaying portion of the CZM law with respect to the t-δ plot origin, given by [47]

$$m=\frac{-t_{n,s}^{\ 0}}{\delta_{n,s}^{\ f}-\delta_{n,s}^{\ s}} \quad ; \quad b=t_{n,s}^{\ 0}-m\delta_{n,s}^{\ s}. \tag{16}$$

The values of $\delta_{n,s}^f$ are found by consideration of the area under the t-δ plot to be equal to $G_{IC,IIC}$. On the other hand, several techniques are available for the definition of $\delta_{n,s}^s$ (trapezoidal law), such as pre-established ratios between $\delta_{n,s}^s$ and $\delta_{n,s}^f$ [74], use of experimental failure strain data [49], or pre-established decaying slope up to $\delta_{n,s}^f$ (e.g. identical slope between the tensile and shear CZM laws, if only tensile data is available) [108]. It this work, the first approach was adopted, considering $\delta_{n,s}^s/\delta_{n,s}^f$=0.8.

3.2.2.3 Cohesive properties estimation

In order to characterize the tensile and shear cohesive laws, the values of t_n^0, t_s^0, G_{IC} and G_{IIC} are required (Figure 21). Studies were published based on the assumption that, by approximation, those parameters were similar to the ones obtained in experimental bulk adhesives [109, 110]. Nevertheless, the restraint to the adhesive layer's strains due to the adherends vicinity in this type of geometry and the crack propagation under mixed-mode origin a difference between bulk and thin layer adhesive properties [73, 111, 112]. Therefore, it becomes necessary to define new methods that provide the adhesive properties adjusted to the geometrical conditions under which they will be employed. The cohesive laws for the Araldite® AV138 were estimated by an inverse method, as presented in the detailed description of Campilho et al. [63]. Due to the non-existence of fracture characterization tests, the tensile and shear strengths obtained by tests with bulk adhesive specimens and thick adherend shear test (TAST) shear test, were used, to estimate t_n^0 e t_s^0, respectively. Those values were used to build an approximate cohesive law, initially using typical G_{IC} and G_{IIC} values for brittle adhesives. The obtained tensile and shear laws were used in the numerical model for one specimen and the adhesive laws were estimated by an adjustment procedure between the

numerical and experimental *P–δ* curves. The obtained G_{IC} and G_{IIC} values were following applied to all joint configurations tested, presenting good results. The *E* and *G* values were experimentally estimated by tensile tests to bulk adhesive specimens and TAST tests, respectively. In another work [58], the authors concluded that the obtained parameters simulate the adhesive behaviour with accuracy. Table 12 presents the Araldite® AV138 cohesive parameters used in a mixed-mode cohesive law.

Table 12 – Tensile and shear cohesive parameters for the adhesive Araldite® AV138

E [MPa]	4890	*G* [MPa]	1560
t_n^0 [MPa]	39.45	t_s^0 [MPa]	30.2
G_{IC} [N/mm]	0.2	G_{IIC} [N/mm]	0.38

For the adhesive Araldite® 2015, the cohesive laws in the adhesive layer were estimated in previous works [113, 114], thru an inverse method to estimate t_n^0 and t_s^0. Although these works present the method with a detailed description, it basically consists of estimating G_{IC} and G_{IIC} thru DCB and ENF tests, respectively. G_{IC} or G_{IIC} values are used to build a pure mode cohesive law, in the beginning with an approximate value of t_n^0 or t_s^0, estimated from the known properties of the adhesives. This cohesive law is then used in the correspondent numerical model (DCB for tension or ENF for shear) with the same dimensions as the experimental specimen. The t_n^0 or t_s^0 values are therefore estimated using an adjustment procedure between the numerical and experimental *P–δ* curves of the respective fracture characterization test, to obtain an approximate behaviour for the adhesive. Table 13 presents the Araldite® 2015 cohesive parameters used in a mixed-mode cohesive law. The *E* and *G* values were experimental estimated thru bulk and shear tests (TAST), respectively [49].

Table 13 – Tensile and shear cohesive parameters for the adhesive Araldite® 2015

E [MPa]	1850	*G* [MPa]	560
t_n^0 [MPa]	21.63	t_s^0 [MPa]	17.9
G_{IC} [N/mm]	0.43	G_{IIC} [N/mm]	4.70

The cohesive properties of the Sikaforce® 7752 were established in a similar fashion to the Araldite® 2015. Indeed, the shear cohesive law was estimated by an inverse method, obtaining the G_{IIC} value by ENF fracture tests, followed by an iterative manual adjustment to attain t_s^0 [115]. The average values of t_s^0 and G_{IIC} from Azevedo [115] were used, on which deviation between specimens was almost nil, showing the repeatability of the performed tests. For the tensile cohesive law, due to the non-existence of an inverse method applied to this adhesive, a different process was performed. G_{IC} was estimated by the average value of DCB fracture tests [116]. The t_n^0 value was approximated to the average value of bulk specimens' tensile strength on the same work [116]. As established in previous works, for the specific case of a tensile loading, t_n^0 has no significant influence on the results for variations until 25% of t_n^0 established by the

inverse method (variation for both ways) [116], this procedure was not performed. E and G were experimentally estimated by tensile tests to bulk adhesive specimens and TAST shear tests, respectively [116]. Table 14 presents the cohesive parameters of the Sikaforce® 7752 used in a mixed-mode cohesive law.

Table 14 – Tensile and shear cohesive parameters for the adhesive Sikaforce® 7752

E [MPa]	493.81	G [MPa]	187.34
t_n^0 [MPa]	11.49	t_s^0 [MPa]	10.17
G_{IC} [N/mm]	2.36	G_{IIC} [N/mm]	5.41

3.2.3 Stress analysis in the adhesive layer

The next subsections addresses peel (σ_y) and shear (τ_{xy}) stress distributions at the adhesive mid-thickness as a function of L_O. The stress distributions were extracted at the mid-thickness of the adhesive layer, without accounting for the known thickness gradients [117]. The objective of such analysis is to fundament the numerical work and for an easier and comprehensive understanding of the joints' mechanical behaviour. Both stresses were normalized by τ_{avg}, the average value of τ_{xy} along the overlap for each value of L_O [118]. A similar normalization procedure was made for L_O (x/L_O) where x represents the distance from the left edge of the adhesive layer. Therefore x/L_O=0 and x/L_O=1 are the overlap edges.

3.2.3.1 Peel stresses

The plots of σ_y stress distributions in the adhesive layer as function of x/L_O are presented in Figure 70 for the adhesive Araldite® AV138, in Figure 71 for the adhesive Araldite® 2015 and in Figure 72 for the adhesive Sikaforce® 7752. The obtained stress profiles are consistent with published works on this matter [72, 119]. Peel stresses in SLJ occur due to the adherends rotation that induces their separation at the overlap edges and compression in-between. For all adhesives, peel stress singularities exist at the overlap edges at a very restricted region owing to the square edge geometry [120]. This happens due to the sharp geometric change [72] and to the load eccentricity caused by the offset of the adherends, which promotes a bending moment that reflects on the adherends transverse flexure [121]. Peel stresses have their lowest magnitude at the inner overlap region where stresses are compressive. The peak peel stresses at the overlap edges increase with L_O and these are responsible for a significant strength reduction of the bonded joints, constituting one of the main factors for damage initiation at the overlap edges [55, 117].

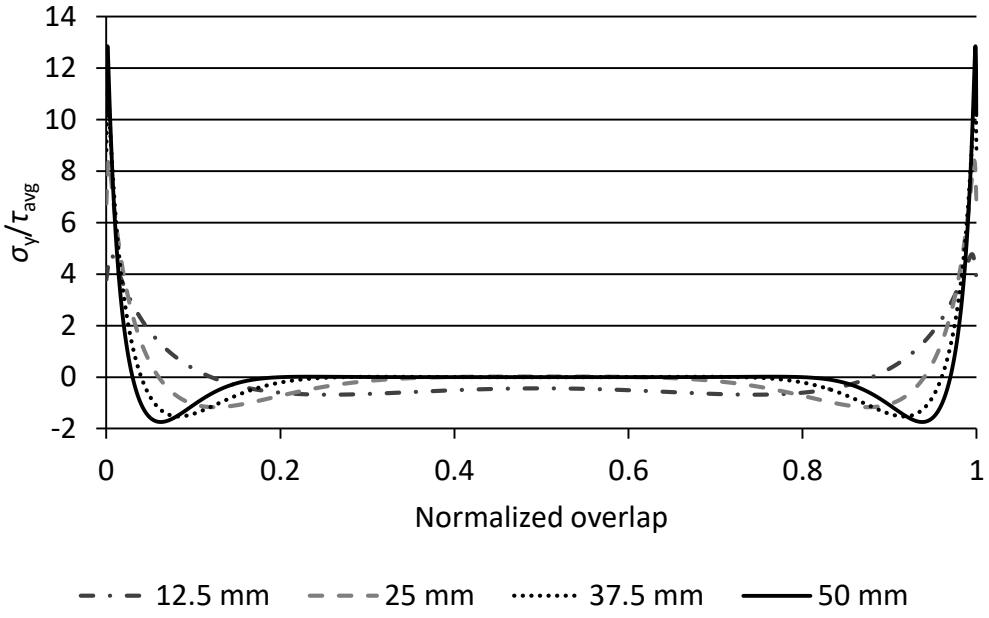

Figure 70 – σ_y stresses as a function of L_O for the adhesive Araldite® AV 138

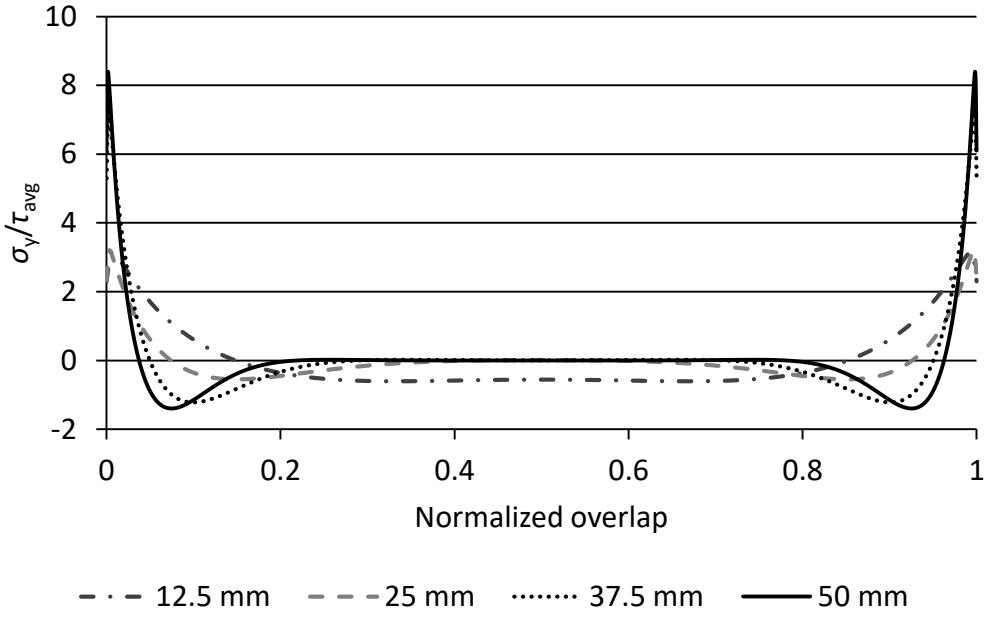

Figure 71 – σ_y stresses as a function of L_O for the adhesive Araldite® 2015

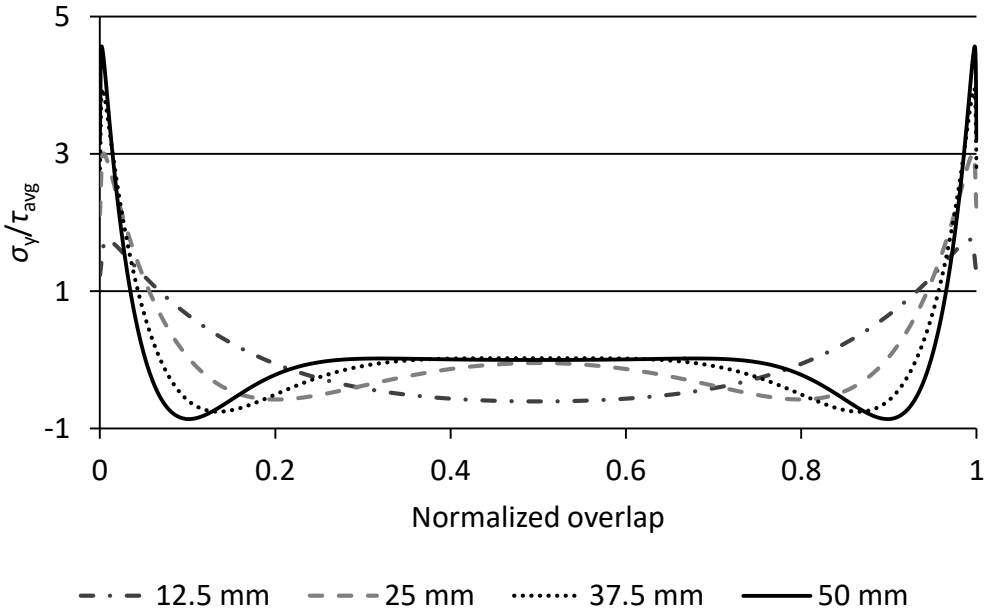

Figure 72 – σ_y stresses as a function of L_O for the adhesive Sikaforce® 7752

The parametric study on L_O for all adhesives shows that σ_y stresses always peak at the overlap edges, concentrating on smaller normalized regions with the increase of L_O. Bigger values of L_O promote the increase of σ_y compressive stresses near the peel singularities, while σ_y compressive stresses diminish in magnitude at the inner region of the overlap. This tendency reduces the peel effects at the overlap edges or prevents crack propagation after localized damage at the square edges [117]. One may observe that the adhesive Araldite® AV 138 attains the highest peaks of σ_y stresses between the three adhesives mainly due to its higher stiffness, which promotes higher stress gradients [122]. The adhesive Sikaforce® 7752 presents, for all values of L_O, peak σ_y stresses of lower magnitude than the adhesives Araldite® AV 138, and Araldite® 2015, due to its flexibility [11]. Peak σ_y stresses for the adhesive Araldite 2015 have an intermediate magnitude between the Araldite® AV 138 and Sikaforce® 7752 mainly due to its moderate flexibility.

3.2.3.2 Shear stresses

The plots of τ_{xy} stress distributions in the adhesive layer as function of a function of x/L_O are presented in Figure 73 for the adhesive Araldite® AV138, in Figure 74 for the adhesive Araldite® 2015 and in Figure 75 for the adhesive Sikaforce® 7752. These plots agree with the reported tendencies for SLJ, in which τ_{xy} stresses peak at the overlap edges and present smaller values at the overlap inner region [123, 124]. This is caused by the adherends' differential deformation along the overlap. Indeed, the adherends are increasingly loaded from their free overlap edge towards the other overlap edge. The practically unloaded free edges of each adherend slide relatively to the matching regions

of the other adherend causing τ_{xy} stress peaks at those regions [20, 117]. τ_{xy} peak stresses also promote damage initiation at the overlap edges, decreasing joint strength more severely for brittle adhesives, which do not allow plasticization at the overlap edges [125]. Contrarily, ductile adhesives allow the redistribution of stress at those regions while the inner region of the overlap is gradually put under loads, masking the stress gradients effect as long as the adhesives' ductility allows, increasing the joint strength [117].

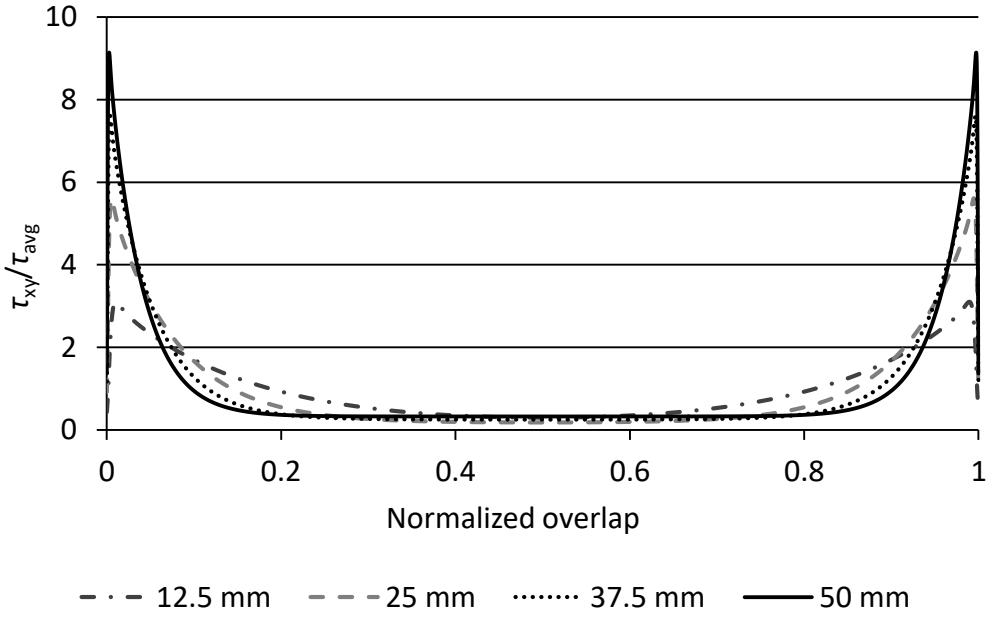

Figure 73 – τ_{xy} stresses as a function of L_O for the adhesive Araldite® AV 138

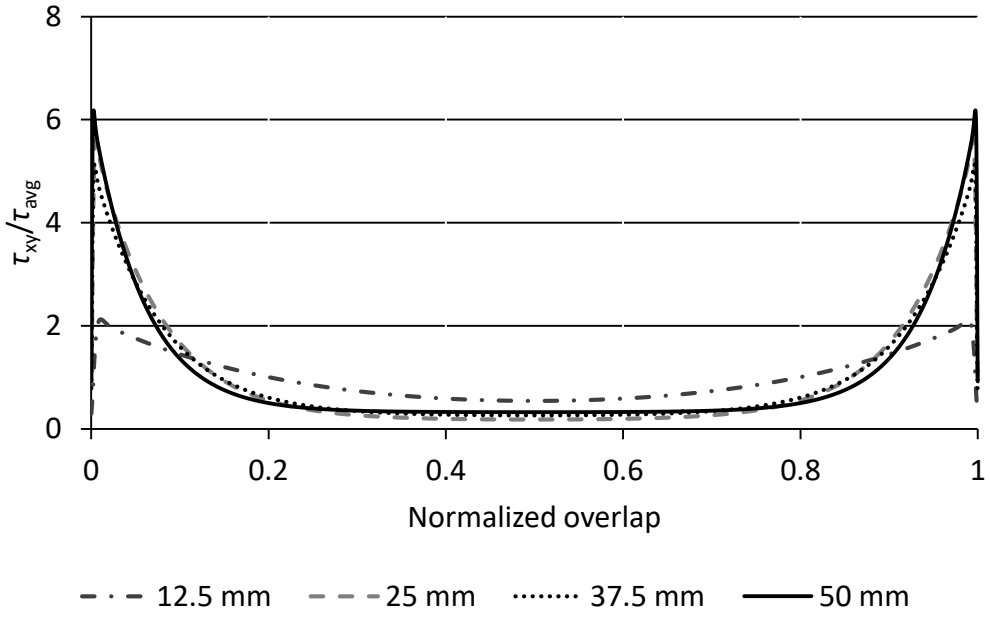

Figure 74 – τ_{xy} stresses as a function of L_O for the adhesive Araldite® 2015

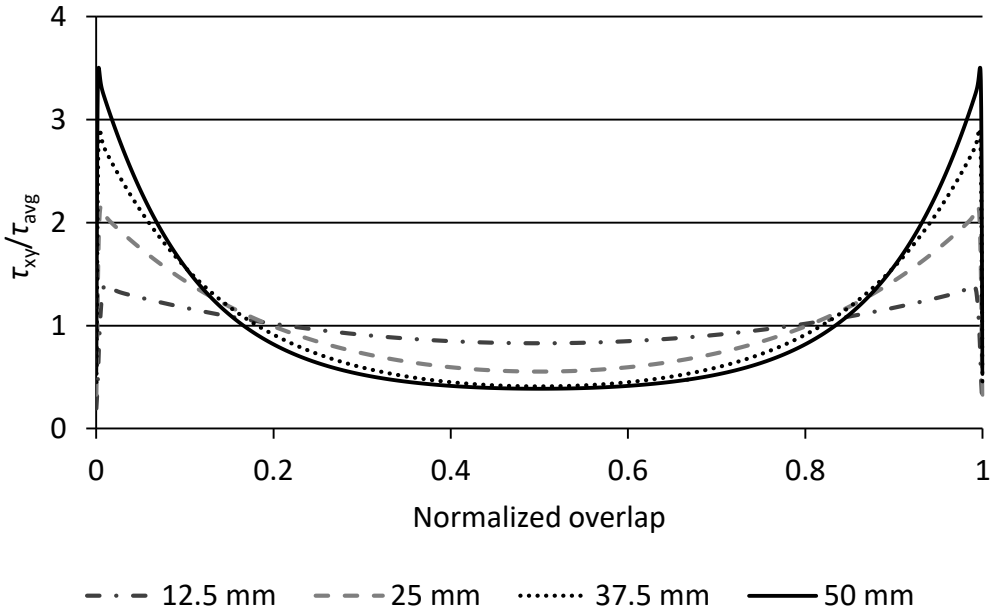

Figure 75 – τ_{xy} stresses as a function of L_O for the adhesive Sikaforce® 7752

The adhesive Araldite® AV138 presents the higher gradient of τ_{xy} stresses due to its higher stiffness. For this adhesive, the overall strength of the joint is affected by the smaller allowable plastic deformation that the adhesive can endure and the strength improvement with L_O should be reduced. On the other hand, the flexibility of the adhesive Sikaforce® 7752 allows a better stress distribution in the adhesive mid-region. Moreover, due to its plasticization ability, the adhesive layer is put under load gradually when the adhesive at the overlap edges starts to plasticize. This should be responsible for a significant improvement of P_m with the increase of L_O [117]. The adhesive Araldite® 2015, due to its' moderate flexibility, presents intermediate gradients of τ_{xy} stresses compared with the other two adhesives. It also has some allowable plasticity, which enables it to undergo some degree of plasticization. Comparing σ_y and τ_{xy} stress distributions gives the awareness of why adhesive bonds should be loaded in shear rather than in peel. The peak stresses are lower under shear loads due to the applied loads and stresses can be spread over larger areas than under peel loads [15].

3.2.4 Strength prediction

This subsection presents an evaluation of the experimental results with support of the stress analysis in the adhesive layer performed in section 3.2.3, and the experimental/numerical comparison of P_m vs. L_O for the three adhesives. To perform the numerical strength prediction, a triangular CZM was considered. The QUADS criterion was used for damage initiation, and the linear energetic criterion for damage growth. Figure 76 reports the comparison for the joints bonded with the adhesive Araldite®

AV138. Figure 77 and Figure 78 present identical comparisons for the adhesives Araldite® 2015 and Sikaforce® 7752, respectively.

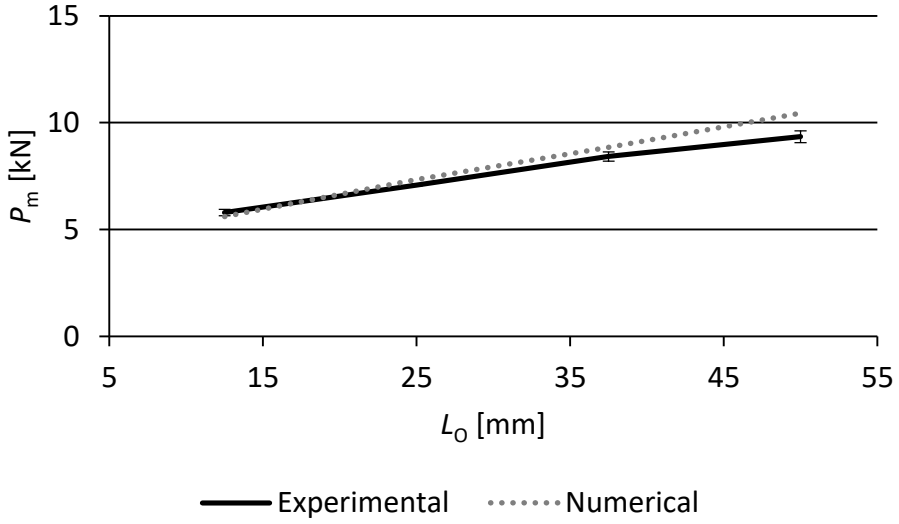

Figure 76 – Experimental and numerical values of P_m vs. L_O for the joints bonded with the adhesive Araldite® AV138

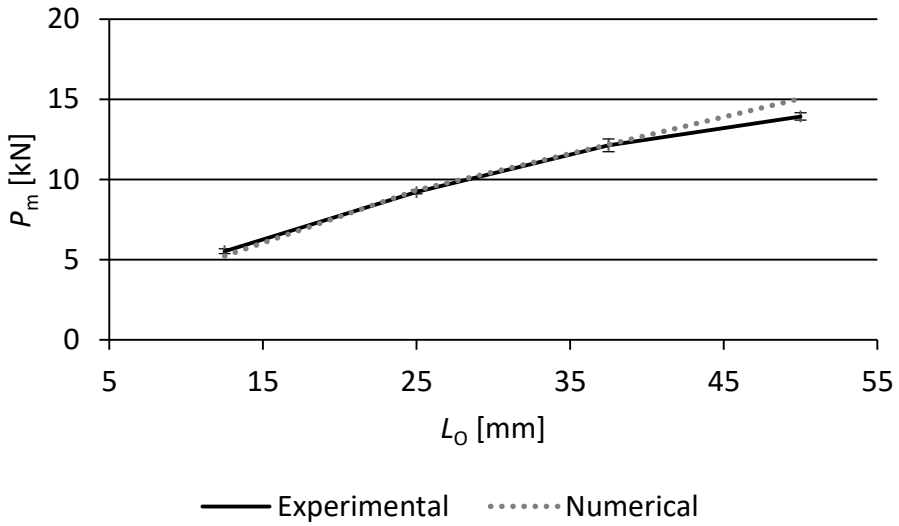

Figure 77 – Experimental and numerical values of P_m vs. L_O for the joints bonded with the adhesive Araldite® 2015

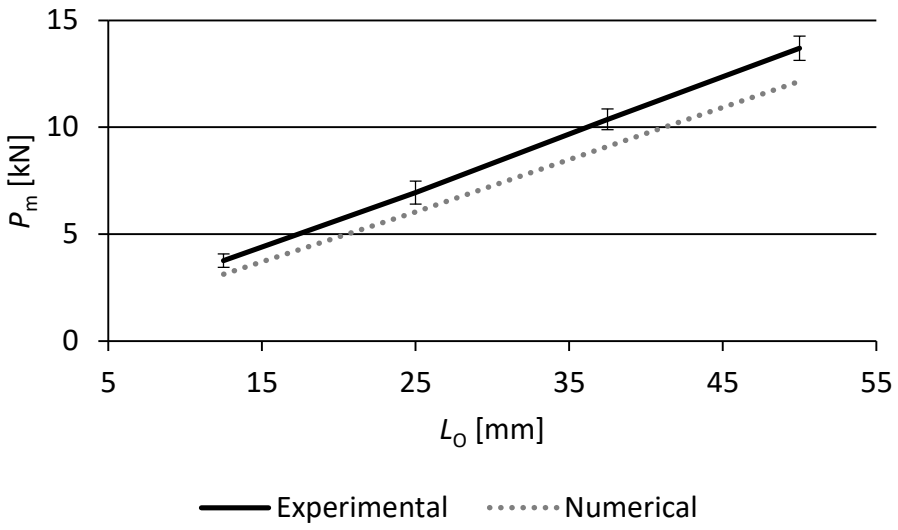

Figure 78 – Experimental and numerical values of P_m vs. L_O for the joints bonded with the adhesive Sikaforce® 7752

According to the experimental results, the three adhesives show different behaviours. The P_m results, although highly influenced by L_O, are also dependent on the adhesives' mechanical properties, such as stiffness, strength and ductility. Indeed, the adhesives' stiffness affects stress fields in such a way that an adhesive with lower stiffness provides a more uniform stress distribution than one with higher stiffness [15], which puts the Araldite® AV138 in disadvantage in view of the values of E presented in Table 3. P_m evolution with L_O for the adhesive Araldite® AV138 was negligible due to is brittleness. By being brittle, this adhesive does not allow plasticization neither redistribution of stresses in the bond line after the failure strength of the adhesive is attained at the overlap edges. Therefore, the joint collapses as soon as the maximum stress are attained [58]. It is important to refer that, due the lack of ductility, increasing L_O brings no significant advantage to the joint strength [117]. Nonetheless, for L_O=12.5 mm, the brittle adhesive presents higher P_m than the other two ductile adhesives. The reasons why Araldite® AV138 performs slightly for lower L_O values are: the fact that adhesive strength has more preponderance for short overlaps, in which σ_y and τ_{xy} stresses became more uniform with the reduction of L_O (Figure 70 and Figure 73) and, due to the inability of plasticization neither redistribution of stresses. As L_O increases the evolution of P_m for the ductile adhesives becomes more notorious. Ductile adhesives manage to redistribute the load and make use of the less stressed parts of the overlap [126]. A ductile adhesive with low strength (Araldite® 2015) reaches the yield strength at the edges of the overlap more quickly but also allows plasticization at those areas (Figure 71 and Figure 74). Thus, the area under the stress curve is higher, conducting to a larger average stress than with a brittle adhesive that fails when adhesive strength is reached on the edges of the adhesive layer [10]. For the Sikaforce® 7752 with L_O=12.5 mm, P_m has the minimum value of the three adhesives, since the strength of joints with short overlaps is governed by the adhesive strengths (due to more uniform stress

distributions), which are the lowest for this adhesive (Figure 72 and Figure 75). With the increase of L_O, P_m also increases, attaining slightly the same value as the Araldite® 2015 for L_O=50 mm. Indeed, the Sikaforce® 7752 is the most ductile adhesive, therefore providing a high value of average stress up to this value of L_O.

Comparing the experimental and numerical results for the adhesive Araldite® AV138 (Figure 76), these were very similar except for L_O=50 mm, with a maximum relative deviation of 11.76%. Lower deviations were attained for smaller L_O values. Actually P_m was underestimated by 3.18% for L_O=12.5 mm and. Contrarily, P_m was overestimated by 3.57 and 5.04% for L_O=25 and 37.5 mm, respectively. Due to the brittleness of the adhesive Araldite® AV138, P_m is attained with minimum plasticization at the overlap edges, justifying the good results obtained with a triangular CZM, whose behaviour is consistent with the absence of plasticity [14]. Figure 77 shows a good correlation for the joints bonded with the adhesive Araldite® 2015, except for L_O=50 mm, where P_m was underestimated by 7.97%. Although this difference is not significant, it contrasts with the correlation found for the other values of L_O. Actually, for the remaining L_O values, smaller P_m deviations were found: -5.55% for L_O=12.5 mm, 1.18% for L_O=25 mm, and 0.48% for L_O=37.5 mm. Possible causes for this difference are small errors induced by the plasticity of the adherends or experimental issues affecting the test results. Overall, despite the moderate ductility of the adhesive Araldite® 2015, the triangular CZM still manages to capture with accuracy the experimental behaviour of the joints [58]. Figure 78 presents numerically underestimated values of P_m for all L_O for the joints bonded with the adhesive Sikaforce® 7752. The deviations were -17.07, -12.89, -12.23, and -11.35% for L_O=12.5, 25, 37.5, and 50 mm, respectively. The under prediction of the P_m values is related to this adhesive's large plasticity, which is not accurately modelled by the triangular CZM considered in this analysis [3].

3.2.5 Influence of different simulation conditions in the numerical analysis

This section presents the influence of different simulation conditions on the numerical analysis to estimate P_m, and evaluation against the experimental data. The variation of the elastic stiffness, the decoupling of the loading modes in the triangular law shape, the effect of different law shapes, the influence of percentile variations of the cohesive parameters, and the evaluation of different initiation and grow criteria, regarding the three different adhesives, are addressed. At the end, the results are discussed.

3.2.5.1 Elastic stiffness of the cohesive law

This subsection addresses the influence of the elastic stiffness of the CZM laws representing the adhesive layer on the joints' strength. A comparison is presented regarding the strength prediction with standard conditions performed in section 3.2.4.

Table 15 presents the *E* and *G* values that were considered for the analysis of the elastic stiffness influence on P_m for the joints bonded with the adhesive Araldite® AV138.

Table 15 – Percentile variation of *E* and *G* values for the adhesive Araldite® AV138

%	25	50	-25	-50
E [MPa]	6112.5	7335	3667.5	2445
G [N/mm]	1.950	2.340	1.170	0.780

Figure 79, Figure 80, and Figure 81 present the strength comparison of the adhesives Araldite® AV138, Araldite® 2015, and Sikaforce® 7752, respectively, with different values of *E* and *G*. P_m^0 represents the strength predicted in section 3.2.4 (without stiffness variation).

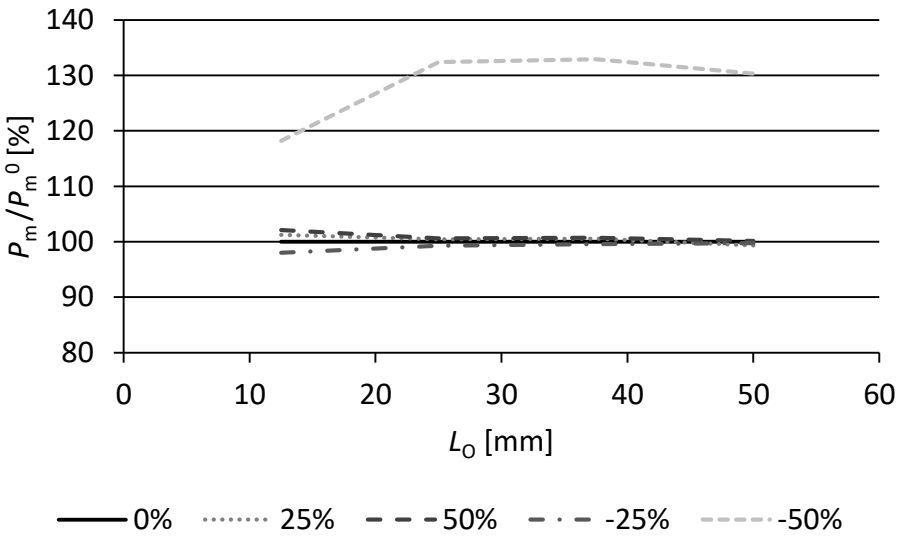

Figure 79 – Percentile variation of P_m/P_m^0 with different values of elastic stiffness for the joints bonded with the adhesive Araldite® AV138

For the adhesive Araldite® AV138 (Figure 79) it was observed that, generally, only for a big reduction of the elastic stiffness, a noteworthy variation of P_m/P_m^0 was found. Actually, decreasing the stiffness by 50%, the strength was overestimated up to 32.95% (L_O=37.5 mm). For the remaining elastic stiffness values variations, the deviations were negligible, although highest for L_O=12.5 mm (-1.97% for properties variations of -25%, 1.22% for properties variations of 25%, 2.11% for properties variations of 50%). The big strength improvement obtained by reducing the stiffness by 50% is due to the reduction stress gradients along the adhesive layer, i.e. the stresses become more uniform along the bonded length. In the presence of a brittle adhesive such as the Araldite® AV138 this modification is prone to have a significant effect on P_m because brittle adhesives fail when their limiting strengths are attained anywhere in the joints. Thus, the reduction of peak stresses at the overlap edges highly increases the joint strength.

Table 16 presents the *E* and *G* values that were considered to the analysis of the joints bonded with the adhesive Araldite® 2015.

Table 16 – Percentile variation of *E* and *G* values for the adhesive Araldite® 2015

%	25	50	-25	-50
E [MPa]	2312.5	2775	1387.5	925
G [N/mm]	0.7	0.84	0.42	0.28

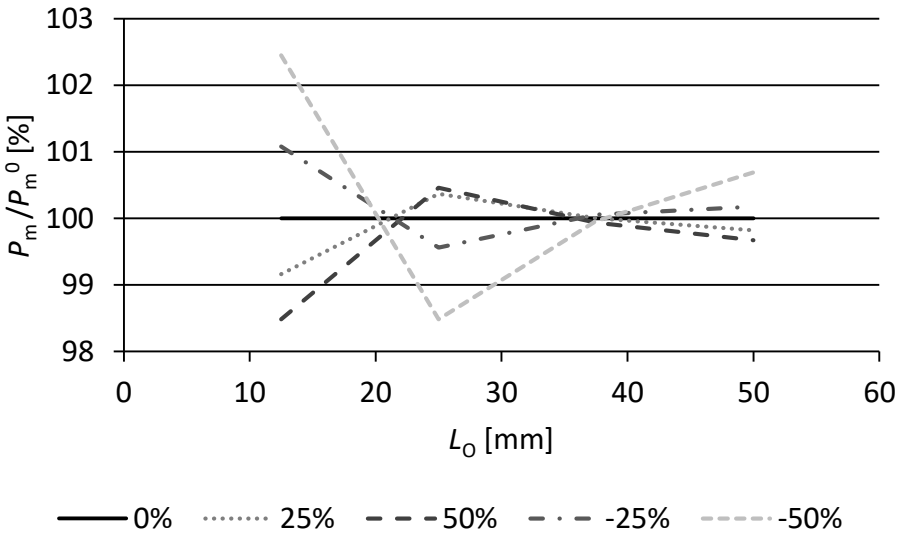

Figure 80 – Percentile variation of P_m/P_m^0 with different values of elastic stiffness for the joints bonded with the adhesive Araldite ® 2015

The elastic stiffness influence on P_m/P_m^0 for the adhesive Araldite® 2015 (Figure 80) reveals low strength variation effect. Indeed, the maximum relative deviation (2.45%) was found for L_O=12.5 mm with a reduction of the elastic stiffness of 50%. Still referring to L_O=12.5 mm, the deviations were -1.28, 0.84, and 1.52% for stiffness variation of -25, 25, and 50% respectively. For L_O=25 and 50 mm the deviations were insignificant, although the maximum deviation found for L_O=25 mm with properties reduction of 50% was 1.52%. For L_O=37.5 mm the deviations were almost nil with the stiffness variation. Thus, the behaviour is significantly different relatively to that of the Araldite® AV138. This is due to the ductility of this adhesive, which makes the behaviour of the respective joints less dependent on peak stresses in the adhesive layer. Actually, the ductility of this adhesive allows it to undergo plasticization when the peak strengths of the adhesive are attained at the overlap edges and, consequently, to redistribute stresses such that the strength of the joint is not that much affected by variations in the stiffness of the adhesive and respective modifications of the stress fields.

Table 17 represents the *E* and *G* values that were considered for the analysis for the joints bonded with the adhesive Sikaforce® 7752.

Table 17 – Percentile variation of *E* and *G* values for the adhesive Sikaforce® 7752

%	25	50	-25	-50
E [MPa]	617.2625	740.715	370.3575	246.905
G [N/mm]	234.6875	281.625	140.8125	93.875

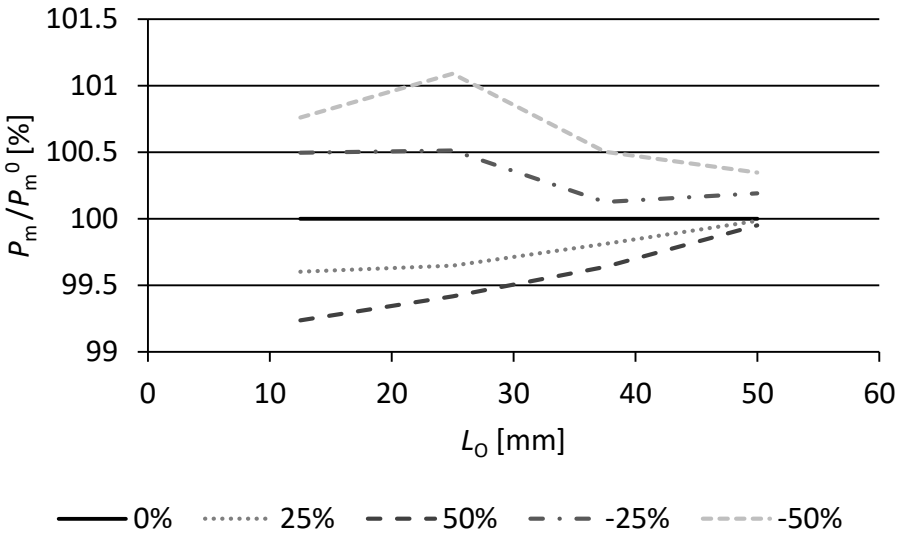

Figure 81 – Percentile variation of P_m/P_m^0 with different values of elastic stiffness for the joints bonded with the adhesive Sikaforce® 7752

The stiffness variation for the joints bonded with the adhesive Sikaforce® 7752 (Figure 81) promotes an even smaller variation on P_m/P_m^0. The maximum relative deviation was 1.09%, for L_O=25 mm with the elastic stiffness decreased by 50%. For L_O=12.5 mm, deviations were practically nil, with deviations of 0.76, and -0.75% for properties variations of 50, and -50% respectively. For higher values of L_O low deviations were found on P_m/P_m^0., with a maximum deviation of 0.50% for L_O=37.5 mm. Stiffness variation shows no improvement on the strength of the joints bonded with the adhesive Sikaforce® 7752. Being an even more ductile adhesive than the previous one, its plasticization capacity is notorious, which allows a distribution of stress fields along the bonded area. Thus, the elastic stiffness variation results in the smallest influence on strength between the three adhesives.

3.2.5.2 Decoupling of the loading modes in the triangular CZM

Figure 82, Figure 83, and Figure 84 present the comparison between the experimental data, the strength predicted in subsection 3.2.4 (mixed-mode model), and P_m obtained for the adhesives Araldite® AV138, Araldite® 2015, and Sikaforce® 7752, respectively, using a triangular CZM with decoupled modes.

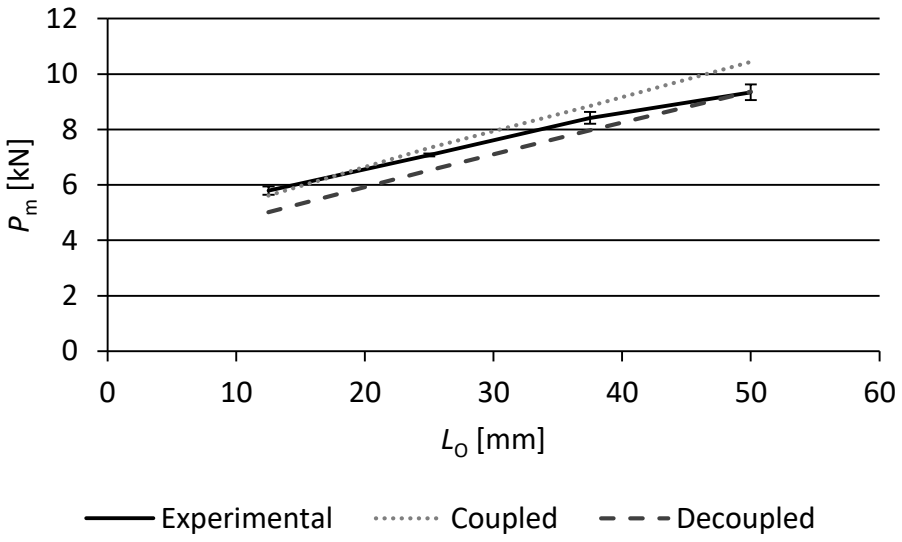

Figure 82 – Comparison between different loading modes for the joints bonded with the adhesive Araldite® AV138

For the adhesive Araldite® AV138, strength prediction with the decoupled mode (Figure 82), was underestimated for all values of L_O, except for L_O=50 mm. The maximum relative deviation to the experimental data was 13.37% for L_O=12.5 mm, while for L_O=25mm P_m was underestimated by 7.79%, for L_O=37.5 mm by 5.28%, and for L_O=50 mm by 0.23%. The comparison of the decoupled with the mixed-mode results also shows a P_m underestimation. P_m by the decoupled model was under predicted by 11.76% for L_O=12.5 mm, by 12.33 for L_O=25 mm, by 10.89 for L_O=37.5 mm, and by 11.50% for L_O=50 mm.

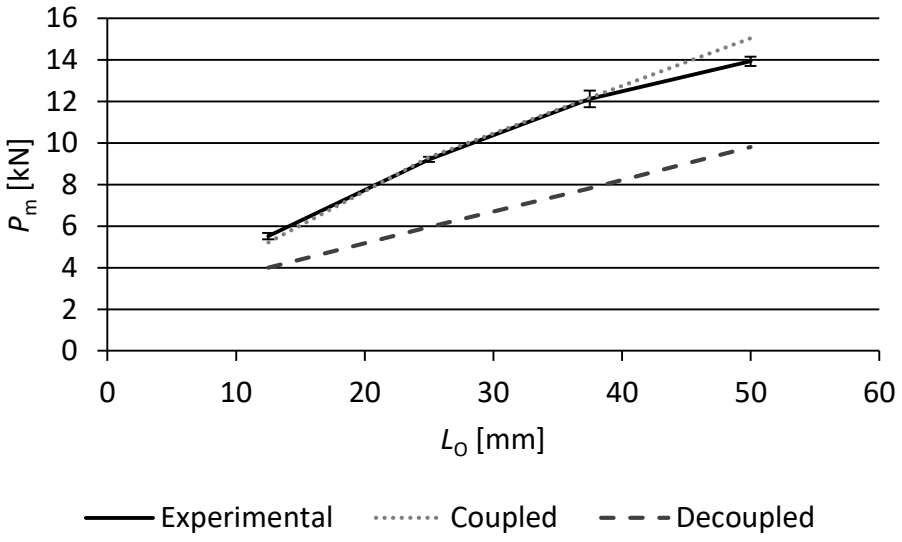

Figure 83 – Comparison between different loading modes for the joints bonded with the adhesive Araldite ® 2015

The analysis performed with the adhesive Araldite® 2015 (Figure 83) shows even worst results than the previous adhesive. Regarding the experimental data, for all L_O values P_m was underestimated. The maximum relative deviation was 35.52% for L_O=37.5 mm. For the remaining L_O values the deviations were -27.39% for L_O=12.5 mm, -35.34% for L_O=25 mm, and -29.61% for L_O=50 mm. Comparing both coupled and decoupled modes, P_m was once more under predicted for all L_O values by the decoupled model. Indeed the deviations were 30.07% for L_O=12.5 mm, 56.49% for L_O=25 mm, 55.80% for L_O=37.5 mm and 53.38% for L_O=50 mm.

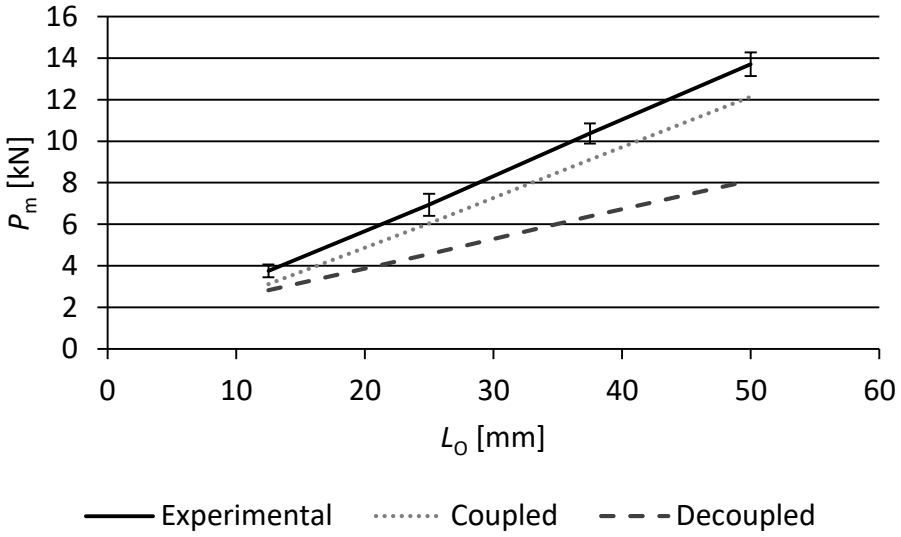

Figure 84 – Comparison between different loading modes for the joints bonded with the adhesive Sikaforce® 7752

The comparison regarding the experimental data and the decoupled model for the adhesive Sikaforce® 7752, depicted in Figure 84, shows a P_m underestimation for all L_O values. The maximum deviation was 40.80% for L_O=50 mm, while for L_O=37.5 mm, P_m was under predicted by 38.44%, for L_O=25 mm by 34.21%, and for L_O=12.5 mm by 24.79%. The evaluation of both couple and decoupled mode shows P_m under predictions of the decoupled model with higher deviations as L_O increases. Beginning with L_O=12.5 mm, P_m was offset by 10.27%, for L_O=25 mm by 32.40%, for L_O=37.5 by 42.58%, and for L_O=50 mm by 49.75%.

3.2.5.3 Cohesive law shape

In the following analysis, triangular, exponential and trapezoidal CZM shapes were used to model the thin adhesive layer, to estimate their influence on the strength predictions. An uncoupled mode analysis was carried out for the three CZM law shapes to provide identical analysis conditions, since coupled trapezoidal and exponential models are not readily available in Abaqus®. The comparison that follows regards the experimental data, the strength prediction performed on section 3.2.4 considering a mode-coupled

triangular law, as well as the current analysis on the three different CZM shapes. Figure 85 shows the influence of the different CZM shapes on P_m for the joints bonded with the adhesive Araldite® AV138.

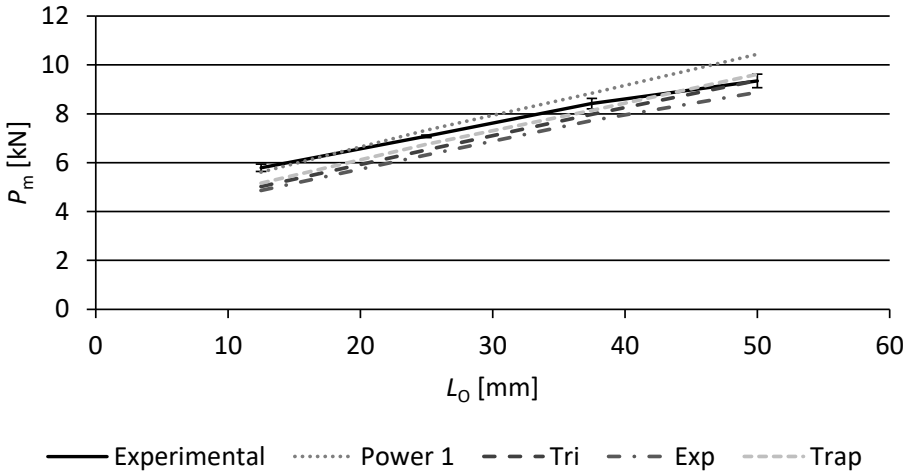

Figure 85 – Comparison between the different cohesive law shapes for the joints bonded with the adhesive Araldite® AV138

The results presented in Figure 85 show that, for the uncoupled CZM laws, the trapezoidal law approximates the best the experimental data. For lower values of L_O the trapezoidal law underestimates P_m (by 10.94 and 4.58% for L_O=12.5 and 25 mm, respectively). However, for larger values of L_O, the triangular law suits best, underestimating P_m by 5.28% for L_O =37.5 mm and, for L_O=50 mm, giving an overestimation of 0.24%. The average absolute deviations found for the uncoupled CZM results were: 5.44% for trapezoidal law, 6.67% for triangular law and 10.03% for the exponential law. Although it was expected that the triangular CZM would give the best results for all joint conditions, the small errors introduced by considering uncoupled modes explain why, for some L_O values, the trapezoidal law represents best the experimental data.

Figure 86 depicts the influence of the different CZM laws for the joints bonded with the adhesive Araldite® 2015. The performance of the three laws was very similar, presenting a linear evolution with the increase of L_O. The average absolute deviations found for the uncoupled CZM results were: 30.73% for trapezoidal law, 31.96% for triangular law and 32.74% for the exponential law. However, P_m was underestimated for all L_O values. The maximum relative deviation was 36.24%, found for L_O=25 mm with the exponential law, and the minimum relative deviation was 27.39% for L_O=12.5 mm with the triangular law. Comparing the results with those of the Araldite® AV138, a higher under prediction is found with respect to the mixed-mode results, showing that ductile adhesives are more sensitive to the uncoupling between modes.

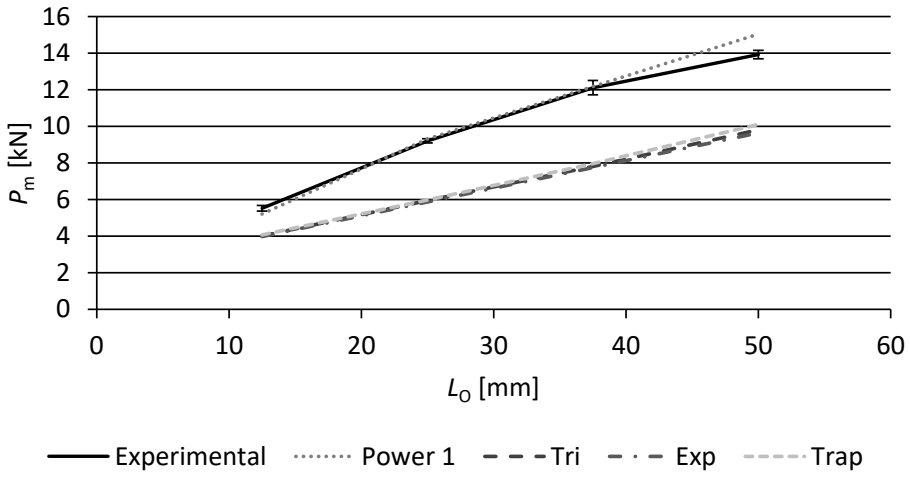

Figure 86 – Comparison between the different cohesive law shapes for the joints bonded with the adhesive Araldite® 2015

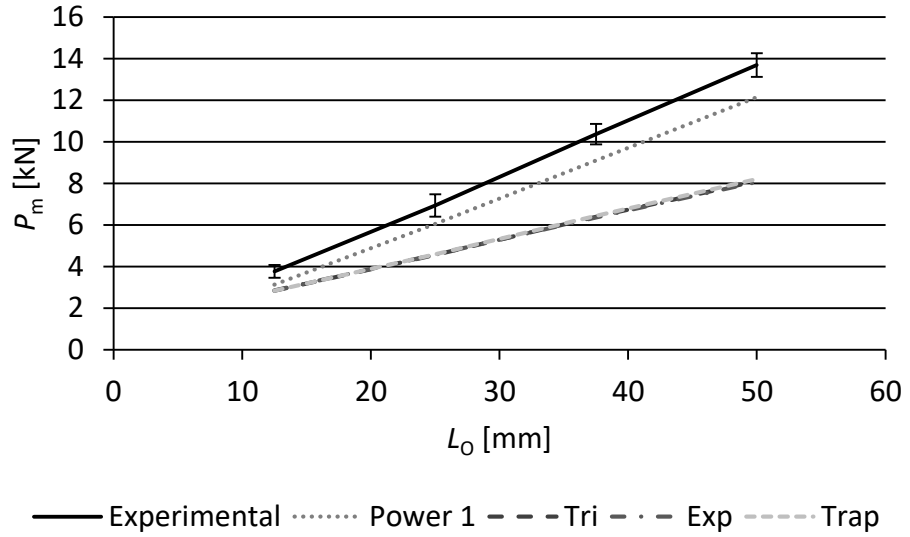

Figure 87 – Comparison between the different cohesive law shapes for the joints bonded with the adhesive Sikaforce® 7752

The data for the adhesive Sikaforce® 7752 (Figure 87) shows, as the previous adhesive, similarity between the three laws for all L_O values, presenting also an increased underestimation of P_m for bigger L_O values. For L_O=12.5 mm P_m was underestimated by 24.59%, and for L_O=50 mm by 40.67% (average for the three CZM laws). These results confirm that ductile adhesives are more affected by the approximation of uncoupling both loading modes than brittle adhesives.

3.2.5.4 Cohesive parameters

This subsection addresses the influence of the cohesive parameters variation (G_{Ic}, G_{IIc}, t_n^0, t_s^0, and their combined effect) on the joints' strength. Their influence on the value of P_m/P_m^0 of the joints is numerically assessed (in this analysis, P_m^0 represents P_m for the initial parameters). Percentile variations of the initial properties between -50 to +50% were considered, whilst the non-mentioned cohesive parameters in all analyses were kept unchanged regarding the standard values. Table 18 shows the percentile variation values of t_n^0 and G_{IC} for the adhesive Araldite® AV138. Figure 88, and Figure 89 present the study of the influence of t_n^0 and G_{IC} on P_m/P_m^0 for the adhesive Araldite® AV138.

Table 18 – Percentile variation of t_n^0 and G_{IC} values for the adhesive Araldite® AV138

%	25	50	-25	-50
t_n^0 [MPa]	49.3125	59.175	29.5875	19.725
G_{IC} [N/mm]	0.375	0.45	0.225	0.15

Figure 88 shows that positive variations of t_n^0 have no significant influence on the joint strength, with the exception of L_O=50mm, in which P_m/P_m^0 was under predicted by 1.56% (for t_n^0=+50%), and by 0.97% (for t_n^0=+25%). The reduction of t_n^0 results on a low P_m/P_m^0 improvement, yet more notorious with t_n^0 reduced by 50% of the initial value. The strength was increased by 2.00% for L_O=12.5%, by 2.70% for L_O=25 mm, by 4.37% for L_O=37.5 mm, and by 5.02% for L_O=50 mm. The t_n^0 value variation of -25%, attained a P_m/P_m^0 over prediction of 1.54% (L_O=37.5 mm), and 1.51% for L_O=50 mm. A lower influence on P_m/P_m^0 was achieved by over predicting t_n^0 rather than under predicting [62]. It was found that smaller values of t_m^0 promote an increase of δ_n^f which is positive for the overall joint strength.

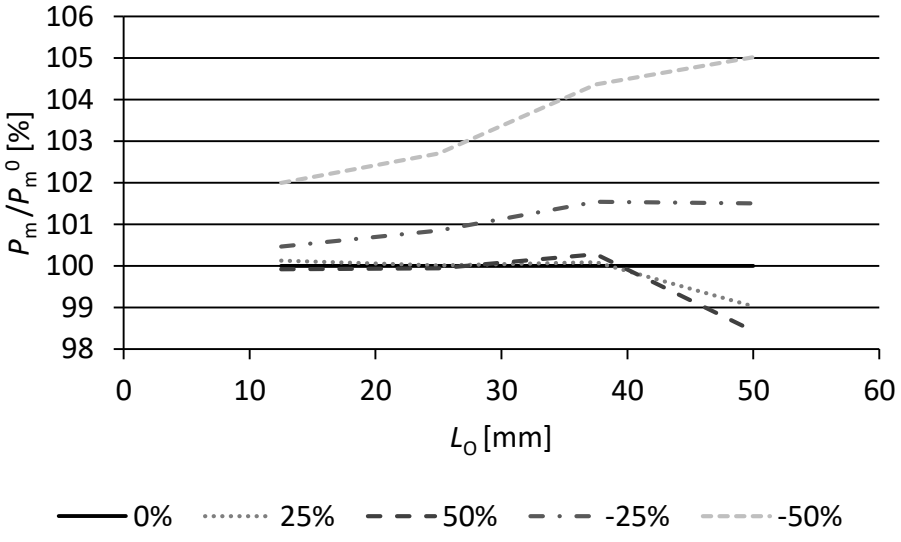

Figure 88 – Percentile variation of P_m/P_m^0 with t_n^0 values ranging from -50 to +50% of the initial ones in adhesive Araldite® AV138

Figure 89 depicts the strength influence of percentile variations of G_{IC} on the joints bonded with the adhesive Araldite® AV138. Positive variations result on a joint strength improvement by 5.46%, and by 9.69% for G_{IC} overestimations of 25, and 50%, respectively. Reduction of the initial G_{IC} leads to a strength reduction of 7.05% for -25%, and -16.78% attained with the variation of -50%. The results for all variations of G_{IC} are identical irrespectively of L_O. The significant strength decline attained by G_{IC} reductions occurs due the smaller values of δ_n^f (Figure 28 a) in the tensile cohesive law, resulting on the premature failure at the overlap edges. Higher G_{IC} values promote a lesser strength influence than the lower ones. This difference is related to the sole attainment of large δ_n values bigger than δ_n^f for the initial parameters (Figure 28 a) at the overlap edges.

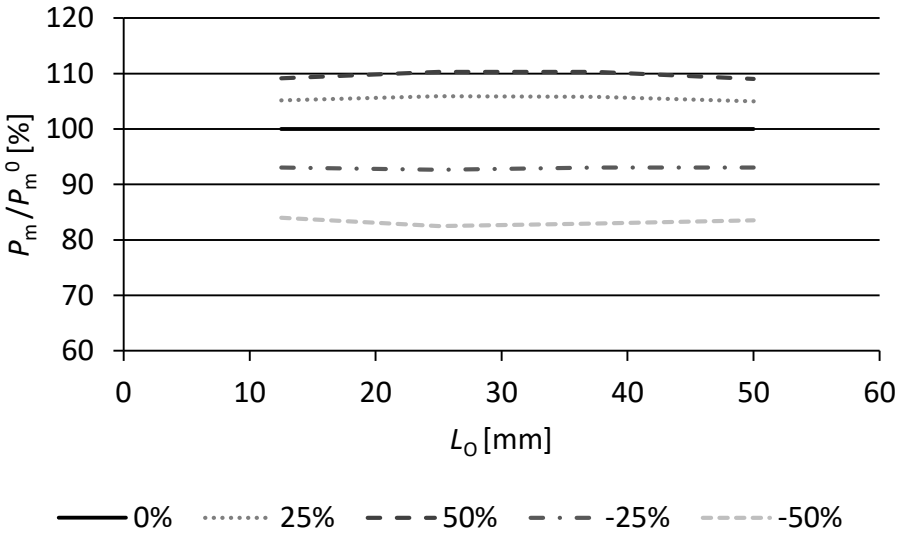

Figure 89 – Percentile variation of P_m/P_m^0 with G_{IC} values ranging from -50 to +50% of the initial ones in adhesive Araldite® AV138

Table 19 reveals the values used to study the t_s^0 and G_{IIC} influence on P_m/P_m^0 for the adhesive Araldite ® AV138. Figure 90 and Figure 91 depict the corresponding results for the adhesive Araldite® AV138.

Table 19 – Percentile variation of t_s^0 and G_{IIC} values for the adhesive Araldite® AV138

%	25	50	-25	-50
t_s^0 [MPa]	37.75	45.3	22.65	15.1
G_{IIC} [N/mm]	0.75	0.9	0.45	0.3

By comparison with the initial parameters, raised t_s^0 values reveal low strength improvement (Figure 90). Indeed, 2.89% was the maximum deviation found with t_s^0 higher by 50%. Decreasing t_s^0 by 25% also results in a small influence on P_m/P_m^0. In fact, the maximum deviation was -5.25%, for L_O=12.5 mm. Reducing t_s^o by 50% in joints with

small L_O values promotes a noteworthy reduction of the joint strength. Actually the maximum deviation was -16.22% for L_O=12.5 mm. The remaining underestimations were 9.88% for L_O=25 mm, by 6.79% for L_O=37.5 mm, and by 6.70% for L_O=50 mm. With high L_O values, smaller deviations are observed. The large P_m reduction by diminishing t_s^0 by 50% for short overlaps is due to the fact that this parameter is the main responsible for the transmission of stresses along the overlap, because under this conditions shear stresses are almost uniform.

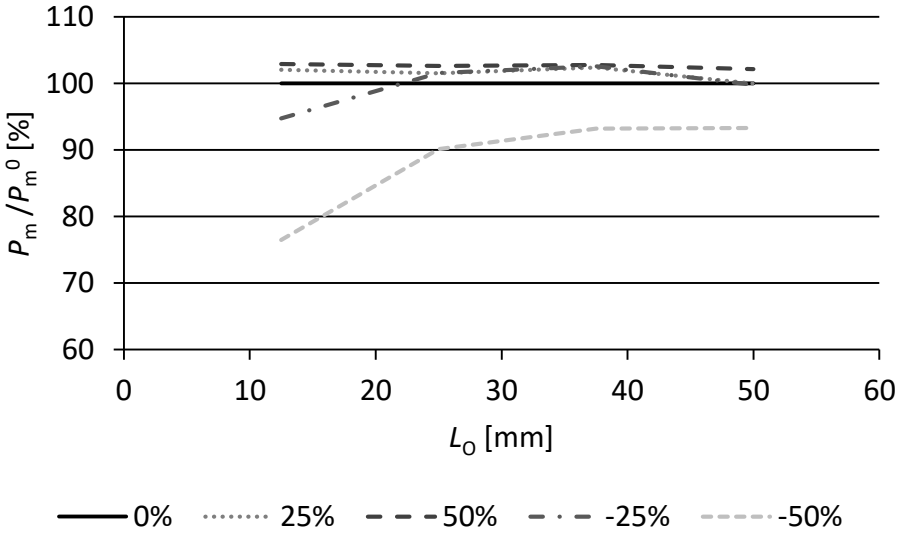

Figure 90 – Percentile variation of P_m/P_m^0 with t_s^0 values ranging from -50 to +50% of the initial ones in adhesive Araldite® AV138

Figure 91 reports the G_{IIC} percentile variation influence on the joints bonded with the adhesive Araldite® AV138. Increasing G_{IIC} enhances the joint strength, with better performance for higher L_O values. Raising G_{IIC} value by 25% of the initial one overestimates P_m/P_m^0 by ≈5% for minor L_O lengths (average deviation for L_O=12.5, 25 and 37.5 mm), and by 10.94% for L_O=50 mm. A similar tendency is observed with G_{IIC} percentile variation of +50%, attaining an average over prediction of 8.75% for lower L_O lengths (12.5, 25 and 37.5 mm), and 16.18% for L_O=50 mm. On the other hand, by decreasing G_{IIC}, the joint strength diminishes, by a slightly higher amount for bigger L_O values. For G_{IIC} reduction of 25%, the deviations ranges between -6.77% for L_O=12.5 mm and -9.08% for L_O=50 mm. Decreasing G_{IIC} by 50% of the initial one induces a strength underestimation of 16.22 for L_O=12.5 mm, of 18.11% for L_O=25 mm, of 18.98% for L_O=37.5 mm, and of 21.78% for L_O=50 mm. Generally, the increase or reduction of P_m follows similar variations of G_{IIC} because of the importance of this parameter for the joint strength, with a higher influence for bigger L_O values because of the higher stress gradients under this conditions.

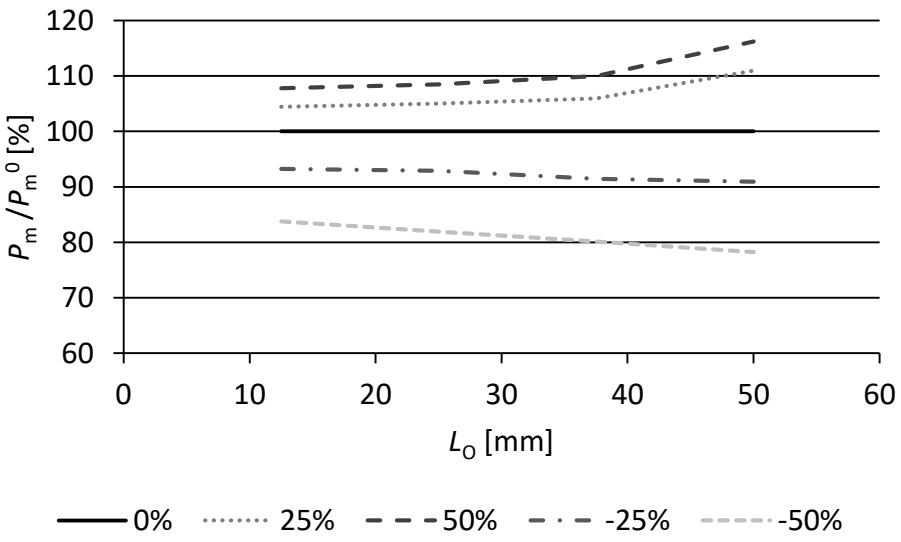

Figure 91 – Percentile variation of P_m/P_m^0 with G_{IIC} values ranging from -50 to +50% of the initial ones in adhesive Araldite® AV138

Table 20 presents the considered values to perform the analysis of the influence of all cohesive properties on the joints strength for the adhesive Araldite® AV138. Figure 92 depicts such influence on P_m/P_m^0.

Table 20 – Percentile variation of all cohesive parameters plus *E* and *G* for the adhesive Araldite® AV138

%	25	50	-25	-50
t_n^0 [MPa]	49.3125	59.175	29.5875	19.725
t_s^0 [MPa]	37.75	45.3	22.65	15.1
G_{IC} [N/mm]	0.375	0.45	0.225	0.15
G_{IIC} [N/mm]	0.75	0.9	0.45	0.3
E [MPa]	6112.5	7335	3667.5	2445
G [N/mm]	1.950	2.340	1.170	0.780

Generally, the shape of the plots presented in Figure 92 is quite similar to that of the G_{IC} variation influence, with approximated constant values with no dependence on L_O, although with higher relative deviations. For positive percentile variations on the global cohesive parameters the strength is upraised in general by 14.39% (accredited to parameters increased by 25% of the initial ones), and by 27.41% (for a 50% variation). The reduction of the cohesive parameters promotes a bigger influence on the joint strength, more noticeable with higher percentile variations. Indeed, for a 50% decrease, P_m/P_m^0 diminishes by average 35.24% (for all L_O). For a 25% reduction of the initial cohesive parameters, the strength is affected in average by -16.24% (for all L_O), resulting in an identical deviation to increasing the parameters by 25%.

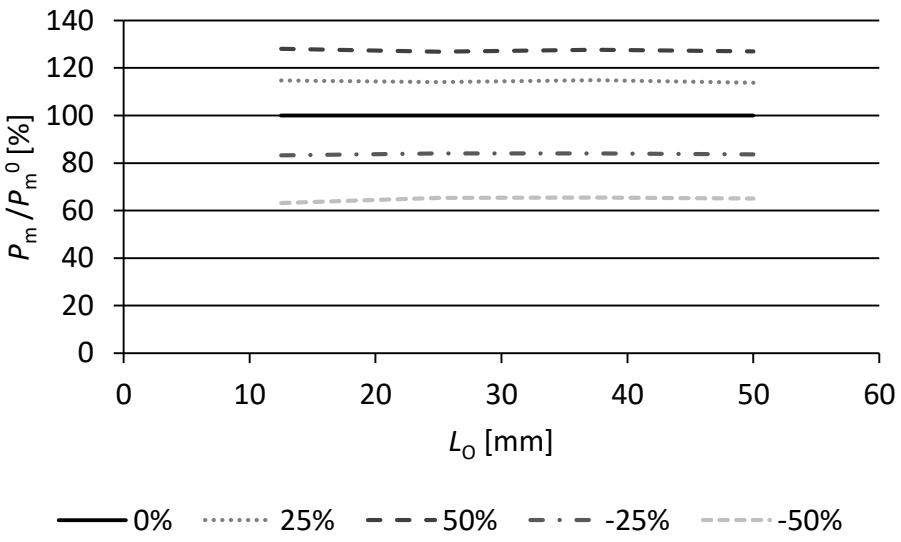

Figure 92 – Percentile variation of P_m/P_m^0 with different values of all cohesive parameters plus E and G ranging from -50 to +50% of the initial ones in adhesive in adhesive Araldite® AV138

Table 21 presents the t_n^0 and G_{IC} values affected by different percentile variations, used to study their influence on P_m/P_m^0 for the adhesive Araldite® 2015. The comparison plots of the t_n^0 and G_{IC} evaluation are depicted in Figure 93 and Figure 94, respectively, for the adhesive Araldite® 2015.

Table 21 – Percentile variation of t_n^0 and G_{IC} values for the adhesive Araldite® 2015

%	25	50	-25	-50
t_n^0 [MPa]	27.038	32.445	16.223	10.815
G_{IC} [N/mm]	0.538	0.645	0.323	0.215

Figure 93 reports a certain influence of t_n^o on P_m/P_m^0 for the lower values of L_O, for negative percentile variations of t_n^0. Indeed, the maximum relative deviation was 8.28% found for L_O=12.5 mm, with t_n^0 decreased by 50% of the initial one. For the same L_O, with a parameter decrease of 25% the strength diminished 2.79%, while higher values of t_n^0 by 25 and 50% result in lower strength improvements of 1.59 and 2.57%, respectively. Increasing L_O significantly reduces the influence of t_n^0 on P_m/P_m^0. Yet, a deviation of -6.89% was found for L_O=25 mm, for t_n^0 decreased by 50%. Just like it was found in the evaluation of the joints bonded with the adhesive Araldite® AV138, a lower influence on P_m/P_m^0 was achieved by over predicting t_n^0 rather than under predicting [62]. Undeniably, over predicting t_n^0 manages low influence of t_n stresses in the damage initiation criterion. Oppositely, the under prediction of t_n^0 enables a premature occurrence of t_m^o, owing to the larger influence of t_n in the damage criterion. However, the analysis performed for the adhesive Araldite® 2015, shows lower t_n^0 impact on P_m/P_m^0 for higher L_O values. This behaviour is due to concentration of peel δ_n values

occurred at a smaller normalized region at the overlap edges with the increase of L_O. Actually, variation of t_n^0 affects δ_n^f in order to keep G_{IC} constant (Figure 29).

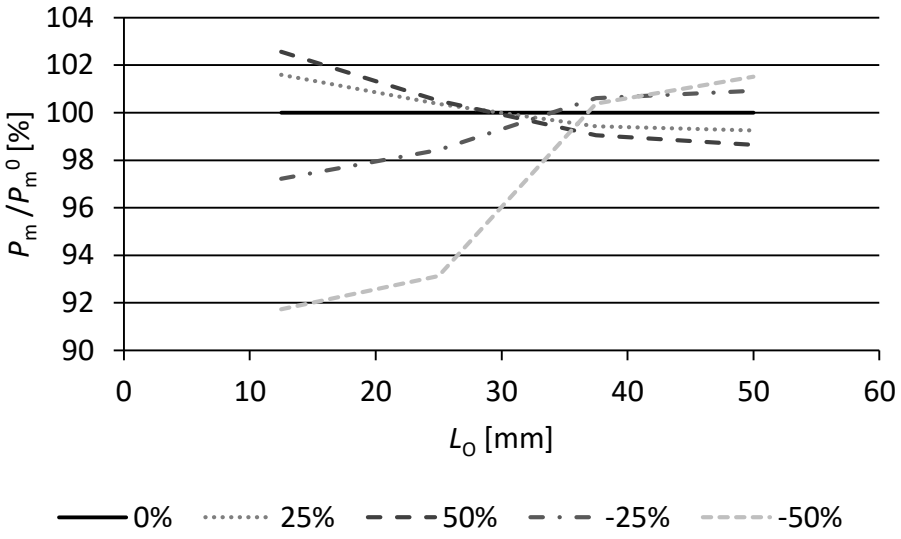

Figure 93 – Percentile variation of P_m/P_m^0 with t_n^0 values ranging from -50 to +50% of the initial ones in adhesive Araldite® 2015

Figure 94, relating to G_{IC}, shows a larger influence on P_m/P_m^0 for reductions of G_{IC}, with the exception for L_O=12.5 mm (presenting practically nil deviations with all G_{IC} values variation). Concerning to G_{IC} reduction of 50%, P_m decreases by 21.77% for L_O=25 mm, by 24.18% for L_O=37.5 mm, and by 23.77% for L_O=50 mm. For a variation of -25%, P_m also reduces in average by 9.74% for L_O=25, 37.5, and 50 mm. On the other hand, increasing G_{IC} gives improvements of P_m/P_m^0. The increase of G_{IC} by 25%, enhances P_m by 4.53, 7.95, and 7.73% for L_O=25, 37.5 and 50 mm respectively. Over predicting G_{IC} by 50% increases P_m by 6.35% for L_O=25 mm, by 14.64% for L_O=37.5 mm, and by 15.97% for L_O=50 mm. The behaviour of this adhesive with variations of G_{IC} is somehow identical to that observed for the Araldite® AV138 although with a much lesser influence for small L_O values. The significant under prediction of P_m/P_m^0 for reductions of G_{IC} occurred due to the smaller values of δ_n^f in the tensile cohesive law, which promote a premature failure at the overlap edges.

Table 22 shows the t_s^0 and G_{IIC} values that were used to evaluate their influence on the joint strength for the Araldite® 2015. The percentile variation of P_m against the initial values for the same adhesive is presented in Figure 95 and Figure 96.

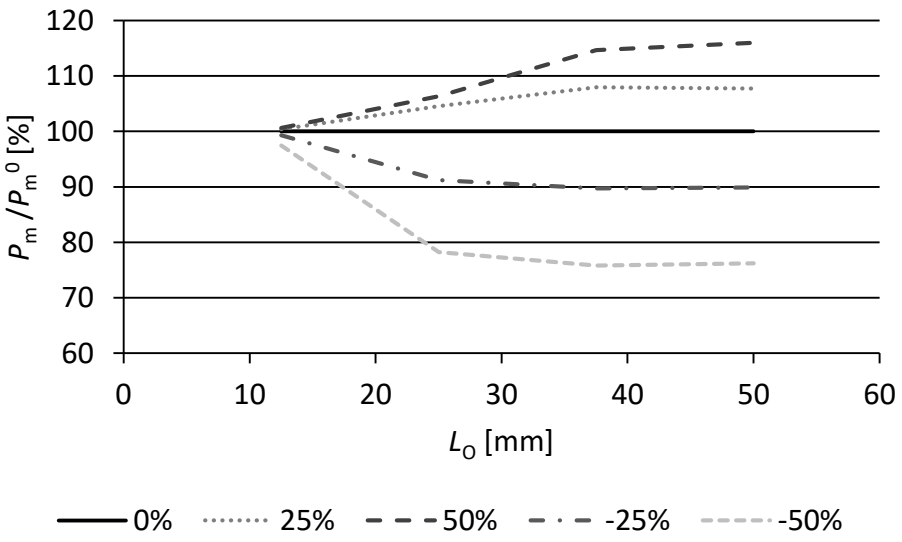

Figure 94 – Percentile variation of P_m/P_m^0 with G_{IC} values ranging from -50 to +50% of the initial ones in adhesive Araldite® 2015

Table 22 – Percentile variation of t_s^0 and G_{IIC} values for the adhesive Araldite® 2015

%	25	50	-25	-50
t_s^0 [MPa]	22.375	26.850	13.425	8.950
G_{IIC} [N/mm]	5.875	7.050	3.525	2.350

As depicted in Figure 95, percentile variations of t_s^0 show a high influence on P_m/P_m^0, which tends to decay with the increase of L_O. The most significant change on the joint strength was attained by decreasing t_s^0 by 50%, attaining -47.37% for L_O=12.5 mm, -42.02% for L_O=25 mm, -33.87% for L_O=37.5 mm, and -28.95% for L_O=50 mm. Reducing t_s^o by 25% also has a significant influence for the lowest L_O (-22.86%) while, by increasing L_O, the deviations become smaller: -16.94, -7.96 and -5.99% for L_O= 25, 37.5, and 50 mm, respectively. Contrarily, positive percentile t_s^o variations of the initial one accomplished significantly improvements of P_m/P_m^0 for L_O=12.5 mm. Actually, the deviations found within for this L_O value were: 20.14, and 37.18% for t_s^o under estimations of 25, and 50%, respectively. The presented deviations for the lowest L_O value show a nearly proportional percentile variation of P_m/P_m^0 with t_s^0 (either for positive or negative variations). By increasing L_O, P_m deviations become constant, attaining the average value of 4.63, and 7.47% (for L_O=25, 37.5 and 50 mm) for t_s^0 over estimation of 25, and 50%. The behaviour as some similarities to that observed for the adhesive Araldite® AV138, although the P_m variations are higher. Moreover the increase of t_s^0 has a higher effect for short overlaps due to the ductility of this adhesive.

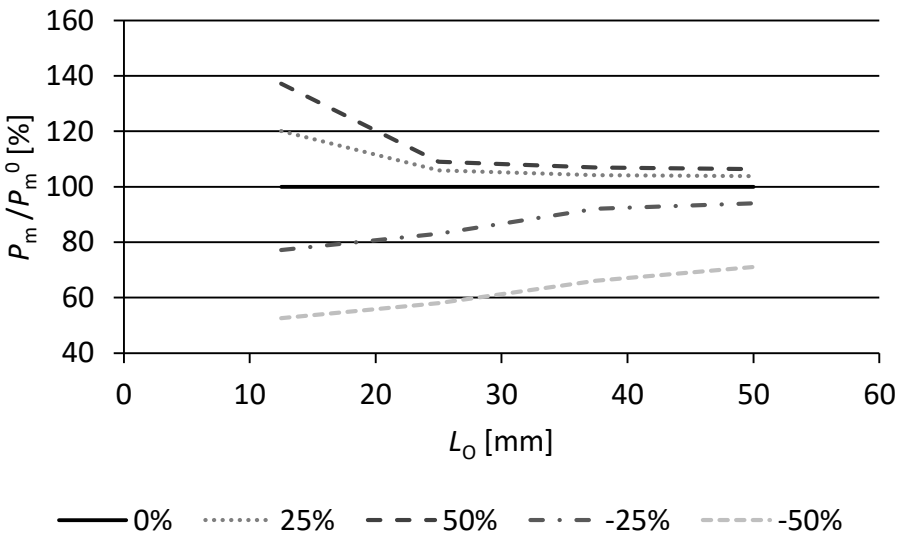

Figure 95 – Percentile variation of P_m/P_m^0 with t_s^0 values ranging from -50 to +50% of the initial ones in adhesive Araldite® 2015

The G_{IIC} influence on P_m/P_m^0, presented in Figure 96, is similar to the one caused by G_{IC} (Figure 94), although with smaller relative deviations. For L_O=12.5 mm, the effect is close to null. Positive percentile variations of G_{IIC} makes a lower impact on P_m than the negative ones. Indeed, not taking into account the lowest L_O value, increasing G_{IIC} by 25 and 50% of the initial one result in an average P_m improvement of 1.09, and 1.85%. Under estimating G_{IIC} by 25% manages to attain identical relative deviations as the ones caused thru the 50% G_{IIC} increasing (-1.73%). The effect of G_{IIC} 50% under estimation on P_m/P_m^0, besides being low, is variation that attains high deviations: -4.37, -5.09-6.61% for L_O=25, 37.5, and 50 mm respectively. The effect of the variations of G_{IIC} is proximal to that of the Araldite® AV138 although with smaller variations of P_m since, due to the higher ductility of this adhesive, the respective joints are less affected by the energetic parameters.

The values shown in Table 23, were used to evaluate how the variation of the cohesive parameters (all at the same time) influences the joint strength. Figure 97 reports the combined influence of (t_n^0, t_s^0, G_{IC}, G_{IIC}, E, and G) percentile variations on P_m/P_m^0 with the adhesive Araldite® 2015.

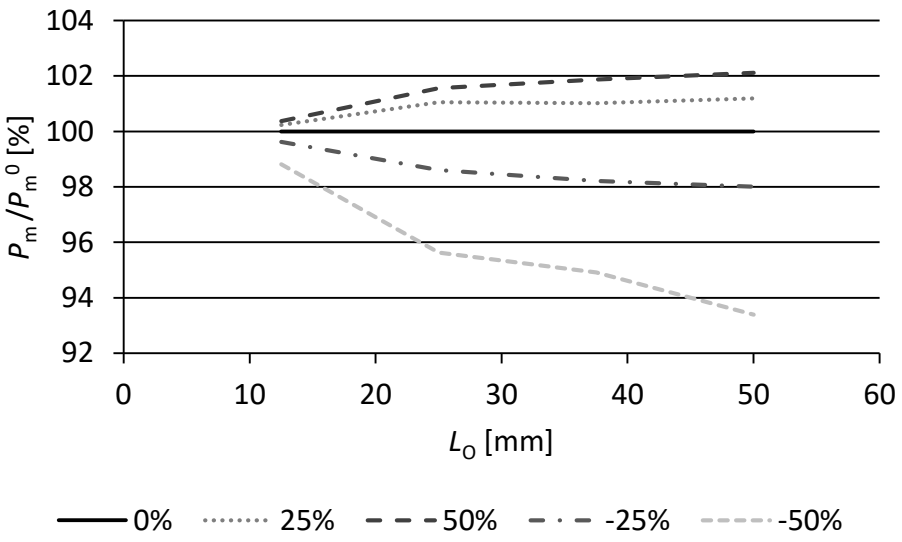

Figure 96 – Percentile variation of P_m/P_m^0 with G_{IIC} values ranging from -50 to +50% of the initial ones in adhesive Araldite® 2015

Table 23 – Percentile variation of all cohesive parameters plus *E* and *G* for the adhesive Araldite® 2015

%	25	50	-25	-50
t_n^0 [MPa]	27.038	32.445	16.223	10.815
t_s^0 [MPa]	22.375	26.850	13.425	8.950
G_{IC} [N/mm]	0.538	0.645	0.323	0.215
G_{IIC} [N/mm]	5.875	7.050	3.525	2.350
E [MPa]	2312.5	2775	1387.5	925
G [N/mm]	0.7	0.84	0.42	0.28

Results depicted in Figure 97, show similarity with the ones presented in Figure 95, due to the higher strength influence that t_s^0 manages. The P_m/P_m^0 relationship is nearly proportional for L_O=12.5 mm, and typically linear for L_O=25 up to 50 mm. Actually for the shorter L_O, the percentile variation of the cohesive elements attains a strength variation almost equal: when the cohesive values were under estimated by 25, and 50%, the strength diminished 23.73, and 48.25%, and when a 25, and 50% over estimation was used, strength raise 23.05, and 45.34% respectively. Following the tendency (of t_s^0 influence), the linear behaviour that starts for L_O=25 up to 50 mm, was more uniform with the over estimation of the cohesive elements. An average deviation of 13.88, and 25.35% was accomplished by percentile variations of 25, and 50% in that order. Under estimating the cohesive parameters by 25%, P_m was diminished by, 20.95, 17.00, and 15.86%, while by decreasing 50%, P_m decay by 45.28, 39.15, and 37.05% for L_O=25, 37.5, and 50 mm, respectively.

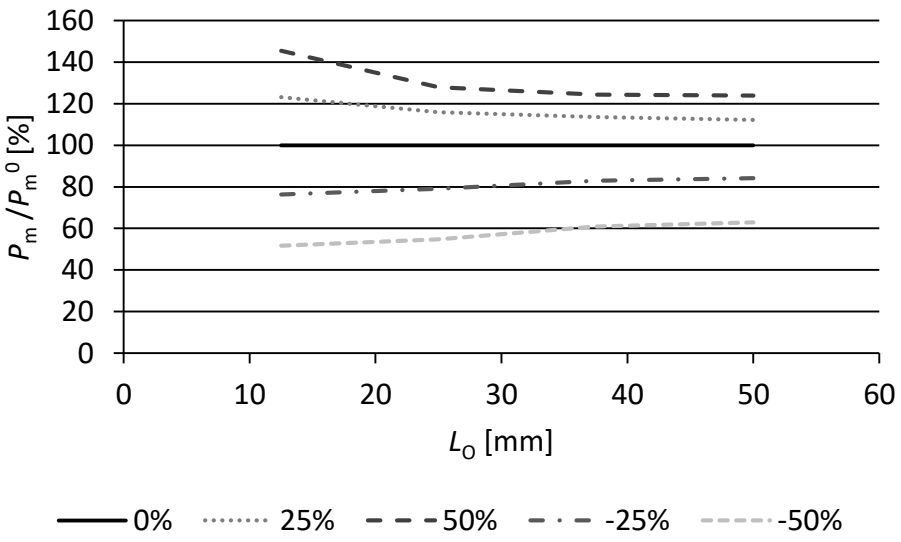

Figure 97 – Percentile variation of P_m/P_m^0 with different values of all cohesive parameters plus E and G ranging from -50 to +50% of the initial ones in adhesive in adhesive Araldite® 2015

The percentile variation of t_n^0 and G_{IC} of the initial ones are presented in Table 24. Figure 98, and Figure 99 depict the performed influence strength analysis for the adhesive Sikaforce® 7752.

Table 24 – Percentile variation of t_n^0 and G_{IC} values for the adhesive Sikaforce® 7752

%	25	50	-25	-50
t_n^0 [MPa]	14.3625	17.235	8.6175	5.745
G_{IC} [N/mm]	2.95	3.54	1.77	1.18

The influence that t_n^0 achieved on P_m/P_m^0, of a joint bonded with the adhesive Sikaforce® 7752 was nearly insignificant (Figure 98), with the exception of deviations attained for L_O=25 mm, or when a big t_n^0 reduction was estimated. In fact a 50% t_n^0 decrease, promotes deviations on P_m of -3.42, -8.09, -6.65, and -5.01%, while a 25% reduction, affects P_m by -0.96, -2.45, -2.08, and -1.59% for L_O=12.5, 25, 37.5, and 50 mm. t_n^0 over estimations manage even minor influence on P_m/P_m^0. The only noteworthy variations were found for L_O=25 mm (1.51, and 2.16%), attained by the increase of t_s^0 by 25, and 50% respectively.

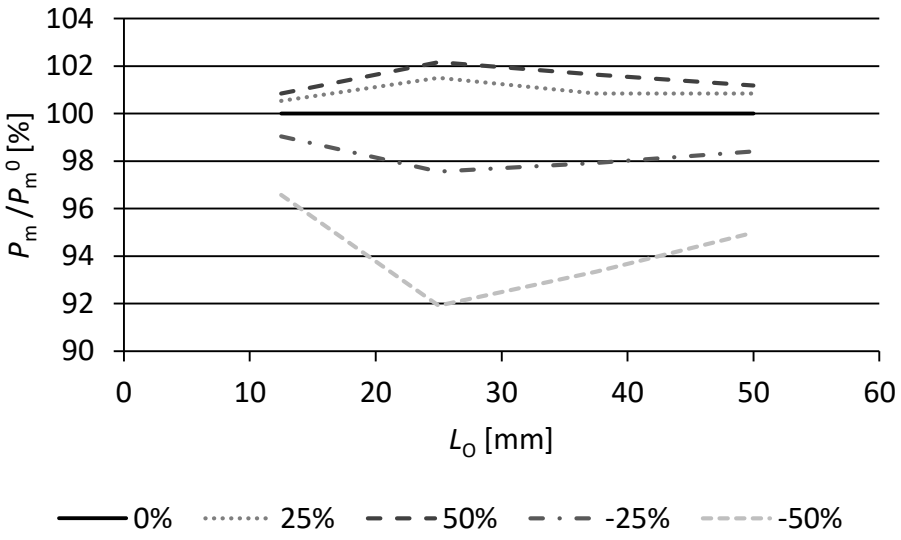

Figure 98 – Percentile variation of P_m/P_m^0 with t_n^0 values ranging from -50 to +50% of the initial ones in adhesive Sikaforce® 7752

Figure 99, related to G_{IC} influence on P_m/P_m^0 for the adhesive Sikaforce® 7752, shows great similarity with the one for the Araldite® 2015. However, inferior P_m deviations were accomplished. The maximum relative deviation was 0.50%, proficient thru a G_{IC} under prediction of 50% for L_O=37.5 mm. Analysing the remain L_O values, the maximum relative P_m deviations caused by G_{IC} percentile variations were: 0.01% (values ranging from -25 to 50%) for L_O=12.5 mm, 0.19% for L_O=25 mm, and 0.40% for L_O=50 mm (G_{IC} decreased by 50%). Raised G_{IC} values manages lesser strength influence than the lowers ones. This difference is related to the sole attainment of large δ_n values bigger than δ_n^f for the initial parameters at the overlap edges.

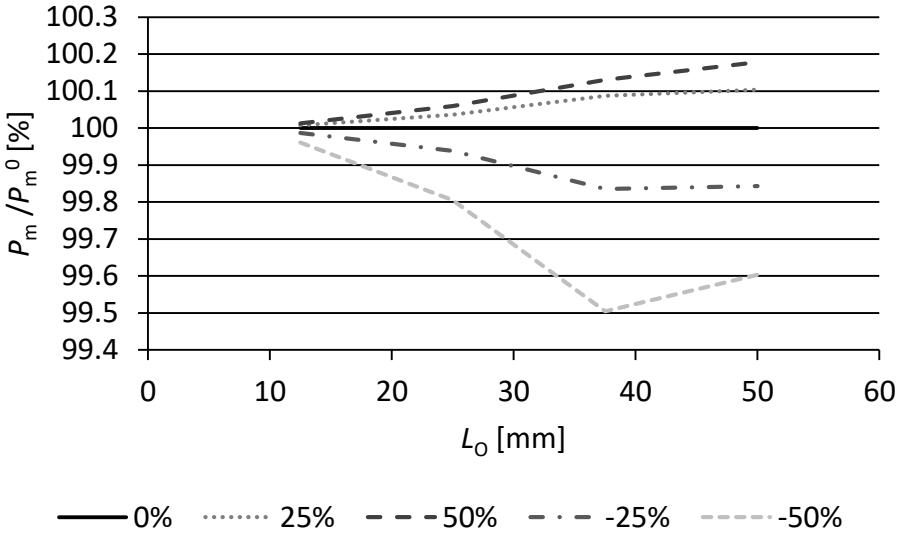

Figure 99 – Percentile variation of P_m/P_m^0 with G_{IC} values ranging from -50 to +50% of the initial ones in adhesive Sikaforce® 7752

Table 25 reveals the values used to study the t_s^0, and the G_{IIC} influence on P_m/P_m^0. Figure 100, and Figure 101 present the influence performed with the adhesive Sikaforce® 7752.

Table 25 – Percentile variation of t_s^0 and G_{IIC} values for the adhesive Sikaforce® 7752

%	25	50	-25	-50
t_s^0 [MPa]	12.7125	15.255	7.6275	5.085
G_{IIC} [N/mm]	6.7625	8.115	4.0575	2.705

As depicted thru Figure 100, t_s^0 imposes high strength influence in a joint bonded with the adhesive Sikaforce® 7752. For both, t_s^0 increase or decrease, P_m/P_m^0 relationship is nearly proportional within all L_O values. A tiny larger P_m influence was manage with t_s^0 under estimations. By comparison, P_m average deviations were 44.00, -48.54% (for 50, and -50% t_s^0 variation), 22.64, and -23.76% (for 25, and -25% t_s^0 variation of the initial one).

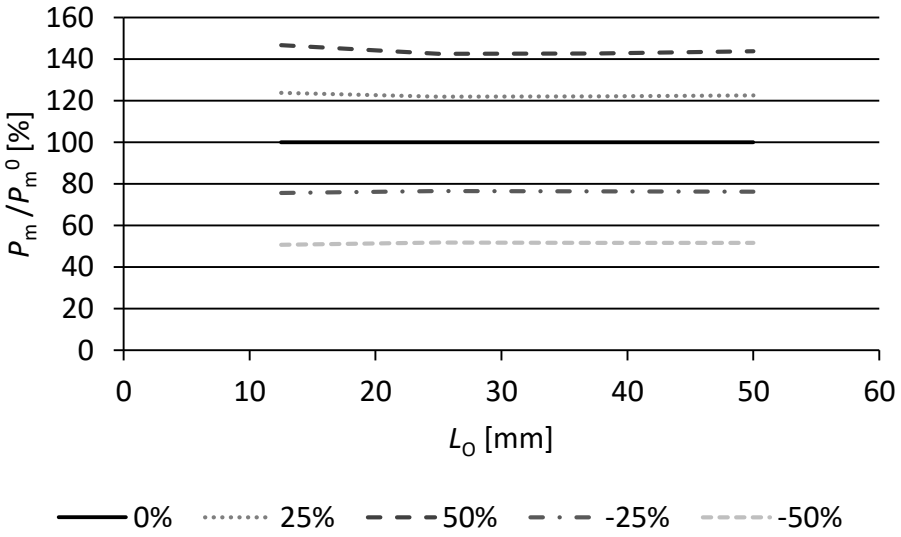

Figure 100 – Percentile variation of P_m/P_m^0 with t_s^0 values ranging from -50 to +50% of the initial ones in adhesive Sikaforce® 7752

Plots presented in Figure 101, related to G_{IIC}, reveals also a low influence in the joint strength Actually the maximum relative deviation was 2.24% found for L_O=50 mm under estimating G_{IIC} by 50%. As a matter of fact, the only P_m variation that occurred above one percent was for L_O=37.5 mm, by -1.60%, under the same G_{IIC} under estimated value.

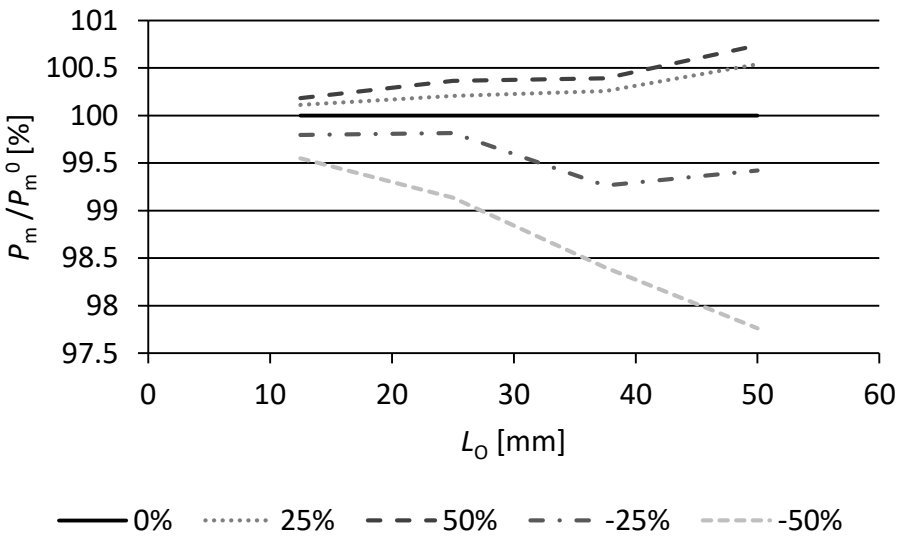

Figure 101 – Percentile variation of P_m/P_m^0 with G_{IIC} values ranging from -50 to +50% of the initial ones in adhesive Sikaforce® 7752

Table 26 shows the values of the cohesive parameters obtained thru percentile variation used to perform their influence on P_m for a joint bonded with the adhesive Sikaforce® 7752. Forward, Figure 102 presents the reported evaluation.

Table 26 – Percentile variation of all cohesive parameters plus *E* and *G* for the adhesive Sikaforce® 7752

%	25	50	-25	-50
t_n^0 [MPa]	14.3625	17.235	8.6175	5.745
t_s^0 [MPa]	12.7125	15.255	7.6275	5.085
G_{IC} [N/mm]	2.95	3.54	1.77	1.18
G_{IIC} [N/mm]	6.7625	8.115	4.0575	2.705
E [MPa]	617.2625	740.715	370.3575	246.905
G [N/mm]	234.6875	281.625	140.8125	93.875

The evaluation depicted on Figure 102 shows huge P_m influence, caused either by under as by over estimations of the cohesive parameters. Following the tendency and, as expected, great similarity with the t_s^0 effect on P_m/P_m^0 (Figure 100), due to its high strength influence for this adhesive. An even more P_m/P_m^0 linear behaviour with L_O was obtained. The simultaneous variation provide values of P_m/P_m^0 in close proportion with the parameters percentile variation. Actually, average deviations were 24.53, 49.02, -24.57, and -49.42%.

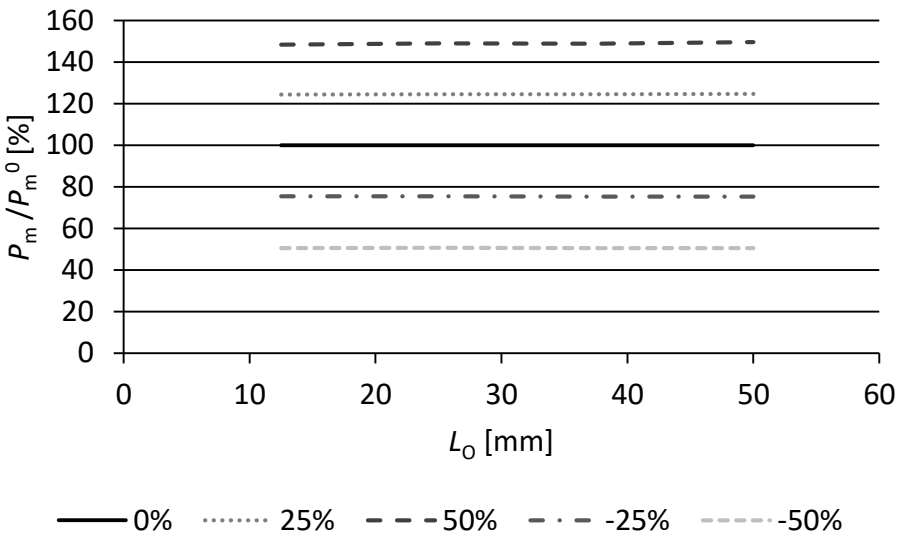

Figure 102 – Percentile variation of P_m/P_m^0 with different values of all cohesive parameters plus *E* and *G* ranging from -50 to +50% of the initial ones in adhesive in adhesive Sikaforce® 7752

3.2.5.5 Damage initiation criterion

The present subsection evaluates different damage initiation criteria (stress and strain-based) to predict joint strength of the joints bonded with the three adhesives. First the evaluation of damage stress-based initiation criteria was accessed by comparison between the experimental data, the strength prediction regarding maximum stress criterion (MAXS), the prediction performed in section 3.2.4 (QUADS), and MAXPS. Figure 103, Figure 104, and Figure 105 show the comparative results for the adhesive Araldite® AV138, Araldite® 2015, and Sikaforce® 7752, respectively.

The results for the adhesive Araldite® AV138 (Figure 103) show close results to the experimental ones for the MAXS and QUADS criteria, contrarily to MAXPS, which attains a large deviation to the experiments. Actually, the MAXPS criterion gives identical P_m values irrespectively of L_O, since failure took place by tensile net failure of the adherends. In fact, the initiation criterion MAXPS is not met prior to failure in the adherends. Between the other two criteria, the QUADS criterion gives more accurate results compared to the experimental data (maximum deviation of 16.86% for the MAXS and 11.76% for the QUADS, both considering L_O=50 mm). In fact, by comparing both criteria, the MAXS P_m estimation gives results higher by 9.39, 7.95, 3.95 and 4.56% for L_O=12.5, 25, 37.5, and 50 mm, respectively.

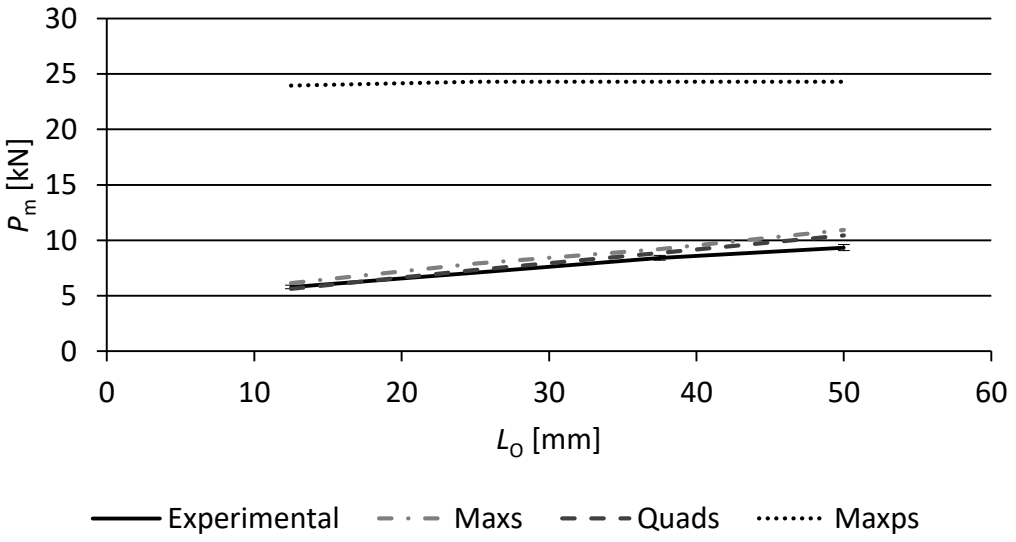

Figure 103 – Comparison between the experimental data and different damage initiation stress criteria for the joints bonded with the adhesive Araldite® AV138

Figure 104, related to the Araldite® 2015, presents once more closer results for the MAXS and QUADS criteria. With the MAXPS criterion failure took place by tensile net failure of the adherends, thus, won't be referred again in this comparison. For the presented adhesive, QUADS was the criteria which better estimations achieved, however, with small deviations than the previous evaluation. The maximum error regarding the experimental data was 8.84% (MAXS), and 7.97% (QUADS) for L_O=50 mm. Deviations regarding only both damage initiation criteria were: 5.16, 3.74, 2.26, and 0.80% for L_O=12.5, 25, 37.5, and 50 mm, respectively.

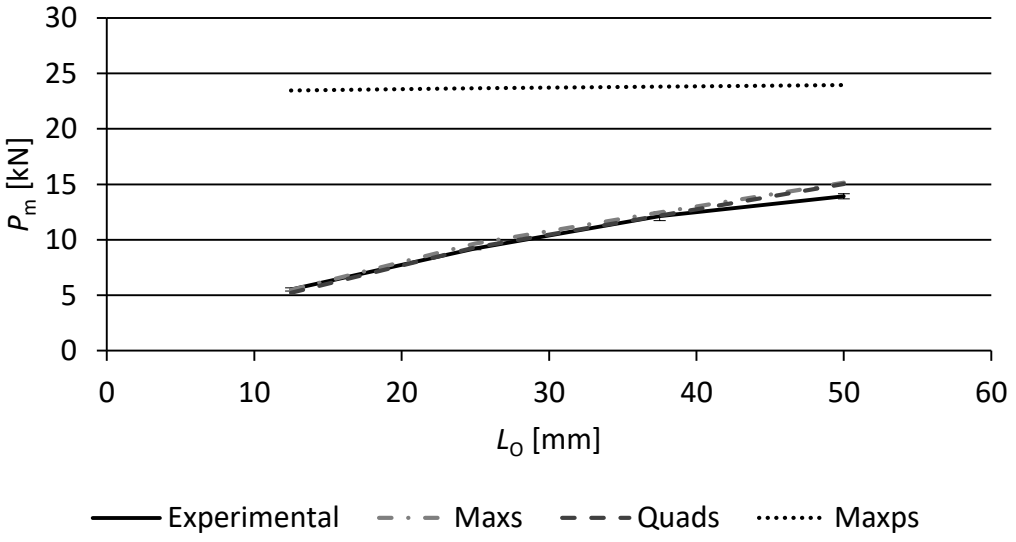

Figure 104 – Comparison between the experimental data and different damage initiation stress criteria for the joints bonded with the adhesive Araldite ® 2015

The strength prediction preformed for the adhesive Sikaforce® 7752 shows, by comparison with the experimental data, that the MAXS and QUADS criteria give P_m under predicted results. The MAXPS criterion revealed, once more, to be a poor choice for P_m prediction because failure took place by tensile net failure of the adherends. However, evaluation data places the MAXS criterion as the best choice to perform P_m estimation for the joints bonded with this adhesive. As a matter of fact, smaller under predictions were attained for all L_O values: -15.73, -9.26, -9.57, and -9.27% for L_O=12.5, 25, 37.5, and 50 mm respectively. The maximum relative deviations were 17.07% (QUADS), and 15.73% (MAXS) found for L_O=12.5 mm. Relating MAXS with QUADS, the deviations from L_O=12.5 to 50 mm were 1.61, 4.18, 3.03, and 2.34%.

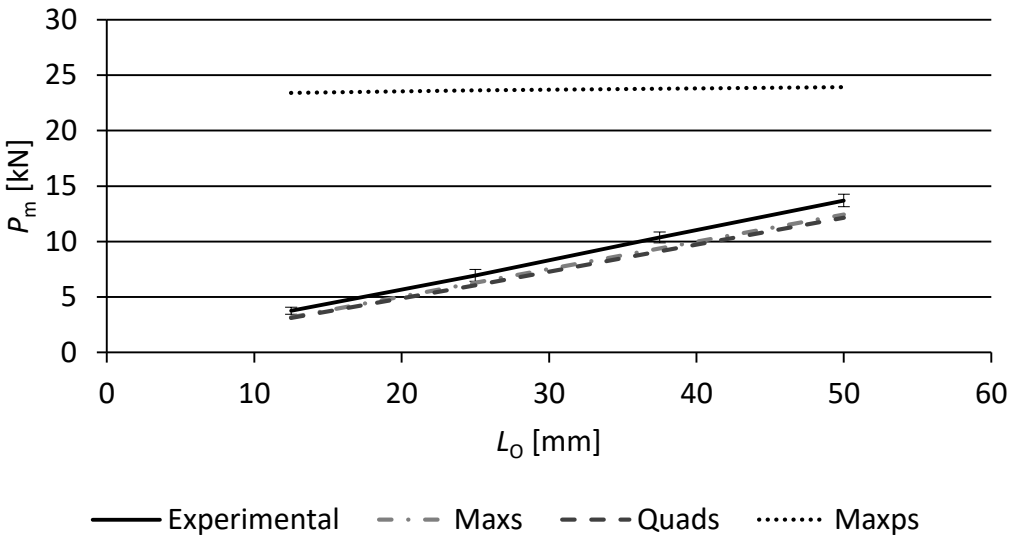

Figure 105 – Comparison between the experimental data and different damage initiation stress criteria for the joints bonded with the adhesive Sikaforce® 7752

The evaluation of the strain-based initiation criteria was carried out by comparison between the experimental data, the MAXE, the QUADE and the MAXPE criteria. Figure 106, Figure 107, and Figure 108 present this evaluation for the adhesives Araldite® AV138, Araldite® 2015 and Sikaforce® 7752, respectively.

Regardless the adhesive used, strain-based initiation criteria are not suited to simulate damage initiation in the adhesive layer, since they all overshoot by a large amount the experimental results. In some joint configurations, damage initiated at a load close to the tensile net failure load of the adherends. In other configurations, the P_m corresponded to the adherends' tensile net failure.

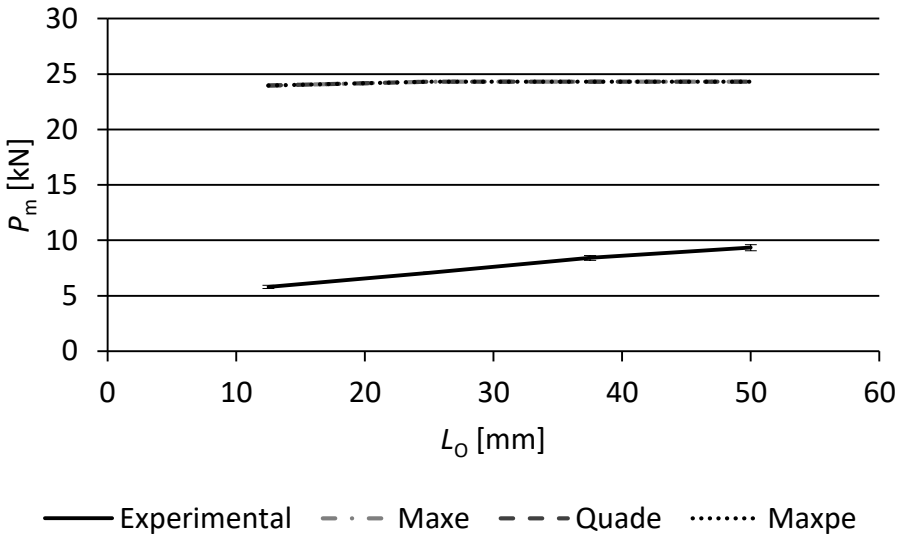

Figure 106 – Comparison between the experimental data and different damage initiation strain criteria for the joints bonded with the adhesive Araldite® AV138

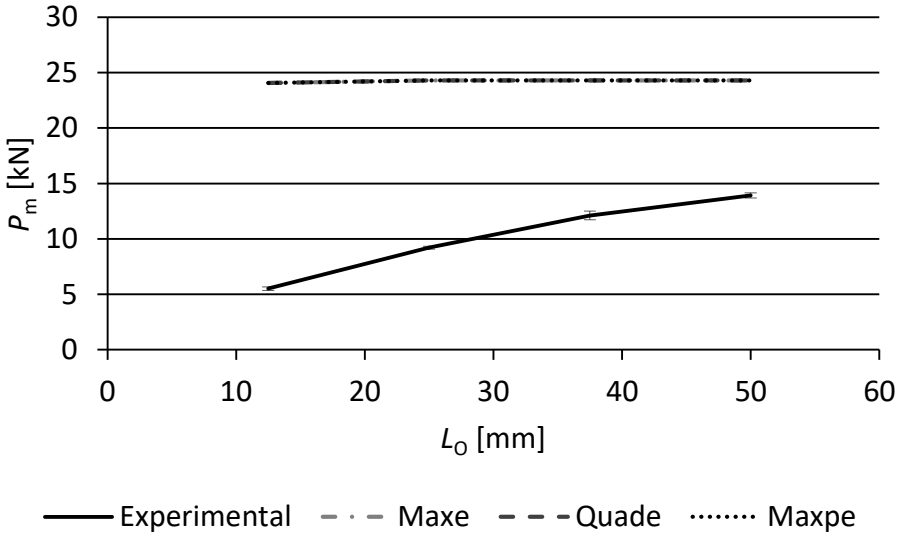

Figure 107 – Comparison between the experimental data and different damage initiation strain criteria for the joints bonded with the adhesive Araldite ® 2015

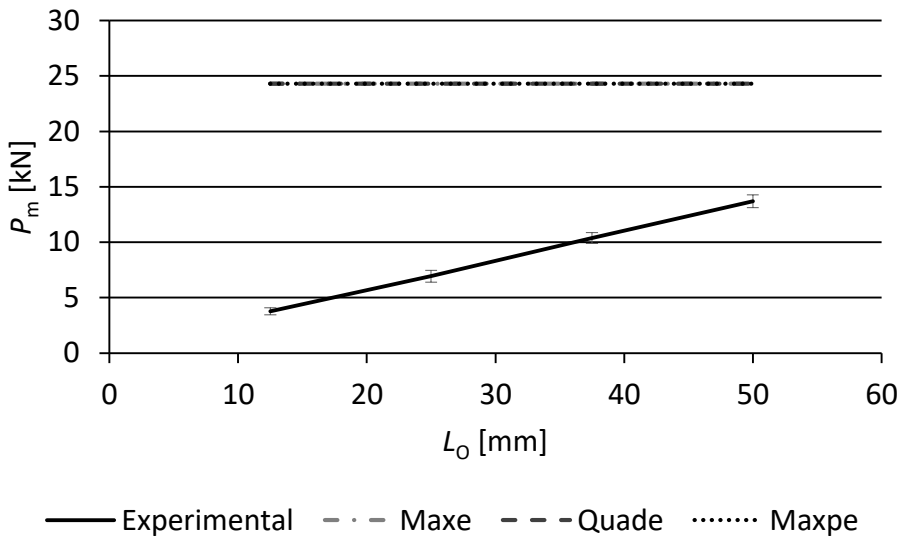

Figure 108 – Comparison between the experimental data and different damage initiation strain criteria for the joints bonded with the adhesive Sikaforce® 7752

3.2.5.6 Damage growth criterion

This subsection addresses the accuracy of the power law and the BK [60] growth criteria for the P_m prediction of the three adhesives. The power law evaluation was firstly performed by varying the power parameter, α (equation(9)), considering values 0.5, 1, 1.5, and 2, for further comparison with the experimental data. The results are presented in Figure 109, Figure 110, and Figure 111 for the adhesive Araldite® AV138, Araldite® 2015, and Sikaforce® 7752, respectively. The Power 1 data is identical to that presented in Section 3.2.4.

Figure 109, related to the adhesive Araldite® AV138, reports that the Power 0.5 suits best for P_m prediction of this adhesive. Actually an average deviation of 4.89% was achieved by Power 0.5 for all L_O values, followed by Power 1, with an average difference of 5.89%. Power 1.5 over predicts P_m by the average value of 16.17%, while Power 2 gives the worst P_m predictions by clearly overshooting the experimental results with an average deviation of 21.65%. As L_O increases, deviations also grow, regardless the value of the power parameter.

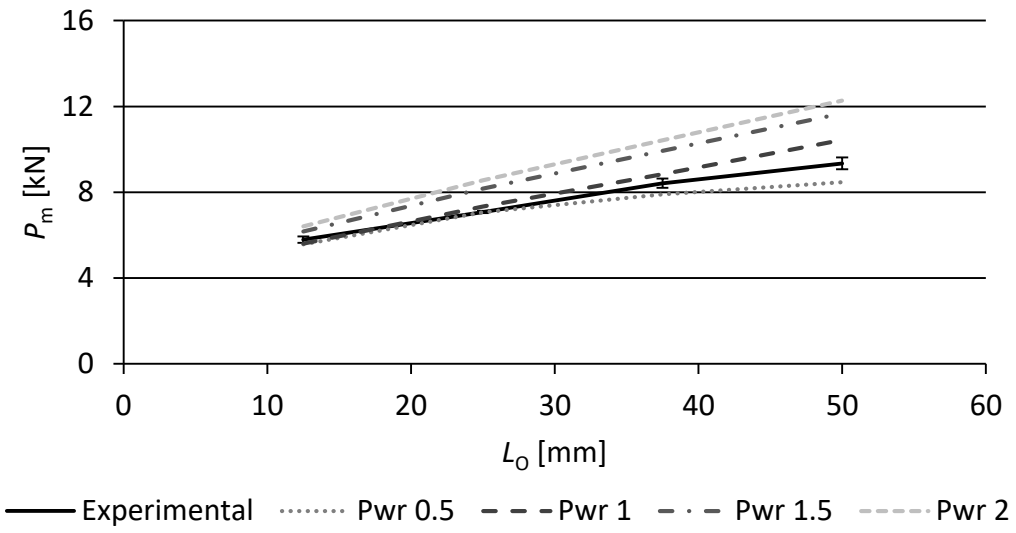

Figure 109 – Comparison between different parameter values of the power law grow criteria for P_m prediction for the joints bonded with the adhesive Araldite® AV138

The comparison shown in Figure 110 reveals Power 1 as the best power parameter for strength prediction of the joints bonded with the adhesive Araldite® 2015. Indeed, the deviations found with Power 1 were: -5.55, 1.18, 0.49, and 7.97% for L_O=12.5, 25, 37.5, and 50 mm, in that order, resulting in an average error of 3.79%. Power 1.5 and Power 2 predicted P_m with an average deviation of 6.56 and 7.29%, respectively. The Power 0.5 criterion, which was the best choice for the strength prediction of the previous adhesive, presents now the worst P_m estimation, with an average under estimation of 15.00%. The increase of L_O promotes the rise of relative deviations, by comparison with the experimental data, equally to what was observed for the Araldite® AV138.

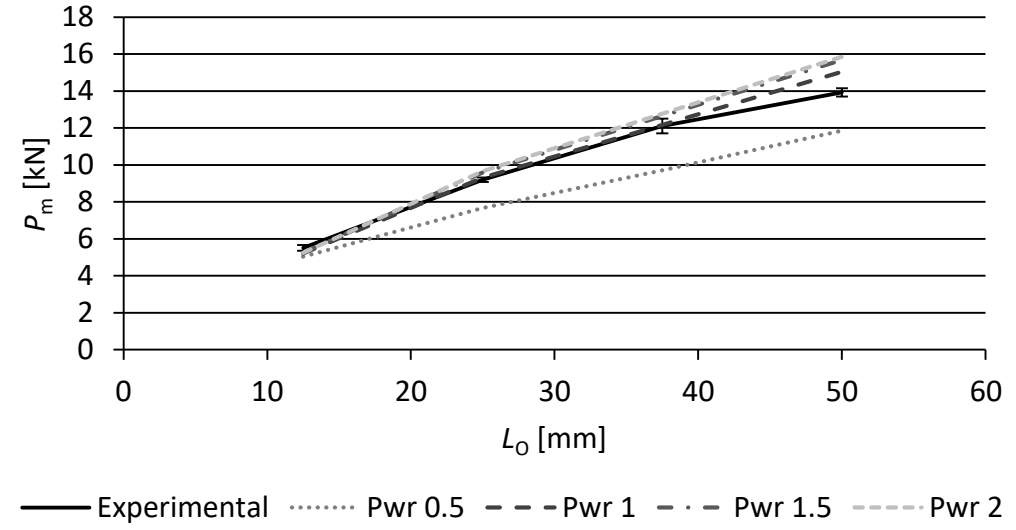

Figure 110 – Comparison between different parameter values of the power law grow criteria for P_m prediction for the joints bonded with the adhesive Araldite ® 2015

The evaluation depicted in Figure 111, comparing different parameters of the power law criterion for the adhesive Sikaforce® 7752, provides identical P_m under estimation values, whatsoever were the chosen α or L_O values. Actually, the average deviations were: 14.2, 13.4, 13.2, and 13.2% for α=0.5, 1, 1.5, and 2, respectively. Oppositely to the tendencies observed with the other adhesives, the increase of L_O promoted a reduction in the relative P_m deviations, although this reduction is only marginal.

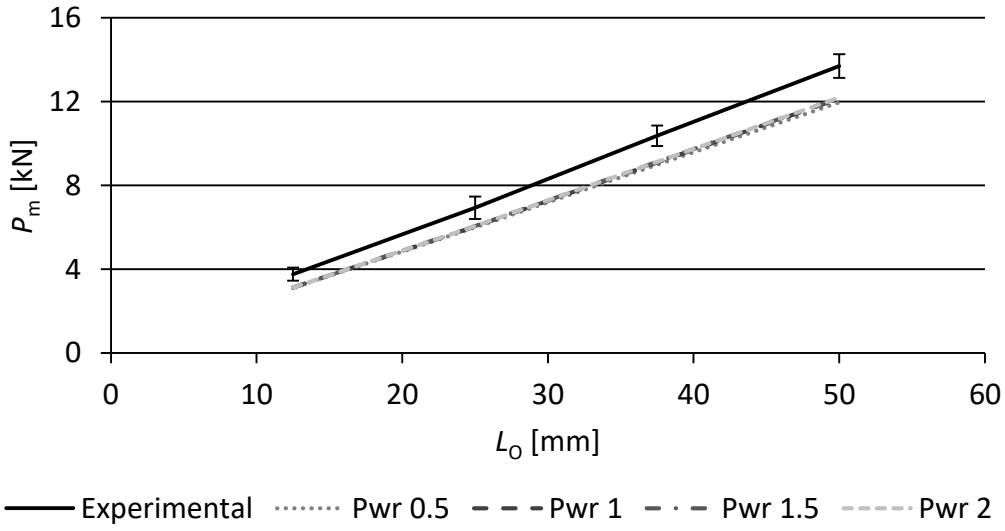

Figure 111 – Comparison between different parameter values of the power law grow criteria for P_m prediction for the joints bonded with the adhesive Sikaforce® 7752

The evaluation of the BK growth criteria for P_m prediction was performed by its comparison with the Power law criterion (with α=1), and the experimental data. For the characteristic parameter η (equation(10)), the values 0.5, 1, and 2.5 were used. The comparison is shown in Figure 112, Figure 113 and Figure 114 for P_m prediction for the adhesives Araldite® AV138, Araldite® 2015, and Sikaforce® 7752, respectively.

Figure 112 shows that the criterion which provides the most accurate strength prediction for the adhesive Araldite® AV138 was BK 2.5, with an average deviation of 4.11%, nearly to the one obtained with Power 1 (4.30%). Nonetheless, a more detailed analysis reveals P_m under estimations for the lower L_O values: -7.47, and -1.33% for L_O=12.5, and 25 mm, and P_m over estimations for higher L_O values: 0.58, and 7.05% for L_O=37.5, and 50 mm, respectively.

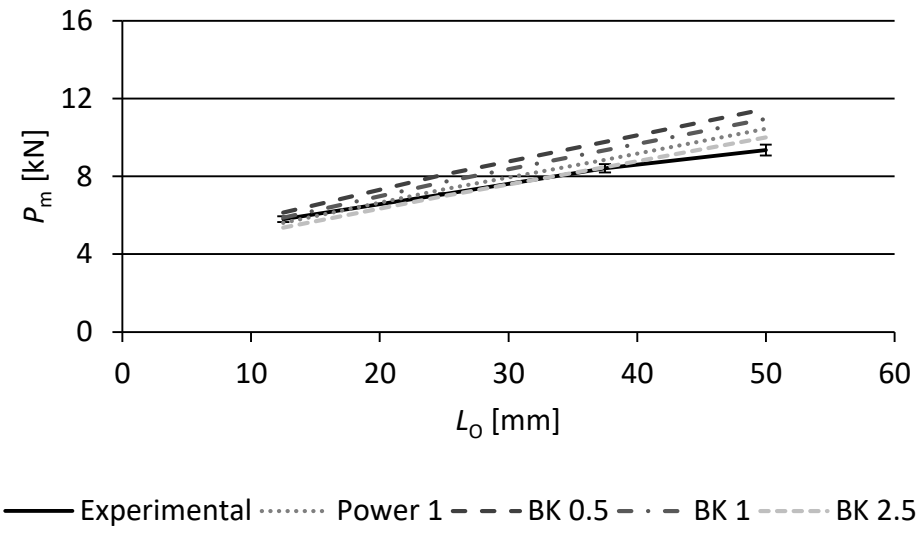

Figure 112 – Comparison between power law and Benzeggagh-Kenane growth criteria for P_m prediction for the joints bonded with the adhesive Araldite® AV138

In Figure 113, related to the adhesive Araldite® 2015, it is shown that the BK criterion under predicts P_m for the lowest L_O value, by an average error of 4.30% for the three values of η. Oppositely, for higher L_O, big deviations by excess were found: P_m was over predicted by values up to 48.26% (η=0.5), 47.20% (η=1), and 16.70% (η=2.5), attained with L_O=50 mm. Due to those deviations, the power law criteria gives the most accurate P_m predictions for this adhesive.

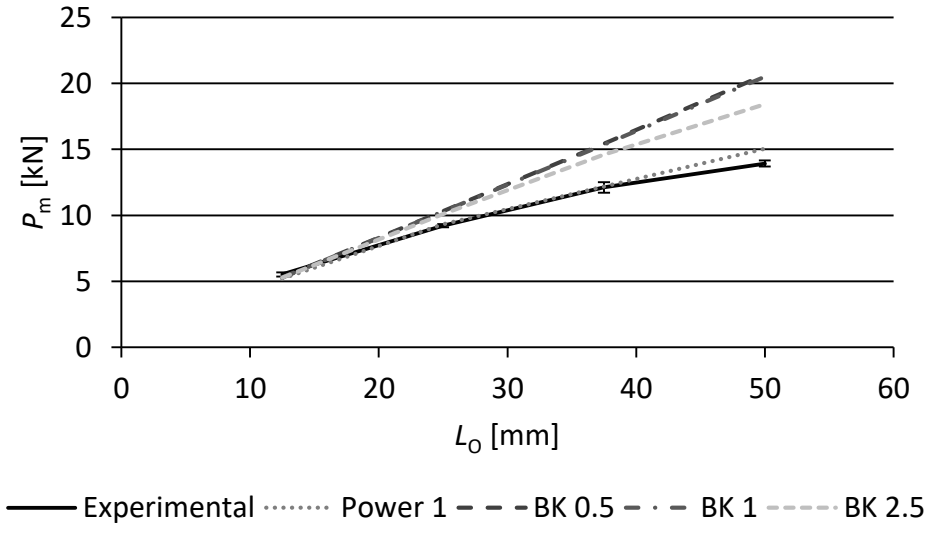

Figure 113 – Comparison between power law and BK growth criteria for P_m prediction for the joints bonded with the adhesive Araldite ® 2015

The comparison depicted in Figure 114, regarding the evaluation of the damage growth criteria for the adhesive Sikaforce® 7752, shows that all criteria underestimate P_m, with

very similar average deviations of -17.07, -12.89, -12.18, and -11.28% for L_O=12.5, 25, 37.5, and 50 mm, respectively.

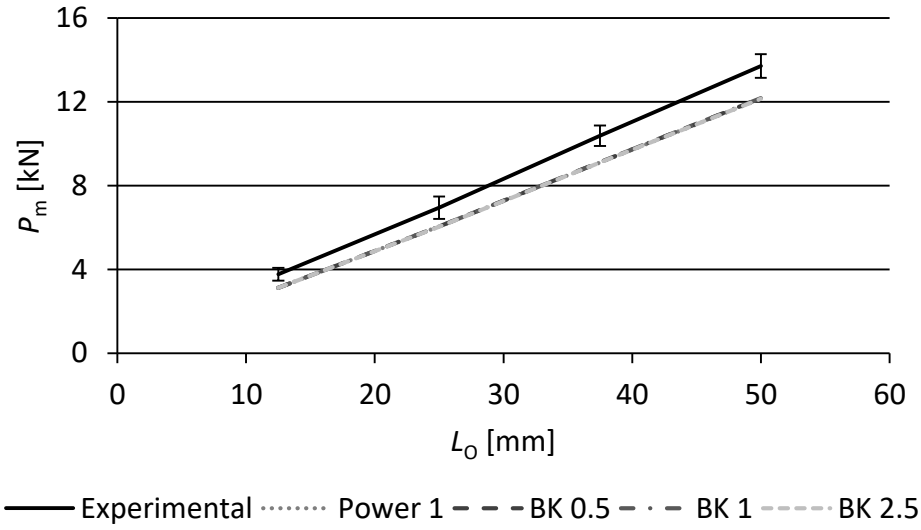

Figure 114 – Comparison between power law and BK growth criteria for P_m prediction for the joints bonded with the adhesive Sikaforce® 7752

3.2.5.7 Analysis of the obtained results

This Section discusses in detail the influence of different simulation conditions on the CZM numerical analysis of the joints bonded with the three adhesives.

Concerning the percentile variation of the elastic stiffness, the only noteworthy impact on P_m was found for the adhesive Araldite® AV138, with E and G values reduced by 50%. Indeed, this stiffness reduction leads to more uniform stress fields along the bonded joint of a brittle adhesive (diminishing peak stresses), which attain failure when the limit strength is reached anywhere in the joints. Therefore, the joint strength increases. Regarding the other two adhesives, due to their plasticization ability when the peak strengths are attained, the respective joints become less affected by the stiffness variations.

Decoupling the loading modes shows P_m under predictions notwithstanding the adhesive and L_O value. However, the simulation for the adhesive Araldite® AV138 was the one that presented lower deviations compared with the experimental data (average under prediction by 6.67%). On the other hand, decoupling the loading modes in the triangular CZM for ductile adhesives revealed to be an unwise simulation option.

The evaluation of the three different CZM laws, by considering uncoupled modes, presented for the adhesive Araldite® AV138 a good correlation with the experimental data by using triangular and trapezoidal laws, while the P_m values given by the exponential law deviate from the experimental ones by 10.03% (average for all L_O

values). On the other hand, the simulation for the ductile adhesives showed significant P_m under predictions, regardless the CZM law or L_O value.

The influence of varying the cohesive parameters for the adhesive Araldite® AV138 showed that the strength of this adhesive is highly sensitive to the percentile variation of the fracture parameters (G_{IC} and G_{IIC}), as well as the cohesive strength parameter t_s^0, when it is decreased by 50%. G_{IC} is the parameter that affects the most P_m, attaining average deviations of -16.78% for a reduction of this parameter by 50%. The simulation performed with the percentile variation of all cohesive parameters plus E and G presents, as expected, plots similar to those of G_{IC}, yet attaining higher P_m deviations. The evaluation for the adhesive Araldite® 2015 reveals that only G_{IC} and t_s^0 promote a significant influence on the joint strength, except for the lowest L_O. Indeed, regarding the fracture toughness parameters, the negative variation of G_{IC} accomplished higher P_m impact (-23.77% for L_O=50 mm). For the cohesive strength parameters, t_s^0 managed P_m variations that decreased for higher L_O values, attaining the maximum P_m under prediction (-47.37%) for L_O=12.5 mm with t_s^0 diminished by 50%. The analysis of percentile variation of all cohesive parameters (plus E and G) at the same time, for the adhesive Araldite® 2015, showed that the overall results were affected in a similar manner to the sole variation of t_s^0, although with bigger percentile deviations. Relating to the adhesive Sikaforce® 7752, the only parameter whose percentile variations of P_m were significant was t_s^0. Actually, a nearly proportional increase and reduction of P_m with the respective variation of t_s^0 was attained, notwithstanding the value of L_O. The study performed with percentile variations of all cohesive parameters (plus E and G) follows the tendency of the variation of t_s^0.

The analysis of the damage initiation criteria draws attention to the results obtained for the MAXPS and all strain-based criteria, which attained large P_m deviations. Indeed, irrespectively of the adhesive type and L_O, failure took place by tensile net failure of the adherends. Regarding the adhesive Araldite® AV138 simulation with the QUADS criterion, it presented the best P_m accuracy, yet with increased deviations for higher L_O values. The evaluation performed with the adhesive Araldite® 2015 also provided good results and, identically to the previous adhesive, the QUADS criterion attained the closest values to the ones of the experimental work. The higher P_m deviation for this criterion was found for L_O=50 mm (7.97%). The analysis for the adhesive Sikaforce® 7752 reveals P_m under predictions for both MAXS and QUADS criteria. However, for this high ductile adhesive, the best P_m estimations were given by the MAXS criterion, yet with low difference to the values attained with the QUADS criterion.

Evaluation of the power law and the BK growth criteria presented different behaviours for each adhesive. For the adhesive Araldite® AV138, the power law criterion with α=0.5 attains P_m values close to the experimental data, yet with a higher deviation for bigger L_O values. The BK criterion suits best with η=2.5 (average deviation of 4.11% for all L_O values). However, P_m was under predicted by 7.47% for L_O=12.5 mm and over predicted by 7.05 for L_O=50 mm. Analysis of the power law criterion for the adhesive Araldite®

2015 showed that, with α=1, P_m was more accurately estimated than with the other parameter values. The BK criterion reveals to be incompatible for strength prediction of ductile adhesives. Despite the fact that, for the shortest L_O, P_m was under predicted by the average of 4.30%, for η=0.5, 1 and 2.5, the L_O increase promoted large P_m under estimations (up to 48.26%). For the adhesive Sikaforce® 7752 the evaluation of both damage growth criteria showed P_m under prediction with an average value of ≈13%, even considering different α and η parameters, which indicates that this high ductile adhesive should be analysed with another CZM law shape.

CONCLUSIONS

4 CONCLUSIONS

The main purpose of this thesis was to evaluate different simulation conditions in the CZM analysis for an accurate strength prediction of a thin adhesive layer in SLJ, after validation of the methodology with experiments. Different L_O values and CZM features were considered: the elastic stiffness of the cohesive law, the decoupling of the loading modes, the evaluation of different law shapes, the percentile variation of the cohesive parameters and the assessment of different initiation and propagation criteria. This study is highly important and essential for the complete understanding of these affects and the correct application of this method. With this purpose, an aluminium alloy (AW6082-T651) was bonded using three different adhesives: the brittle adhesive Araldite® AV138, the moderately ductile adhesive Araldite® 2015 and the ductile Sikaforce® 7752.

After a detailed description of the experimental tests, the raw data was treated and analysed, and it was concluded that P_m results are highly influenced by L_O and the adhesives' mechanical properties. The brittle adhesive Araldite® AV138 attained the worst P_m improvement with the increase of L_O, for the three adhesives. Actually, 61.26% was the percentile P_m improvement that the Araldite® AV138 was capable to accomplish with L_O from 12.5 to 50 mm. On the other hand, the ductile adhesives Araldite® 2015 and Sikaforce® 7752 attained a P_m evolution by 152.29 and 263.99% between limit values of L_O, respectively. These different behaviours are manly justified by the adhesives' plasticization capability and their level of ductility. Indeed, a brittle adhesive does not allow plasticization neither redistribution of stresses in the bond line after the failure strength of the adhesive is attained at the overlap edges. Oppositely, the ductile adhesives permit plasticization and manage redistribution of loads when the limiting stresses are attained, making use of the less stressed parts of the overlap, therefore resulting in higher P_m values.

The numerical work performed with the software ABAQUS® began with the presentation of the simulations conditions, i.e., adhesives and adherends characterization, mesh design, the boundary conditions and the CZM formulation (mixed-mode triangular law, pure-mode triangular, trapezoidal and linear-exponential laws, damage initiation and growth criteria and the cohesive properties estimation). For a better understanding of the joints' behaviour, a stress analysis in the adhesive layer was initially performed. The parametric study on L_O showed for all adhesives that both σ_y and τ_{xy} stresses peak at the overlap edges and concentrated in smaller normalized regions with the increase of L_O. The adhesive Araldite® AV138 attained the highest peaks of σ_y and τ_{xy} stresses, due to higher stiffness, promoting therefore higher stress gradients, which resulted on reduced overall joint strength. On the other hand, the adhesive Sikaforce® 7752 presents, for all values of L_O, peak σ_y and τ_{xy} stresses of lower

magnitude than the adhesives Araldite® AV 138 and Araldite® 2015, mainly due to its flexibility. Moreover, owing to its plasticization ability, the adhesive layer was put under load gradually when the adhesive at the overlap edges started to plasticize. This promoted a significant improvement of P_m with the increase of L_O. The adhesive Araldite® 2015, due to its' moderate flexibility, presented intermediate gradients of σ_y and τ_{xy} stresses compared with the other two adhesives.

Strength prediction was then performed and further compared with experimental data, using the initial CZM conditions (triangular mixed-mode CZM law, QUADS and linear energetic criterion for damage initiation and damage growth, respectively). For the adhesives Araldite® AV138 and Araldite® 2015, the P_m prediction were very accurate, except for L_O=50 mm. Actually, P_m over predictions for the highest L_O were 11.76 and 7.97%, respectively. Regarding the brittle Araldite® AV138, which presented lack of plasticization at the overlap edges when P_m was attained, the triangular CZM law suited almost perfectly. The adhesive Araldite® 2015, ignoring its moderate ductility, followed the same tendency: the triangular CZM law still was able to accurately predict P_m. On the other hand, for the adhesive Sikaforce® 7752 P_m was under predicted by 13.39% (average for all L_O values), due to the large plasticity that this adhesive can endure, which is not correctly modelled by the triangular CZM.

The above mentioned strength prediction with the initial CZM conditions plus the data from the experimental tests, were used as comparative basis upon the different CZM simulation conditions, in order to fulfil the main purpose of this work. The conclusions for the different analyses were as follows:

- Variation on the elastic stiffness revealed to have lower P_m influence on the brittle adhesive Araldite® AV138 – only with a big stiffness reduction (by 50%) a noteworthy P_m over prediction (32.95%) occurred, found for L_O=37.5 mm. Such P_m improvement was due reduction of the peak stresses at the overlap edges, attained by the stiffness decrease. Regarding the ductile adhesives, results showed that the influence of the stiffness on P_m was smaller than for the previous adhesive. Indeed, the influence tends to diminish with the increase of ductility. The maximum deviations were -2.45 and -1.09% for the adhesives Araldite® 2015 and Sikaforce® 7752, respectively, attained with a stiffness reduction of 50%. Ductile adhesives undergo plasticization, therefore they are less dependent on the elastic stiffness of the adhesive.
- Decoupling the loading modes showed for the adhesive Araldite® AV138 P_m under predictions that decreased with the increase of L_O. Actually, P_m was deviated by -13.37 and 0.24% for L_O=12.5 and 50 mm, respectively. The analysis for the Araldite® 2015 presented higher P_m deviations – average of 31.96% for all L_O values. Regarding the adhesive Sikaforce® 7752, P_m was also under predicted, however, deviations by increasing L_O – P_m was deviated by -24.79 and -40.80% for L_O=12.5 and 50 mm, respectively. Comparing the results for the three

adhesives, one may conclude that ductile adhesives are more sensitive than the brittle ones to the decoupling of the loading modes.

- Simulations with different CZM law shapes revealed for the adhesive Araldite® AV138 that trapezoidal law was the one that suited best. It was expected that the triangular law would give the best results however, the small errors introduced by considering uncoupled modes explain why the trapezoidal law represented best the experimental data. The analysis outcome for both ductile adhesives, the Araldite® 2015 and the Sikaforce® 7752, showed poor results despite the used law shape. Actually, deviations ranged from -24.24 to -41.14%. These results confirm that ductile adhesives are more affected by the approximation of uncoupling both loading modes than brittle adhesives.
- The analysis of the influence of the cohesive parameters variation for the adhesive Araldite® AV138 showed that the noteworthy P_m deviations were attained with parameters decreased by 50%. Actually, with such percentile variation, G_{IC} promoted P_m under predictions by 16.78%, G_{IIC} by 18.99% and t_s^0 by 11.73% (average values for all L_O lengths). On the other hand, the influence of t_n^0 on P_m was almost nil. The outcome of the simulation performed with the variation of all parameters presented a similar influence to that observed for G_{IC}, which was the parameter that most affected P_m for this brittle adhesive. Analysis for the adhesive Araldite® 2015 revealed that the parameters that promoted significant P_m variations were: G_{IC} increased and decreased by 50%, attaining 15.97 and -23.77% variations, respectively, for L_O=50 mm; and t_s^0 either with negative or positive variations affected P_m by deviations that ranged from 37.18 to -47.13% (for t_s^0 variations of 50 and -50%, respectively), for the shortest L_O. The simultaneous variation of all parameters showed similar results to the sole variation of t_s^0, however with bigger percentile deviations. The study for the ductile adhesive Sikaforce® 7752 presented that the only parameter that really affects P_m was t_s^0, which attained a nearly proportional increase and reduction of P_m with the respective variation of this cohesive strength parameter. Since the other cohesive parameters were less influent on P_m for this adhesive, their simultaneous variation promoted a similar effect to the t_s^0 by itself.
- The different strain-based initiation damage criteria (MAXE, QUADE and MAXPE) showed that, notwithstanding the type of adhesive, all criteria provided large errors. As a matter of fact, the stress-based MAXPS criteria also attained large P_m deviations, and for those four cases, failure always took place by the tensile net failure of the adherends. Concerning now the other two stress-based criteria (QUADS and MAXS), the analysis for the adhesives Araldite® AV138 and Araldite® 2015 presented better accuracy with the QUADS criterion (average of 5.89% for the Araldite® AV138 and 3.79% for the adhesive Araldite® 2015). The results for the Sikaforce® 7752 were not satisfactory, yet the MAXS criterion presented the closer predictions.

- For the adhesive Araldite® AV38, results of the influence of the damage growth criteria on P_m showed that the criterion that suited best was the BK with η=2.5 (average error of 4.11%), despite for the limit L_O values, P_m had been wrongly estimated by ≈7.26%. P_m for moderate ductile adhesive Araldite® 2015 was best predicted by a Power law criterion with α=1 (average error of 3.79%), yet it also presented an average P_m deviation of 6.76% for the two limit L_O values. Regarding the strength prediction of the ductile adhesive Sikaforce® 7752, none of the tested criteria was able to accurately evaluate it. P_m was under predicted by an average of ≈13% for all simulations performed.

Upon those statements, it becomes easier to choose the best set of numerical conditions for an accurate strength prediction of an adhesively-bonded joints.

The following suggestions are proposed for future works:

- Evaluation of the strength prediction without decoupling the loading modes for the trapezoidal law;
- Perform the same verifications undertaken in this work with different joint designs: double lap, T-joints tubular, with and without reinforcements;
- Compare the obtained results with 3D simulations to evaluate any possible 3D effects on the stress distributions and the strength predictions;
- Analyse the performed simulation conditions concerning a different shape of the softening law, for instance, the trapezoidal one.

REFERENCES

5 REFERENCES

1. da Silva, L.F.M. and R.D.S.G. Campilho, *Advances in Numerical Modelling of Adhesive Joints*, in *Advances in Numerical Modeling of Adhesive Joints*. 2012, Springer Berlin Heidelberg. p. 1-93.
2. da Silva, J.F.M.G., A. Öchsner, and R.D. Adams, *Handbook of Adhesion Technology*. 2011, Heidelberg: Springer.
3. Fernandes, T.A.B., et al., *Adhesive Selection for Single Lap Bonded Joints: Experimentation and Advanced Techniques for Strength Prediction.* The Journal of Adhesion, 2015. **91**(10-11): p. 841-862.
4. May, M., H. Voß, and S. Hiermaier, *Predictive modeling of damage and failure in adhesively bonded metallic joints using cohesive interface elements.* International Journal of Adhesion and Adhesives, 2014. **49**: p. 7-17.
5. Neto, J.A.B.P., R.D.S.G. Campilho, and L.F.M. da Silva, *Parametric study of adhesive joints with composites.* International Journal of Adhesion and Adhesives, 2012. **37**: p. 96-101.
6. de Sousa, C.C.R.G., *Comparação de técnicas analíticas e numéricas para previsão da resistência de juntas adesivas de sobreposição simples*. 2016, Tese de Mestrado em Engenharia Mecânica - Ramo Construções Mecânicas. Instituto Superior de Engenharia do Porto: Porto.
7. Carvalho, U.T.F., *Modelação de juntas adesivas de sobreposição simples e dupla por modelos de dano coesivo com obtenção das leis coesivas pelo método direto*. 2016, Tese de Mestrado de Engenharia Mecânica - Ramo Contruções Mecânicas. Instituto Superior de Engenharia do Porto: Porto.
8. da Silva, L.F.M., A.G. de Magalhães, and M.F.S.F. de Moura, *Juntas Adesivas Estruturais*. 2007, Porto: Publindústria.
9. Campilho, R.D.S.G., et al., *Modelling of Single-Lap Joints Using Cohesive Zone Models: Effect of the Cohesive Parameters on the Output of the Simulations.* The Journal of Adhesion, 2012. **88**(4-6): p. 513-533.
10. Ebnesajjad, S. and A.H. Landrock, *Adhesives Technology Handbook*. 3rd Edition ed. 2014, San Francisco: Elsevier.
11. Petrie, E.W., *Handbook of adhesives and sealants*. 2nd ed ed. 1999, New York: McGraw-Hill.
12. Cognard, P., *Handbook of Adhesives and Sealants*. 1st Edition ed. 2005: Elsevier Science.
13. Kinloch, A.J., *Adhesion and Adhesives: Science and Technology*. 1987, Heidelberg: Springer.
14. Adams, R.D., *Adhesive Bonding, Science, technology and applications*. 2005, Cambridge England: Woodhead Publishing.
15. Adams, R.D., J. Comyn, and W.C. Wake, *Structural adhesive joints in engineering*. 2nd edn ed. 1997, London: Chapman & Hall.
16. Dvorak, G.J., J. Zhang, and O. Canyurt, *Adhesive tongue-and-groove joints for thick composite laminates.* Composites Science and Technology, 2001. **61**(8): p. 1123-1142.

17. Ávila, A.F. and P.n.d.O. Bueno, *Stress analysis on a wavy-lap bonded joint for composites.* International Journal of Adhesion and Adhesives, 2004. **24**(5): p. 407-414.

18. Kim, K.S., et al., *Optimal tubular adhesive-bonded lap joint of the carbon fiber epoxy composite shaft.* Composite Structures, 1992. **21**(3): p. 163-176.

19. Chaudhury, M. and A.V. Pocius, *Adhesion Science and Engineering - 2*, ed. A.V. Pocius. 2002, Amsterdam: Elsevier Science.

20. Volkersen, O., *Die Niektraftverteilung in zugbeanspruchten mit konstanten laschenquerschritten.* Luftfahrtforschung, 1938. **15**: p. 41-47.

21. da Silva, L.F.M., et al., *Analytical models of adhesively bonded joints—Part I: Literature survey.* International Journal of Adhesion and Adhesives, 2009. **29**(3): p. 319-330.

22. Goland, M. and E. Reissner, *The stresses in cemented joints.* Journal of Applied Mechanics, 1944(66): p. A17-A27.

23. Hart-Smith, L.J., *Adhesive-Bonded Single-Lap Joints*. 1973, NASA CR-112236.

24. Renton, W.J. and J.R. Vinson, *Analysis of Adhesively Bonded Joints Between Panels of Composite Materials.* Journal of Applied Mechanics, 1977. **44**(1): p. 101-106.

25. Ojalvo, I.U. and H.L. Eidinoff, *Bond Thickness Effects upon Stresses in Single-Lap Adhesive Joints.* AIAA Journal, 1978. **16**(3): p. 204-211.

26. ALLMAN, D.J., *A THEORY FOR ELASTIC STRESSES IN ADHESIVE BONDED LAP JOINTS.* The Quarterly Journal of Mechanics and Applied Mathematics, 1977. **30**(4): p. 415-436.

27. Chen, D. and S. Cheng, *An Analysis of Adhesive-Bonded Single-Lap Joints.* Journal of Applied Mechanics, 1983. **50**(1): p. 109-115.

28. Adams, R.D. and V. Mallick, *A Method for the Stress Analysis of Lap Joints.* The Journal of Adhesion, 1992. **38**(3-4): p. 199-217.

29. Zhao, B. and Z.-H. Lu, *A Two-Dimensional Approach of Single-Lap Adhesive Bonded Joints.* Mechanics of Advanced Materials and Structures, 2009. **16**(2): p. 130-159.

30. Yang, C. and S.S. Pang, *Stress-Strain Analysis of Single-Lap Composite Joints Under Tension.* Journal of Engineering Materials and Technology, 1996. **118**(2): p. 247-255.

31. Crocombe, A.D., *Stress analysis for adhesive structures*, in *2nd World Congress on Adhesion and Related Phenomena*. 2002, The Adhesion Society: Florida. p. 17 - 19.

32. Zhao, X., R.D. Adams, and L.F.M. da Silva, *Single Lap Joints with Rounded Adherend Corners: Stress and Strain Analysis.* Journal of Adhesion Science and Technology, 2011. **25**(8): p. 819-836.

33. Zhao, X., R.D. Adams, and L.F.M. da Silva, *Single Lap Joints with Rounded Adherend Corners: Experimental Results and Strength Prediction.* Journal of Adhesion Science and Technology, 2011. **25**(8): p. 837-856.

34. da Silva, L.F.M., et al., *Effect of material, geometry, surface treatment and environment on the shear strength of single lap joints.* International Journal of Adhesion and Adhesives, 2009. **29**(6): p. 621-632.

35. Williams, M.L., *The stresses around a fault or crack in dissimilar media.* Bulletin of the Seismological Society of America, 1959. **49**(2): p. 199-204.

36. Fernlund, G. and J.K. Spelt, *Failure load prediction of structural adhesive joints.* International Journal of Adhesion and Adhesives, 1991. **11**(4): p. 213-227.

37. Shahin, K. and F. Taheri, *The strain energy release rates in adhesively bonded balanced and unbalanced specimens and lap joints.* International Journal of Solids and Structures, 2008. **45**(25–26): p. 6284-6300.

38. Dillard, D.A., et al., *Observations of Decreased Fracture Toughness for Mixed Mode Fracture Testing of Adhesively Bonded Joints.* Journal of Adhesion Science and Technology, 2009. **23**(10-11): p. 1515-1530.

39. Rice, J.R. and G.F. Rosengren, *Plane strain deformation near a crack tip in a power-law hardening material.* Journal of the Mechanics and Physics of Solids, 1968. **16**(1): p. 1-12.

40. Barenblatt, G.I., *The formation of equilibrium cracks during brittle fracture. General ideas and hypotheses. Axially-symmetric cracks.* Journal of Applied Mathematics and Mechanics, 1959. **23**(3): p. 622-636.

41. Barenblatt, G.I., *The Mathematical Theory of Equilibrium Cracks in Brittle Fracture*, in *Advances in Applied Mechanics*, T.v.K.G.K.F.H.v.d.D. H.L. Dryden and L. Howarth, Editors. 1962, Elsevier. p. 55-129.

42. Dugdale, D.S., *Yielding of steel sheets containing slits.* Journal of the Mechanics and Physics of Solids, 1960. **8**(2): p. 100-104.

43. Xie, D. and A.M. Waas, *Discrete cohesive zone model for mixed-mode fracture using finite element analysis.* Engineering Fracture Mechanics, 2006. **73**(13): p. 1783-1796.

44. Cui, W. and M.R. Wisnom, *A combined stress-based and fracture-mechanics-based model for predicting delamination in composites.* Composites, 1993. **24**(6): p. 467-474.

45. Feraren, P. and H.M. Jensen, *Cohesive zone modelling of interface fracture near flaws in adhesive joints.* Engineering Fracture Mechanics, 2004. **71**(15): p. 2125-2142.

46. Yang, Q.D., M.D. Thouless, and S.M. Ward, *Elastic–plastic mode-II fracture of adhesive joints.* International Journal of Solids and Structures, 2001. **38**(18): p. 3251-3262.

47. ABAQUS® Documentation. 2009, Dassault Systèmes: Vélizy-Villacoublay.

48. Zhu, Y., K.M. Liechti, and K. Ravi-Chandar, *Direct extraction of rate-dependent traction–separation laws for polyurea/steel interfaces.* International Journal of Solids and Structures, 2009. **46**(1): p. 31-51.

49. Campilho, R.D.S.G., M.F.S.F. de Moura, and J.J.M.S. Domingues, *Using a cohesive damage model to predict the tensile behaviour of CFRP single-strap repairs.* International Journal of Solids and Structures, 2008. **45**(5): p. 1497-1512.

50. Alfano, G. and M.A. Crisfield, *Finite element interface models for the delamination analysis of laminated composites: mechanical and computational issues.* International Journal for Numerical Methods in Engineering, 2001. **50**(7): p. 1701-1736.

51. Allix, O. and A. Corigliano, *Modeling and simulation of crack propagation in mixed-modes interlaminar fracture specimens.* International Journal of Fracture. **77**(2): p. 111-140.

52. Chen, J., *Predicting Progressive Delamination of Stiffened Fibre-Composite Panel and Repaired Sandwich Panel by Decohesion Models.* Journal of Thermoplastic Composite Materials, 2002. **15**(5): p. 429-442.

53. Chandra, N., et al., *Some issues in the application of cohesive zone models for metal–ceramic interfaces.* International Journal of Solids and Structures, 2002. **39**(10): p. 2827-2855.

54. Kafkalidis, M.S. and M.D. Thouless, *The effects of geometry and material properties on the fracture of single lap-shear joints.* International Journal of Solids and Structures, 2002. **39**(17): p. 4367-4383.

55. Campilho, R.D.S.G., M.F.S.F. de Moura, and J.J.M.S. Domingues, *Numerical prediction on the tensile residual strength of repaired CFRP under different geometric changes.* International Journal of Adhesion and Adhesives, 2009. **29**(2): p. 195-205.

56. Pinto, A.M.G., et al., *Single-Lap Joints of Similar and Dissimilar Adherends Bonded with an Acrylic Adhesive.* The Journal of Adhesion, 2009. **85**(6): p. 351-376.

57. Campilho, R.D.S.G., et al., *Adhesively Bonded Repair Proposal for Wood Members Damaged by Horizontal Shear Using Carbon-Epoxy Patches.* The Journal of Adhesion, 2010. **86**(5-6): p. 649-670.

58. Campilho, R.D.S.G., et al., *Strength prediction of single- and double-lap joints by standard and extended finite element modelling.* International Journal of Adhesion and Adhesives, 2011. **31**(5): p. 363-372.

59. Jing, J., et al., *Simulation of dynamic fracture along solder–pad interfaces using a cohesive zone model.* Engineering Failure Analysis, 2009. **16**(5): p. 1579-1586.

60. Benzeggagh, M.L. and M. Kenane, *Measurement of mixed-mode delamination fracture toughness of unidirectional glass/epoxy composites with mixed-mode bending apparatus.* Composites Science and Technology, 1996. **56**(4): p. 439-449.

61. Campilho, R.D.S.G., et al., *Modelling adhesive joints with cohesive zone models: effect of the cohesive law shape of the adhesive layer.* International Journal of Adhesion and Adhesives, 2013. **44**: p. 48-56.

62. Ridha, M., V.B.C. Tan, and T.E. Tay, *Traction–separation laws for progressive failure of bonded scarf repair of composite panel.* Composite Structures, 2011. **93**(4): p. 1239-1245.

63. Campilho, R.D.S.G., et al., *Strength Improvement of Adhesively-Bonded Joints Using a Reverse-Bent Geometry.* Journal of Adhesion Science and Technology, 2011. **25**(18): p. 2351-2368.

64. Campilho, R.D.S.G., et al., *Modelling the tensile fracture behaviour of CFRP scarf repairs.* Composites Part B: Engineering, 2009. **40**(2): p. 149-157.

65. Campilho, R.D.S.G., et al., *Computational Modelling of the Residual Strength of Repaired Composite Laminates Using a Cohesive Damage Model.* Journal of Adhesion Science and Technology, 2008. **22**(13): p. 1565-1591.

66. Jain, L.K. and Y.-W. Mai, *Analysis of resin-transfer-moulded single-lap joints.* Composites Science and Technology, 1999. **59**(10): p. 1513-1518.

67. Reis, P.N.B., F.J.V. Antunes, and J.A.M. Ferreira, *Influence of superposition length on mechanical resistance of single-lap adhesive joints.* Composite Structures, 2005. **67**(1): p. 125-133.

68. John, S.J., A.J. Kinloch, and F.L. Matthews, *Measuring and predicting the durability of bonded carbon fibre/epoxy composite joints.* Composites, 1991. **22**(2): p. 121-127.

69. Hu, F.Z. and C. Soutis, *Strength prediction of patch-repaired CFRP laminates loaded in compression.* Composites Science and Technology, 2000. **60**(7): p. 1103-1114.

70. McGeorge, D., *Inelastic fracture of adhesively bonded overlap joints.* Engineering Fracture Mechanics, 2010. **77**(1): p. 1-21.

71. Davis, M. and D. Bond, *Principles and practices of adhesive bonded structural joints and repairs.* International Journal of Adhesion and Adhesives, 1999. **19**(2–3): p. 91-105.

72. Shin, K.C. and J.J. Lee, *Bond Parameters to Improve Tensile Load Bearing Capacities of Co-Cured Single and Double Lap Joints with Steel and Carbon Fiber-epoxy Composite Adherends.* Journal of Composite Materials, 2003. **37**(5): p. 401-420.

73. Andersson, T. and U. Stigh, *The stress–elongation relation for an adhesive layer loaded in peel using equilibrium of energetic forces.* International Journal of Solids and Structures, 2004. **41**(2): p. 413-434.

74. Yang, Q.D., M.D. Thouless, and S.M. Ward, *Numerical simulations of adhesively-bonded beams failing with extensive plastic deformation.* Journal of the Mechanics and Physics of Solids, 1999. **47**(6): p. 1337-1353.

75. Pandya, K.C. and J.G. Williams, *Measurement of cohesive zone parameters in tough polyethylene.* Polymer Engineering & Science, 2000. **40**(8): p. 1765-1776.

76. Sørensen, B.F., *Cohesive law and notch sensitivity of adhesive joints.* Acta Materialia, 2002. **50**(5): p. 1053-1061.

77. Campilho, R.D.S.G., et al., *Fracture toughness determination of adhesive and co-cured joints in natural fibre composites.* Composites Part B: Engineering, 2013. **50**: p. 120-126.

78. Carlberger, T. and U. Stigh, *Influence of Layer Thickness on Cohesive Properties of an Epoxy-Based Adhesive—An Experimental Study.* The Journal of Adhesion, 2010. **86**(8): p. 816-835.

79. Ji, G., et al., *Effects of adhesive thickness on global and local Mode-I interfacial fracture of bonded joints.* International Journal of Solids and Structures, 2010. **47**(18–19): p. 2445-2458.

80. Banea, M.D., L.F.M. da Silva, and R.D.S.G. Campilho, *Mode I fracture toughness of adhesively bonded joints as a function of temperature: Experimental and numerical study.* International Journal of Adhesion and Adhesives, 2011. **31**(5): p. 273-279.

81. Campilho, R.D.S.G., *Repair of composite and wood structures*. 2009, Engineering Faculty of Porto University: Porto.

82. Flinn, B.D., et al., *Fracture Resistance Characteristics of a Metal-Toughened Ceramic.* Journal of the American Ceramic Society, 1993. **76**(2): p. 369-375.

83. Mello, A.W. and K.M. Liechti, *The Effect of Self-Assembled Monolayers on Interfacial Fracture.* Journal of Applied Mechanics, 2004. **73**(5): p. 860-870.

84. Li, S., et al., *Use of a cohesive-zone model to analyze the fracture of a fiber-reinforced polymer–matrix composite.* Composites Science and Technology, 2005. **65**(3–4): p. 537-549.

85. Jung Lee, M., et al., *Determination of cohesive parameters for a mixed-mode cohesive zone model.* International Journal of Adhesion and Adhesives, 2010. **30**(5): p. 322-328.

86. Khoramishad, H., et al., *Predicting fatigue damage in adhesively bonded joints using a cohesive zone model.* International Journal of Fatigue, 2010. **32**(7): p. 1146-1158.

87. Daudeville, L. and P. Ladevèze, *A damage mechanics tool for laminate delamination.* Composite Structures, 1993. **25**(1): p. 547-555.

88. Voyiadjis, G.Z. and P.I. Kattan, *Damage mechanics*. 2005, New York: Marcell Dekker.

89. Raghavan, P. and S. Ghosh, *A continuum damage mechanics model for unidirectional composites undergoing interfacial debonding.* Mechanics of Materials, 2005. **37**(9): p. 955-979.

90. Wahab, M.M.A., et al., *Prediction of fatigue thresholds in adhesively bonded joints using damage mechanics and fracture mechanics.* Journal of Adhesion Science and Technology, 2001. **15**(7): p. 763-781.

91. Shenoy, V., et al., *Fracture mechanics and damage mechanics based fatigue lifetime prediction of adhesively bonded joints subjected to variable amplitude fatigue.* Engineering Fracture Mechanics, 2010. **77**(7): p. 1073-1090.

92. Lemaitre, J., *Local approach of fracture.* Engineering Fracture Mechanics, 1986. **25**(5): p. 523-537.

93. Lemaitre, J. and J.L. Chaboche, *Mechanics of Solid Materials*. 1990: Cambridge University Press.

94. Sampaio, E.M., F. Luiz Bastian, and H.S. Costa Mattos, *A simple continuum damage model for adhesively bonded butt joints.* Mechanics Research Communications, 2004. **31**(4): p. 443-449.

95. Hua, Y., et al., *Continuum damage modelling of environmental degradation in joints bonded with EA9321 epoxy adhesive.* International Journal of Adhesion and Adhesives, 2008. **28**(6): p. 302-313.

96. Belytschko, T. and T. Black, *Elastic crack growth in finite elements with minimal remeshing.* International Journal for Numerical Methods in Engineering, 1999. **45**: p. 601-620.

97. Mohammadi, S., *Extended Finite Element Method for Fracture Analysis of Structures*. 2008, New Jersey: Blackwell Publishing.

98. Moës, N., J. Dolbow, and T. Belytschko, *A finite element method for crack growth without remeshing.* International Journal for Numerical Methods in Engineering, 1999. **46**: p. 131-150.

99. Campilho, R.D.S.G., et al., *eXtended Finite Element Method for fracture characterization of adhesive joints in pure mode I.* Computational Materials Science, 2011. **50**(4): p. 1543-1549.

100. Sukumar, N., et al., *Extended finite element method for three-dimensional crack modelling.* International Journal for Numerical Methods in Engineering, 2000. **48**: p. 1549-1570.

101. Daux, C., et al., *Arbitrary branched and intersecting cracks with the extended finite element method.* International Journal for Numerical Methods in Engineering, 2000. **48**: p. 1741-1760.

102. Moës, N. and T. Belytschko, *Extended finite element method for cohesive crack growth.* Engineering Fracture Mechanics, 2002. **69**(7): p. 813-833.

103. Elguedj, T., A. Gravouil, and A. Combescure, *Appropriate extended functions for X-FEM simulation of plastic fracture mechanics.* Computer Methods in Applied Mechanics and Engineering, 2006. **195**(7–8): p. 501-515.

104. Moreira, P.M.G.P., et al., *Fatigue crack growth in friction stir welds of 6082-T6 and 6061-T6 aluminium alloys: A comparison.* Theoretical and Applied Fracture Mechanics, 2008. **50**(2): p. 81-91.

105. Faneco, T.M.S., *Caraterização das propriedades mecânicas de um adesivo estrutural de alta ductilidade*. 2014, Tese de Mestrado em Engenharia Mecânica - Ramo Materias e Tecnologias de Fabrico. Instituto Superior de Engenharia do Porto: Porto.

106. Alfano, G., *On the influence of the shape of the interface law on the application of cohesive-zone models.* Composites Science and Technology, 2006. **66**(6): p. 723-730.

107. Li, S., et al., *Mixed-mode cohesive-zone models for fracture of an adhesively bonded polymer–matrix composite.* Engineering Fracture Mechanics, 2006. **73**(1): p. 64-78.

108. Carlberger, T. and U. Stigh, *An explicit FE-model of impact fracture in an adhesive joint.* Engineering Fracture Mechanics, 2007. **74**(14): p. 2247-2262.

109. Pocius, A.V., *Adhesion and Adhesives Technology, An Introduction*. 2nd Edition ed. 2002: Hanser.

110. Campilho, R.D.S.G., M.F.S.F. de Moura, and J.J.M.S. Domingues, *Modelling single and double-lap repairs on composite materials.* Composites Sci. Technol., 2005. **65**(null): p. 1948.

111. Leffler, K., K.S. Alfredsson, and U. Stigh, *Shear behaviour of adhesive layers.* International Journal of Solids and Structures, 2007. **44**(2): p. 530-545.

112. Högberg, J.L. and U. Stigh, *Specimen proposals for mixed mode testing of adhesive layer.* Engineering Fracture Mechanics, 2006. **73**(16): p. 2541-2556.

113. de Moura, M.F.S.F., R.D.S.G. Campilho, and J.P.M. Gonçalves, *Pure mode II fracture characterization of composite bonded joints.* International Journal of Solids and Structures, 2009. **46**(6): p. 1589-1595.

114. de Moura, M.F.S.F., R.D.S.G. Campilho, and J.P.M. Gonçalves, *Crack equivalent concept applied to the fracture characterization of bonded joints under pure mode I loading.* Composites Science and Technology, 2008. **68**(10–11): p. 2224-2230.

115. Azevedo, J.C.S., *Determinação da tenacidade à fratura em tração (GIIC) de adesivos estruturais pelo ensaio End-Notched Flexure (ENF)*, in *Engenharia Mecânica*. 2014, Instituto Superior de Engenharia do Porto.

116. Faneco, T.M.S., *Caracterização das propriedades mecânicas de um adesivo estrutural de alta ductilidade*, in *Engenharia Mecânica*. 2014, Instituto Superior de Engenharia do Porto.

117. Campilho, R.D.S.G., M.F.S.F. de Moura, and J.J.M.S. Domingues, *Modelling single and double-lap repairs on composite materials.* Composites Science and Technology, 2005. **65**(13): p. 1948-1958.

118. Campilho, R.D.S.G., et al., *Experimental and numerical evaluation of composite repairs on wood beams damaged by cross-graining.* Construction and Building Materials, 2010. **24**(4): p. 531-537.

119. Kilic, B., E. Madenci, and D.R. Ambur, *Influence of adhesive spew in bonded single-lap joints.* Engineering Fracture Mechanics, 2006. **73**(11): p. 1472-1490.

120. Radice, J. and J. Vinson, *On the use of quasi-dynamic modeling for composite material structures: Analysis of adhesively bonded joints with midplane asymmetry and transverse shear deformation.* Composites Science and Technology, 2006. **66**(14): p. 2528-2547.

121. Pires, I., et al., *Performance of bi-adhesive bonded aluminium lap joints.* International Journal of Adhesion and Adhesives, 2003. **23**(3): p. 215-223.

122. Campilho, R.D.S.G., M.F.S.F. de Moura, and J.J.M.S. Domingues, *Stress and failure analyses of scarf repaired CFRP laminates using a cohesive damage model.* Journal of Adhesion Science and Technology, 2007. **21**(9): p. 855-870.

123. Vable, M. and J. Reddy Maddi, *Boundary element analysis of adhesively bonded joints.* International Journal of Adhesion and Adhesives, 2006. **26**(3): p. 133-144.

124. Luo, Q. and L. Tong, *Fully-coupled nonlinear analysis of single lap adhesive joints.* International Journal of Solids and Structures, 2007. **44**(7–8): p. 2349-2370.

125. da Silva, L.F.M. and M.J.C.Q. Lopes, *Joint strength optimization by the mixed-adhesive technique.* International Journal of Adhesion and Adhesives, 2009. **29**(5): p. 509-514.

126. Adams, R.D. and N.A. Peppiatt, *Stress analysis of adhesive-bonded lap joints.* Journal of Strain Analysis, 1974. **9**(3): p. 185-196.